R-10-74

On the role of model depth and hydraulic properties for groundwater flow modelling during glacial climate conditions

Patrik Vidstrand, TerraSolve AB

Ingvar Rhén, SWECO Environment AB

March 2011

Svensk Kärnbränslehantering AB
Swedish Nuclear Fuel
and Waste Management Co

Box 250, SE-101 24 Stockholm
Phone +46 8 459 84 00

ISSN 1402-3091
SKB R-10-74

On the role of model depth and hydraulic properties for groundwater flow modelling during glacial climate conditions

Patrik Vidstrand, TerraSolve AB

Ingvar Rhén, SWECO Environment AB

March 2011

Keywords: Hydrogeology, Groundwater, Modelling, Glacial.

Abstract

A common assumption in regional groundwater flow simulations of periods with glacial climate conditions is that the salinity at the bottom boundary of the model domain is stable (constant over time). This assumption is partly based on the general fact that water density increases with increasing salinity, but also supported by measurements, e.g. the mobile (fracture water) and immobile (pore-water) salinity typically increase with depth, whereas the conductive fracture frequency and fracture transmissivity often decrease with depth.

Plausibly, the depth to stable hydrogeological conditions varies between sites, and the question studied here is whether hydrogeological disturbances could occur at 2–4 km depth during glacial climate conditions. With regard to the results of SDM-Site and SR-Site, the hydrogeological conditions at repository depth indicate less groundwater flow during glacial climate conditions at Forsmark than at Laxemar. For this reason, this study uses the Laxemar site as a hypothetical site of potentially more permeable conditions, hence more readily affected during glacial climate conditions.

A series of flow simulations conducted with DarcyTools in an approximately 5 km deep, super-regional model domain centred on the Laxemar site are reported. The studied cases (model variants) represent a variety of different property specifications along with variations in initial conditions concerning salinity. The model domain is subjected to a transient top boundary representing an advancing ice sheet margin. The behaviour of the grid cell pressure, Darcy flux and mobile salinity is monitored at four different elevations along a vertical scan line through the centre of the suggested location for a KBS-3 repository at Laxemar. The studied monitoring points are located at –0.5 km, –2.5 km, –3.0 km, and –3.5 km. These elevations are chosen with the objective to study the range of hydrogeological disturbance that could occur at 2–4 km depth.

The flow model is run twice; first with hydraulic conditions that mimic temperate climate conditions, and second with hydraulic conditions that maximises the potential impact at depth during glacial climate conditions. The key assumptions made regarding the hydraulic conditions during the glacial phase are: 1) a thick ice sheet with a steep profile at the front, 2) a hydraulic pressure beneath the ice sheet that equals 92% of the ice thickness, 3) a low advance rate of the ice sheet margin, and 4) no permafrost beneath the ice sheet or in front of the ice sheet margin.

The results vary between the studied cases (model variants). For a model set-up that mimics the current hydrogeological conditions at the Laxemar site, the results are as follows:

- The grid cell Darcy flux magnitudes during temperate climate conditions are 10^{-11} m/s at –0.5 km and 10^{-13} m/s at –3.0 km. During the ice front passage, the relative increase in Darcy flux is approximately two orders of magnitude at all four monitoring points. The duration of this increase in Darcy flux is approximately 100 years.
- The grid cell salinities during temperate climate conditions are approximately 0% by weight at –0.5 km and approximately 7% by weight at –2.5 km. During the ice front passage, the grid cell salinity at –0.5 km first increases to approximately 2% by weight before it returns back to approximately 0% by weight. The duration of this pulse change in salinity is approximately 100 years. At –2.5 km elevation, the grid cell salinity decreases approximately to 6% by weight during the ice front passage. During the long period of complete ice coverage that follows the passage of ice front, the hydraulic gradients at depth are very small; hence it takes several thousand of years before the grid cell salinity at –2.5 km elevation is fully recovered.

Sammanfattning

I flertalet grundvattenstudier som simulerar perioder med glaciala klimatförhållanden är det vanligt att anta att den mobila saliniteten vid modelldomänens bottenrand är stabil (konstant över tiden). Detta antagande baseras delvis på att vattendensiteten ökar med ökad salinitet men är även givet av fältobservationer såsom att salthalten i så väl sprickvatten som matrisporvatten ökar med ökat djup samtidigt som konduktiv sprickfrekvens och spricktransmissivitet ofta minskar mot djupet.

Det är troligt att djupet till stabila hydrogeologiska förhållanden varierar från plats till plats och frågan som studeras i detta arbete är huruvida en hydrogeologisk störning kan uppträda på 2–4 kilometers djup under glaciala förhållanden. Resultat från SDM-Site och SR-Site indikerar att de hydrogeologiska förhållandena för ett KBS-3 förvarsdjup påverkas mindre i Forsmark än i Laxemar under glaciala förhållanden. Därför används i denna studie Laxemar som en hypotetisk mer genomsläpplig plats som därmed har större förutsättningar att påverkas under glaciala förhållanden.

I föreliggande studie redovisas en serie flödessimuleringar utförda med DarcyTools. Den superregionala modelldomänen är ca 5 km djup och simuleringarna studerar skillnader i grundvattenflöde mellan olika egenskapssättningar och initialvillkor avseende salt för ett KBS-3 förvar beläget i Laxemar. Randvillkoret på modelldomänens topprand representerar passagen av fronten hos en kontinentalis och studien fokuserar på förändringarna i tryck, Darcy flux och salinitet i fyra punkter, som ligger längs med en centralt belägen lodlinje genom KBS-3 förvaret. Djuppositionerna, som är valda i syfte att illustrera variationen i den hydrogeologiska störningen i djupintervallet 2–4 km, är –0,5 km, –2,5 km, –3,0 km och –3,5 km.

Modelleringen utförs två gånger för varje variant. Först med hydrauliska förhållanden som representerar tempererade förhållanden och sedan med hydrauliska förhållanden som maximerats med avseende på den glaciala störningen. Följande antaganden har därvidlag kombinerats: 1) isen är tjock och lutar brant vid fronten, 2) vattentrycket under isen motsvarar 92 % av istjockleken, 3) en långsam framåthastighet hos isfronten och 4) i området framför isen saknas permafrost.

Resultaten varierar mellan de olika studerade varianterna. För den variant som bäst efterliknar de rådande förhållandena i Laxemar är resultaten följande:

- De beräknade storleksordningarna på Darcy fluxer, under tempererade klimatförhållanden, är ungefär10^{-11} m/s på –0,5 km och 10^{-13} m/s på –3,0 km. Den relativa förändringen under isfrontpassagen är en ökning med ungefär två tiopotenser på alla undersökta nivåer. Denna ökning är representativ under ungefär 100 år.
- De beräknade salthalterna under tempererade förhållanden är ungefär 0 % (viktprocent) på –0,5 km och ungefär 7 % på –2,5 km. Under isfrontpassagen ökar salthalten på –0,5 km temporärt till ungefär 2 % innan den återgår till ungefär 0 % efter isfrontspassagen. Denna ökning och efterföljande minskning varar ungefär 100 år. På –2,5 km minskar salthalten successivt till ungefär 6 % under isfrontpassagen. Under den långa tidsperiod som platsen med förvaret är helt istäkt är de hydrauliska gradienterna låga och det tar flera tusen år innan salthalterna på –2,5 km återhämtas.

Contents

1 Introduction

1.1 Background

The Swedish Nuclear Fuel and Waste Management Company (SKB) has conducted site investigations at two different locations, the Forsmark and Laxemar-Simpevarp areas (Figure 1-1), with the objective of siting a final repository for spent nuclear fuel constructed on the basis of the KBS-3 concept.

In many groundwater flow simulations of periods with glacial climate conditions, e.g. /Vidstrand et al. 2010a, b, Walsh and Avis 2010, Lemieux et al. 2008a, b, c, Jaquet and Siegel 2006/, it is assumed that the chemical conditions at the bottom of the chosen model depth are relatively stable, and hence that all important groundwater responses are primarily found on top of the saline water; i.e. within the shallow, more fresh, water. As a consequence of the assumption, no-flow bottom boundary conditions are often advocated, typically between 2 and 4 km for the references mentioned above.

In the review of SKB FUD 2007 by /SSM 2009/, the opinion that SKB needs to illustrate this assumed chemical stability is expressed. As the glacial top boundary condition could create the most critical flow gradients during the full cycle assessed in SKB's climate reports /SKB 2006a, SKB 2010/, it is decided to assess the flow conditions at great depth within a deep model domain.

The flow modelling is based on a maximisation of the potential impact during glaciation; not only with regard to the adopted top boundary conditions but also with regard to the choice of bedrock properties. This maximisation was done in order to illustrate that during certain conditions an effect may be seen in the deep saline waters. Of the two sites, Forsmark and Laxemar, previously modelled during glacial climate condition by /Vidstrand et al. 2010a, b/, the Forsmark site has indicated relative stable conditions already at –0.5 km whereas the conditions at great depths at the Laxemar site appear to be more affected by the passage of the ice sheet margin.

The site chosen is hence the Laxemar site since this site is significantly more permeable as compared to the Forsmark site but also due to the somewhat deeper knowledge of bedrock conditions at depth at that site. It should however already here be stated that the detailed site specific knowledge is mainly down to c 1 km depth for both sites and deeper information at the Laxemar site comes from one borehole (KLX02) reaching about 1.6 km depth as illustrated in Figure 1-2. The assessed model depth of 5.2 km is almost 3 times deeper than the available source of site information and the modelling is hence based on a series of governing assumptions.

Figure 1-1. *Map of Sweden showing the location of the Forsmark and Laxemar-Simpevarp sites, located in the municipalities of Östhammar and Oskarshamn, respectively. (Figure 1-1 in /SKB 2008a/.)*

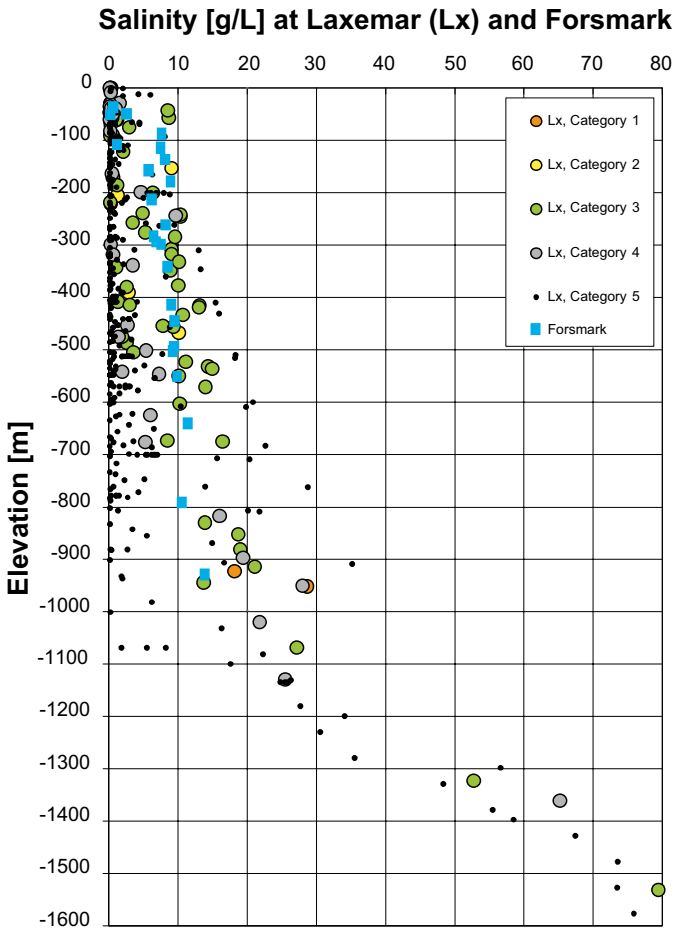

Figure 1-2. *Plot of all available salinity data from the core-drilled boreholes and percussion-drilled boreholes in Laxemar sorted according to quality category and in seven boreholes at Forsmark. The data in Laxemar are classified into five categories with regard to the quality of the sampling and/or analysis method, where category 1 represents the best quality and category 5 is the poorest. The Forsmark data are all of good quality in this regard (category 3 or better). (Modified after Figure 5-15 in /Follin et al. 2008/ and Figure 5-18 in /Rhén et al. 2009/.)*

1.2 Scope and objectives

The main objective of this study is to provide an indication of effects on the deep saline groundwater due to a passage of an ice front of a continental ice sheet. As such the results can be used to postulate on the stability of the hydrochemical environment at depth. The simulations are assumed to yield bounding, i.e. maximum, changes in salinity and flux since a bounding setting of the ice sheet is used (cf. Chapter 4). These bounding settings may not be the most likely, however, the situation considered cannot be totally ruled out.

The mathematical modelling used version 3.3[1] of the DarcyTools computational model /Svensson et al. 2010/.

The mathematical modelling considered two major climate periods; temperate and glacial, where the hydrogeological results of the temperate period are used as a reference for the hydrogeological results of the glacial period. The following physical and chemical performance measures are studied:

- Pressure (P).
- Darcy flux (q).
- Salinity (C).

The simulations of the glacial periods are carried out with a moving ice sheet margin. The average advance rate, 50 m/y, is coordinated with SKB's climate modelling /SKB 2010/. The simulations do not include effects caused by temperature gradients. Neither are disturbances caused by gas migration from the Earth's interior nor tidal forces included. All these processes are, however for the glacial case considered believed less important for the flow situation than the strong gradient during by the ice front passage.

The mathematical modelling applied top boundary conditions based on findings reported in previous studies on permafrost and ice sheet hydrology (see /Vidstrand et al. 2010a/ for a summary review). The boundary conditions were coupled to available hydrogeological and hydrochemical data for the site (see Chapter 2 and Chapter 3) and a flow model was created with large dimensions; 36 km by 21 km by 5.2 km (depth), see Figure 1-3. Hence, a super-regional hydrogeological modelling approach is used. In the previous modelling, as shown in Figure 1-3, the maximum depth of the models was chosen to be slightly deeper than 2 km. This truncation was considered sufficient for modelling of the flow conditions between the biosphere and the intended repository depth (approximately 500 m). In all these models, the super-regional model domains assessed yields conditions with large numerical cell sizes in many parts of the models even if DarcyTools unstructured grid allows for good resolution within volumes of particular interest.

The modelling is based on a maximisation of the potential impact during glaciation. The key assumptions made regarding the hydraulic conditions during the glacial phase are: 1) a thick ice sheet with a steep profile at the front, 2) a hydraulic pressure beneath the ice sheet that equals 92% of the ice thickness, 3) a low advance rate of the ice sheet margin, and 4) no permafrost beneath the ice sheet or in front of the ice sheet margin.

Also, an assumption of a low mechanical loading response is considered to be in line with the objective of the work as it enhances the hydraulic gradients imposed and thereby the Darcy fluxes and the chemical changes at depth. Therefore no mechanical coupling is included, meaning that the classic hydraulic mass balance equation for transient groundwater flow is applied.

[1] It is noted that the current documentation of DarcyTools relates to version 3.4 /Svensson et al. 2010/, but that the differences are insignificant for the applications reported here.

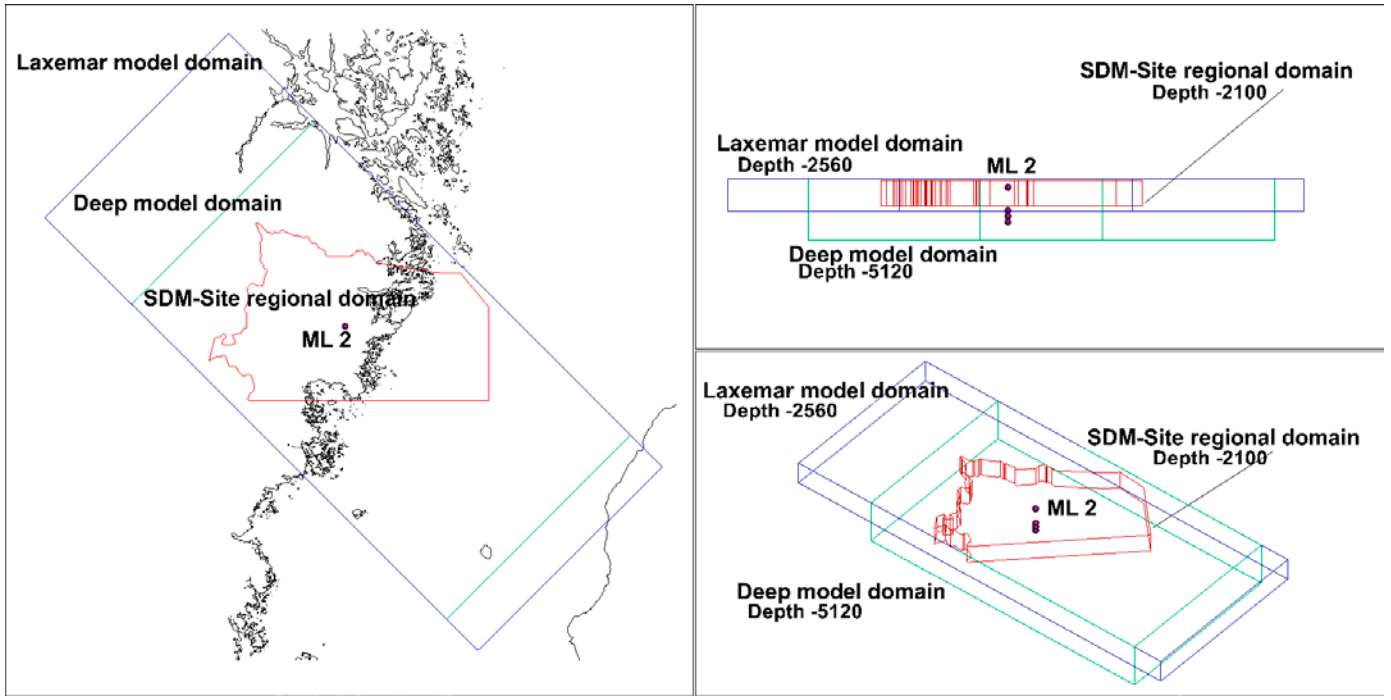

Figure 1-3. *Illustration of domains assessed in SDM (Site Descriptive Model) /SKB 2009/ (red), Laxemar groundwater flow simulation of periods with periglacial and glacial conditions (blue) /Vidstrand et al. 2010b/ and herein (Deep model domain) (green). The depth elevations of the three domains are –2,100 m (SDM site), –2,560 m (Laxemar model) and –5,120 m (this study).*

2 Settings of the Laxemar site

The Laxemar-Simpevarp area is located on the Swedish east coast near Oskarshamn and c 350 km south of Stockholm.

The investigated area is close to the coast, cf. Figure 2-1. The topography is fairly flat (regional topographic gradient in the order of 4%; the topography corresponds to the Sub-Cambrian Peneplain /Fredén 2002/) but with relatively distinct valleys, cf. Figure 2-2 and Figure 2-3. The investigation area is located within a crystalline basement, mostly covered by a rather thin till in the elevated areas and with glaciofluvial sediments in the larger valleys. The site-average annual precipitation and specific discharge are estimated to be on the order of 600 mm and 160–170 mm, respectively /Werner et al. 2008, Larsson-McCann et al. 2002/ and the area is covered with a fairly large number of small streams indicating small local drainage basins within the regional model area. The Äspö Hard Rock laboratory is an underground research facility that is located below the Äspö Island, cf. Figure 2-1, and the facility affects the groundwater flow locally in the area. The Simpevarp peninsula hosts the Clab interim facility and the nuclear power plants O1, O2 and O3. At Clab inflows are observed to the rock caverns near the surface and the shallow shafts surrounding the foundations of the power plants, but it has a very local effect on the groundwater flow. The hydrogeology of the area is described in more detail in /Rhén and Hartley 2009/.

2.1 Overview of the SKB´s system approach

In order to meet the objectives for model version SDM-Site Laxemar /Rhén and Hartley 2009/ (SDM: Site Descriptive Model), the groundwater system is divided into different hydraulic domains. Figure 2-4 illustrates schematically SKB's systems approach as employed in the hydrogeological SDM for Laxemar. The groundwater system consists of three basic hydraulic domain types, namely HSD, HCD and HRD, where:

- HSD (Hydraulic Soil Domain) represents the Quaternary deposits,
- HCD (Hydraulic Conductor Domain) represents deformation zones,
- HRD (Hydraulic Rock mass Domain) represents the fractured bedrock between the deformation zones.

The systems approach constitutes the basis for the conceptual modelling, the site investigations and the numerical simulations carried out in support of the hydrogeological SDM /Rhén et al. 2003/.

Besides the three hydraulic domains shown in Figure 2-4, the groundwater flow (saturated flow) and solute transport modelling consists of three additional elements:

- A solute (salt) transport model for the modelling of advective transport and matrix diffusion.
- Initial conditions for groundwater flow and hydrochemistry.
- Boundary conditions for groundwater flow and hydrochemistry.

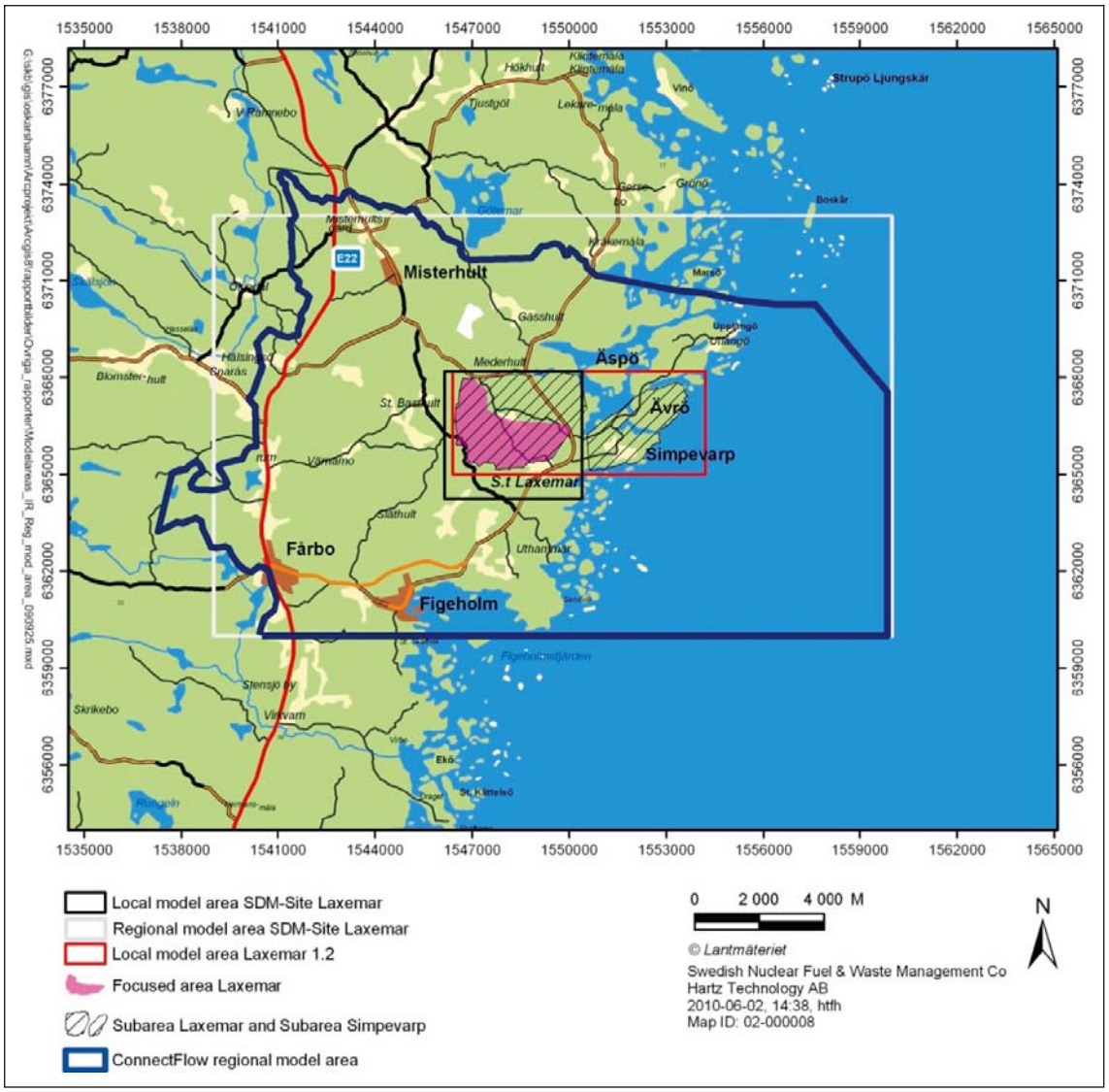

Figure 2-1. *Overview map of the Laxemar-Simpevarp regional model area. Regional and local model areas used for model version SDM-Site Laxemar are illustrated. The area coverage of the regional model is the same as that employed in previous model versions, whereas the local model area is significantly reduced compared to that employed in model version Laxemar 1.2. Laxemar subarea and Simpevarp subarea defined the investigation areas during the initial stage of the site investigations. The choice of boundaries used for the SDM-Site regional groundwater flow simulations (regional flow domain) based on surface water catchments is also shown (in this figure denoted ConnectFlow regional model area). /Rhén and Hartley 2009/.*

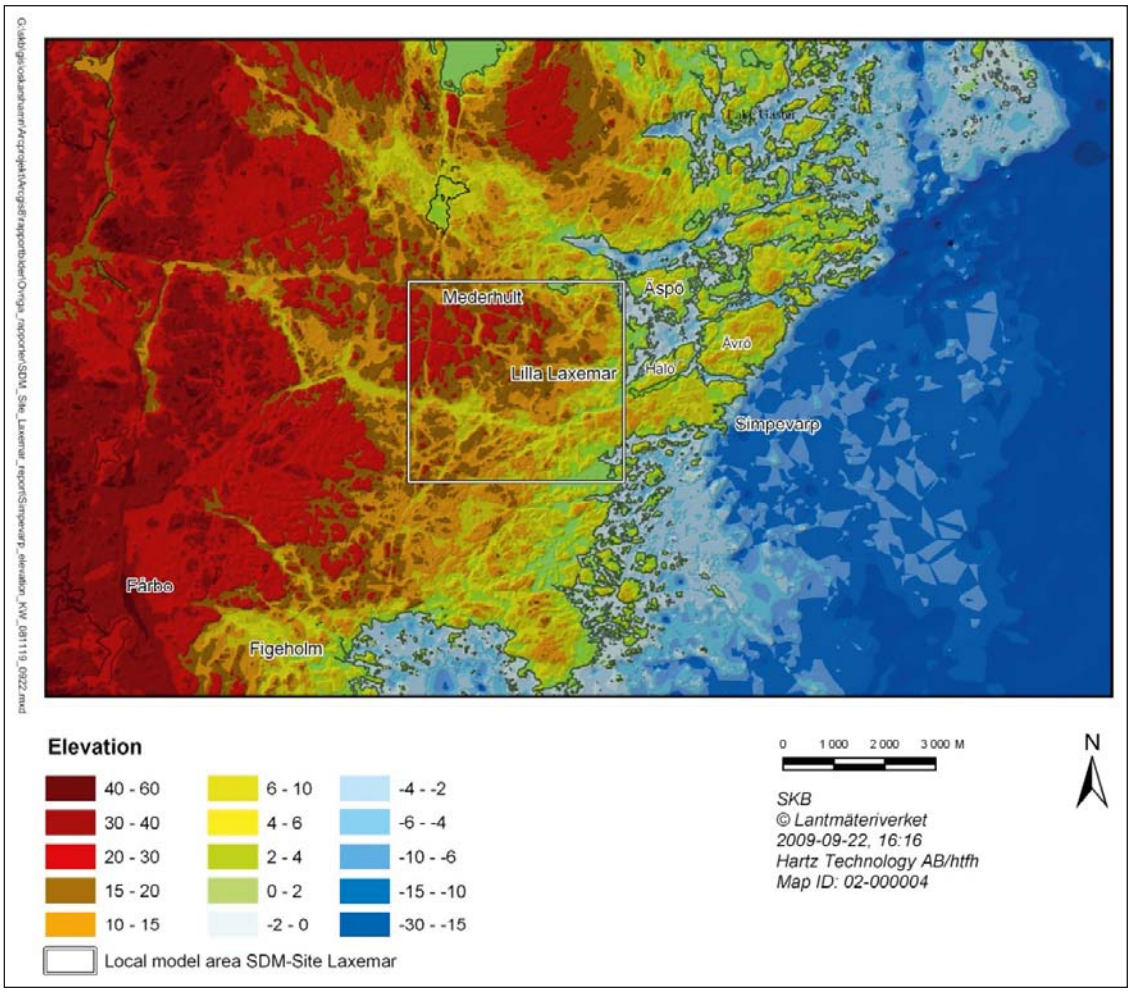

Figure 2-2. *Overview map illustrating the elevation of the ground-surface topography (m.a.s.l.) in an area corresponding to the Laxemar-Simpevarp regional model area, including the bathymetry of lakes and the sea. /Rhén and Hartley 2009/.*

Figure 2-3. *Air photographs showing the flat topography, low gradient near shore situation in the Laxemar-Simpevarp area with shallow bays, top) view from the southeast, Clab facility in the foreground, bottom) view from the west, drill site KLX05/KLX12A in the centre of the photograph. Both photographs show the outline of the focused area in Laxemar in red, cf. Figure 2-1 /Rhén and Hartley 2009/.*

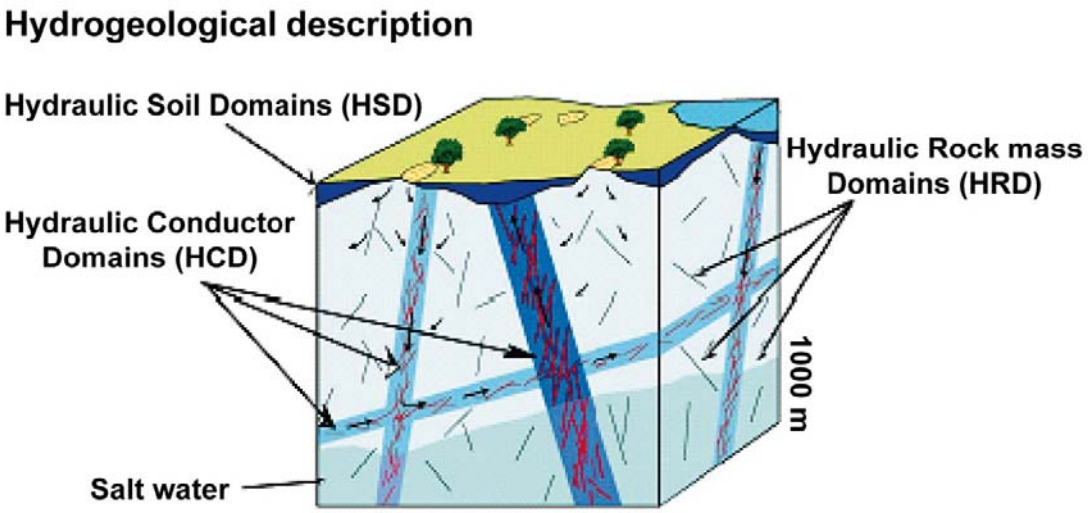

Figure 2-4. *Cartoon showing the division of the crystalline bedrock and the overburden (Quaternary deposits) into hydraulic domains. Within each domain, the hydraulic properties are represented by equivalent values, or by spatially distributed statistical distributions /Rhén et al. 2003/.*

2.2 Summary of the bedrock hydrogeological model

2.2.1 General

Single-hole hydraulic tests, interference tests, groundwater levels and hydrochemical data are the basis for the hydrogeological characterisation, together with the geological model. Investigations have essentially been made down to c 1,000 m depth but there is one borehole (KLX02) that provide data down to c 1,600 m depth. The PFL-f (f stands for fracture or feature, PFL is abbreviation for *Posiva Flow Log*) method is essential for the hydrogeological model. The PFL-f method constitutes a geophysical logging device developed to detect continuously flowing features in sparsely fractured crystalline bedrock by means of difference flow logging, using a 1 m test section that is moved step-wise 0.1 m. The PFL method essentially provides an estimate of the specific capacity (Q/s) [L^2T^{-1}], where s represents the drawdown and Q the flow rate. Transient injection tests with PSS (*Pipe String System*) have been performed using 3 different test scales: 5, 20 and 100 m with 5 m tests only being performed in the elevation interval –300 m to –700 m, covering the foreseen repository depth, cf. /Rhén and Hartley 2009/ for details.

The Laxemar-Simpevarp regional model area is in general characterised by an undulating bedrock surface with a thin cover of Quaternary deposits, mainly till on the top of the hills and thicker Quaternary deposits in the valleys made up of till overlain by postglacial deposits. The crystalline bedrock is intersected by a number of deformation zones, denoted Hydraulic Conductor Domains (HCD) in the hydrogeological model, which are mainly steeply dipping, with less fractured bedrock between these zones. The bedrock in between the HCDs is in the hydrogeological model called Hydraulic Rock mass Domains (HRD). Hydraulically, the deformation zones are generally more conductive than the bedrock in between. The general tendency within the Laxemar-Simpevarp regional model volume is that the hydraulic conductivity decreases with depth in both HCDs and HRDs. The Quaternary deposits, called Hydraulic Soil Domains (HSD) in the hydrogeological model are generally more conductive than the bedrock. Figure 2-5 shows a generalised vertical section illustrating the overall hydrological and hydrogeological conceptual model of the Laxemar-Simpevarp area. The hydrogeological characteristics of the HCDs, HRDs and HSDs are further described in Sections 2.2.2 through 2.2.4 and 2.3; details are found in /Rhén et al. 2008/.

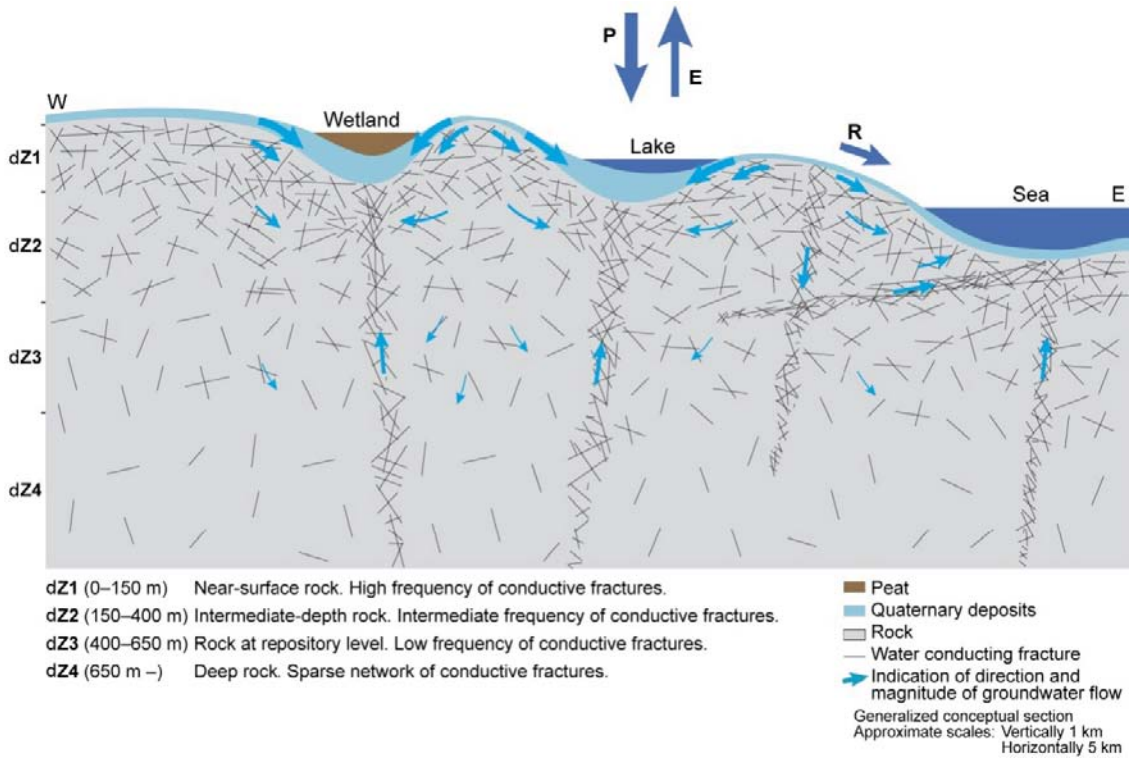

Figure 2-5. *Generalised section illustrating the conceptual model of hydrology and hydrogeology in Laxemar. Note the different horizontal (5 km) and vertical (1 km) scales. Furthermore, the thickness of the Quaternary deposits is exaggerated in the figure. /Rhén and Hartley 2009/.*

2.2.2 Hydraulic characteristics of hydraulic conductor domains (HCD)

The deformation zone model, as implemented in the SDM-Site regional flow domain, is shown in Figure 2-6.

The data and the general models suggested for the initial assignment of hydraulic properties to HCDs in the groundwater flow modelling are presented in Figure 2-7 cf. a detailed account in /Rhén et al. 2008/. The variability in transmissivity is large but considering mean values for depth zones employed in the HRD modelling, see Figure 2-7, the transmissivity decreases with depth, cf. /Rhén et al. 2008/. There is also a tendency that the transmissivity is positively correlated to the interpreted lineament length of the HCD and also that HCDs with E-W orientations are slightly more transmissive than HCDs of other orientations, cf. /Rhén et al. 2008/. However, some of the HCDs are intersected by several boreholes at a range of depths and it was judged that there was enough data for assessment of zone-specific trend functions for seven of the HCDs, cf. /Rhén et al. 2008/.

An exponential trend model is used for the depth trend of the transmissivity:

$$T(z)=10^{(a+B\cdot z)} \qquad (2\text{-}1)$$

z: Elevation in m (m.a.s.l.) (z defined positive up). The coefficients *a* and *B* in the exponential trend model are based on a linear regression of log10(T) data from surface down to lower most depth zone. See /Rhén et al. 2008/ for details.

Several interference tests have shown that dolerite dykes may act as hydraulic barriers, at least locally. The best example relates to the steep N-S oriented HCD ZSMNS001C just west of the focused area, associated with a core of dolerite, cf. /Rhén and Hartley 2009/. Both interference tests and monitoring data show fairly large differences in hydraulic head on either side of two other HCDs associated with dolerite dykes, ZSMNS059A and the KLX19_DZ5-8_dolerite, are also acting as hydraulic barriers, but probably to a lesser degree where the dykes become thinner. Mapping of the cored boreholes and outcropping deformation zones has shown that fault gouge is present in some deformation zones. This implies that these HCDs can exert some hydraulic barrier effect, most likely highly localised.

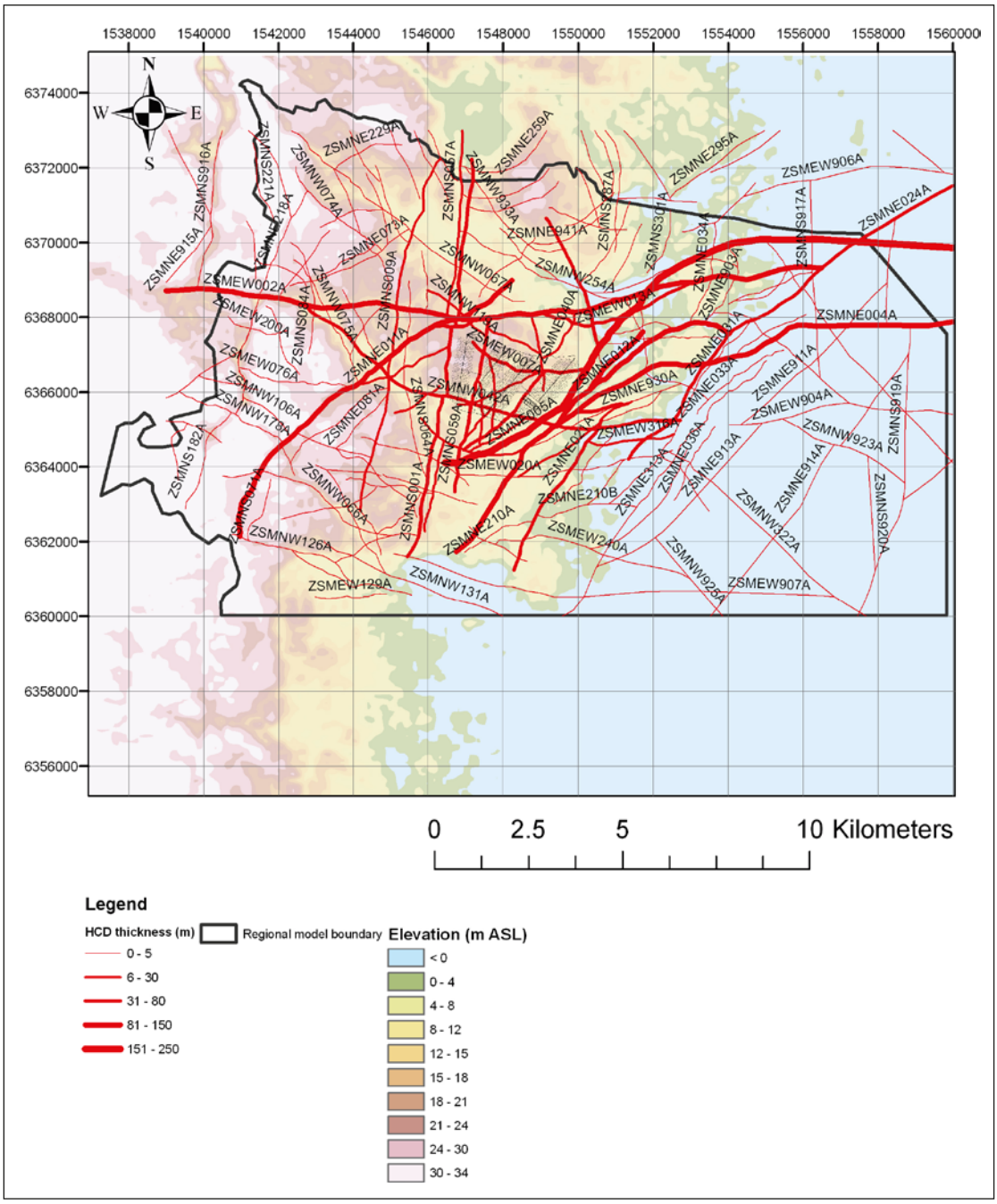

Figure 2-6. *Deformation zones included in the SDM-Laxemar deterministic deformation zone model. Colouring of zones is according to judged thickness.*

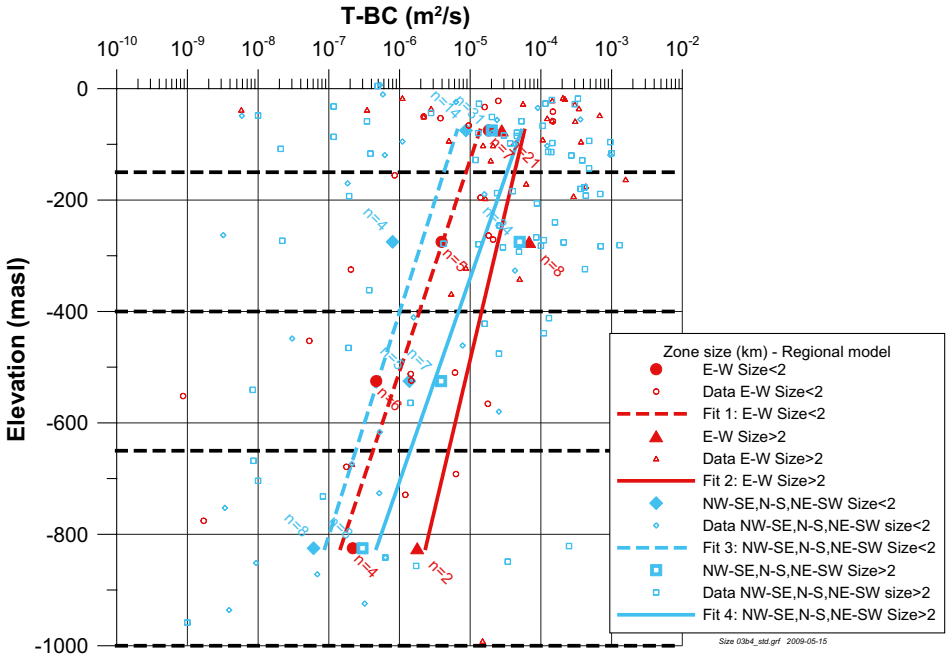

Figure 2-7. *Deformation zone transmissivity (T) related to deformation zone orientations in the horizontal plane and size, versus elevation for the regional model. Mean of $log_{10}(T)$, plotted as well as the number of observations (n). Regression line based on Mean of log10(T) /Rhén and Hartley 2009/.*

The distribution of the mean transmissivity in the HCD for the *base case*[2] is shown in Figure 2-8. For stochastic realisations with lateral heterogeneity within SDM-Site, these values are used as the mean sampled value for a log-normal distribution with specified standard deviation, but truncated at ± 2 standard deviations. Equivalent plots for one example realisation of the HCD with spatial variability, standard deviation in $\log_{10}(T)$=1.4, is shown in Figure 2-9. In both cases, the heterogeneous transmissivity field is conditioned to measured values at the intercept with borehole intervals where measurements are available. Thus, the local contact between the formation and the borehole will be as measured and not dependent on the realisation of the spatial distribution of the transmissivity values, which is important when measurements are compared to simulated entities.

2.2.3 Hydraulic characteristics of hydraulic rock mass domains (HRD)

The hydraulic rock mass domain model, as implemented in the SDM-Site regional flow domain, is shown in Figure 2-10 though Figure 2-13. According to /Rhén et al. 2008/, four separate hydraulic rock mass domains (HRD) should be modelled in the local model area; HRD_C, HRD_EW007, HRD_N and HRD_W, that are based on the fracture domains, cf. Figure 2-12, Figure 2-13 and /Wahlgren et al. 2008/.

The rock mass in the regional flow domain, outside the defined four HRDs mentioned above, is based on the material property assignments made in model version Laxemar 1.2 /SKB 2006b, Rhén et al. 2006/ (summarised in /Rhen et al. 2009/) and assessments of similarities between regional HRDs and the newly developed HRDs inside the Laxemar local model volume; HRD_C, HRD_EW007, HRD_N and HRD_W, cf. Table 2-1. The hydrogeological DFN for the HRDs is described in Appendix A.

[2] *"Base case"* in /Rhén and Hartley 2009/ accounting for the SDM-Site Laxemar modelling corresponds to "*Deterministic base model simulation"* in the SDM-Site Forsmark modelling /Follin 2008/.

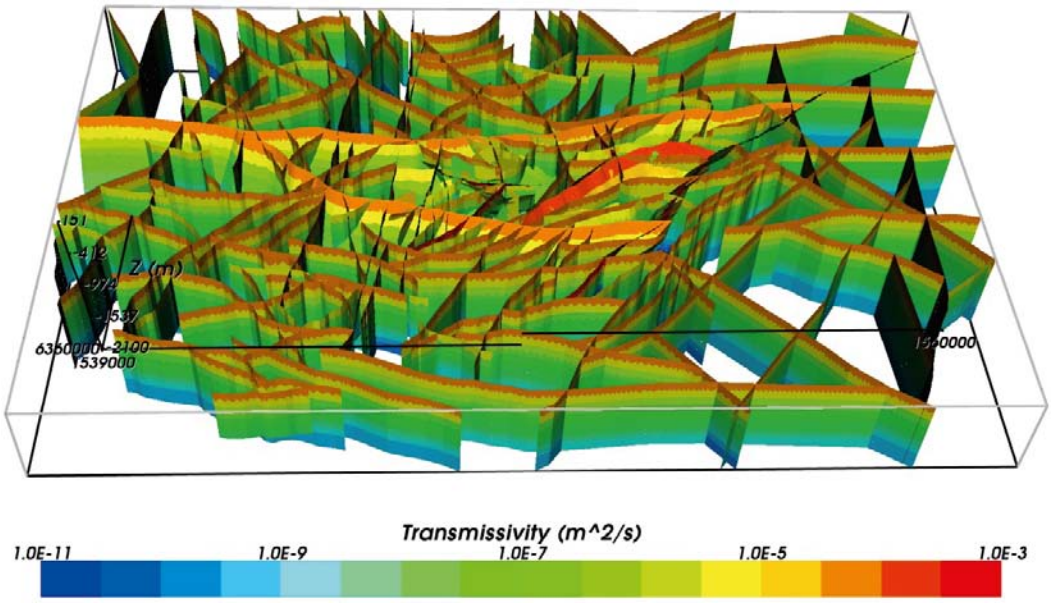

Figure 2-8. *All HCDs and their inferred depth dependent transmissivity for the deterministic base case model. Oblique view looking from the south. /Rhén and Hartley 2009/.*

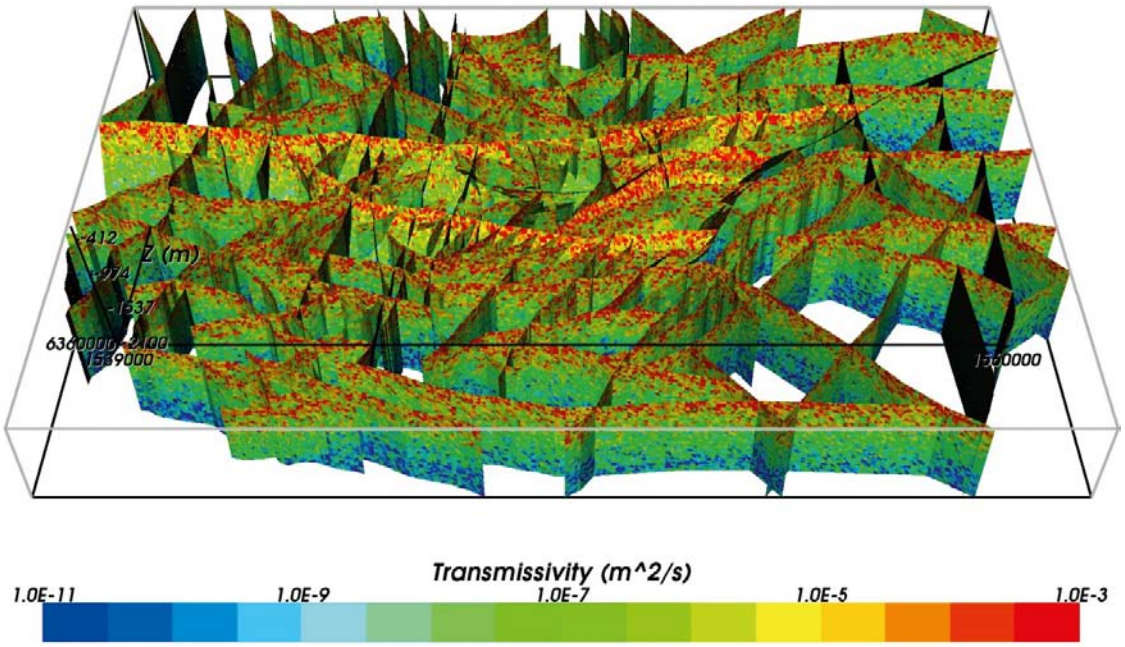

Figure 2-9. *All HCDs and their inferred depth dependent transmissivity for a case with spatial variability and a standard deviation in Log(T) of 1.4. Oblique view looking from the south. /Rhén and Hartley 2009/.*

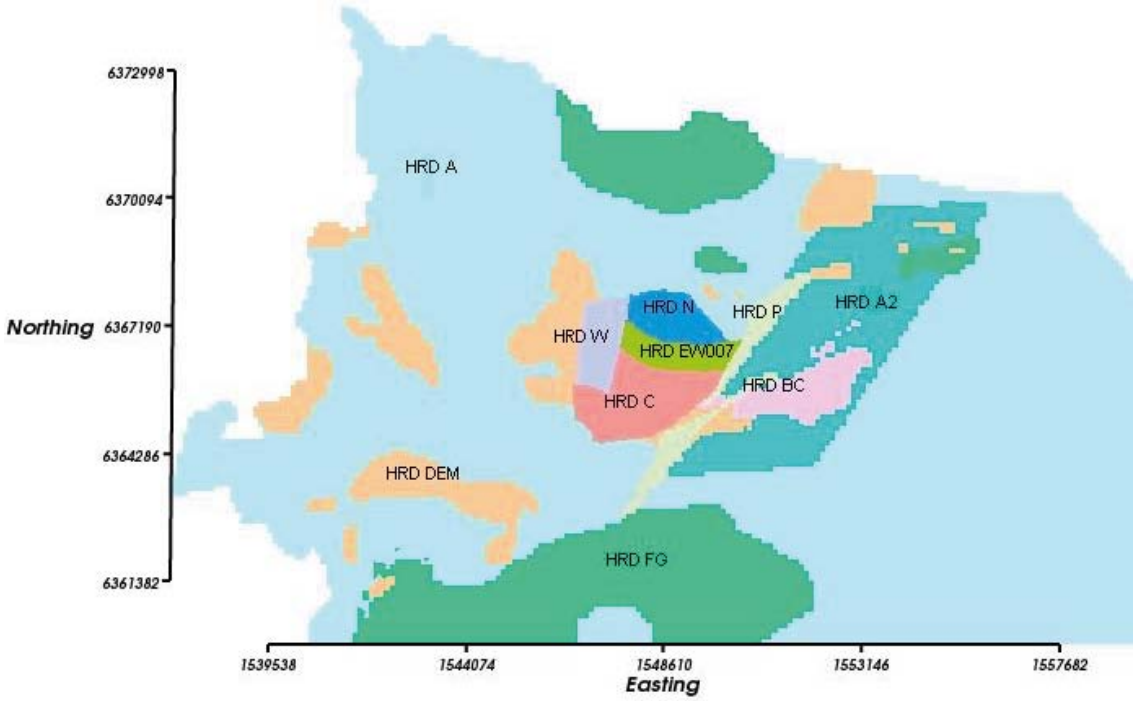

Figure 2-10. *Hydraulic rock mass domains on the top surface of the bedrock in the regional flow domain. /Rhén and Hartley 2009/.*

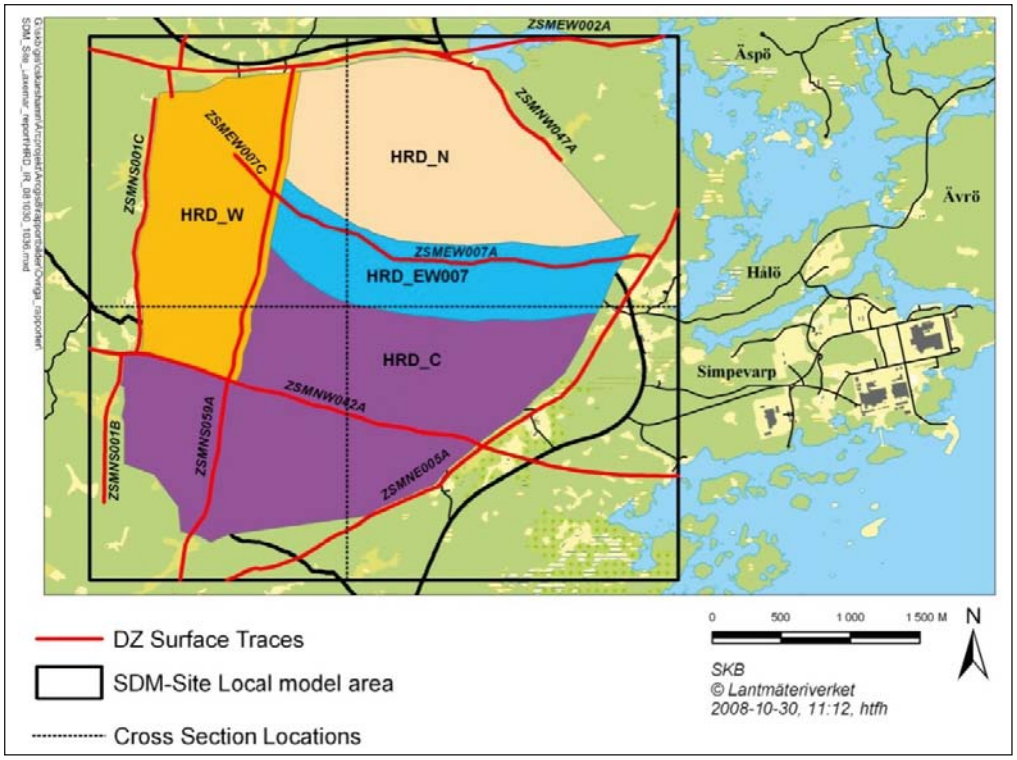

Figure 2-11. *Illustration of the SDM-Site Laxemar Hydraulic Rock Mass Domain Model. Horizontal view. DZ: Deformation zone. /Rhén and Hartley 2009/.*

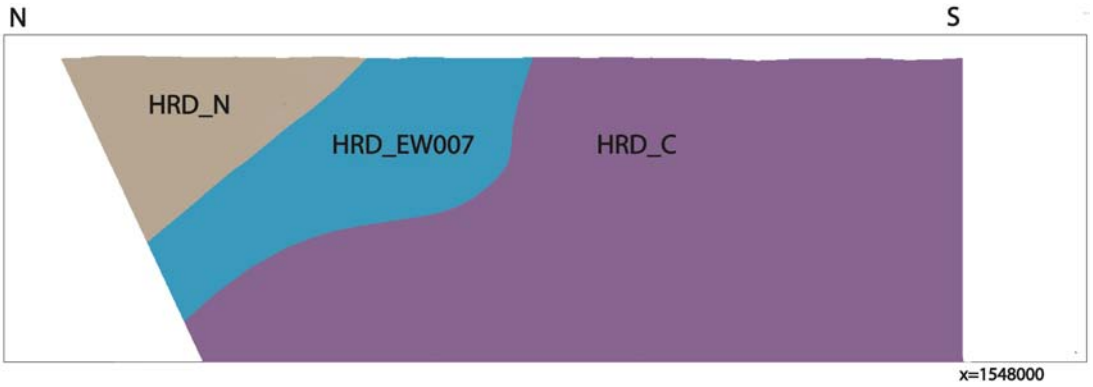

Figure 2-12. *Illustration of the SDM-Site Laxemar Hydraulic Rock Mass Domain Model. Vertical section from north (left) to south-at Easting's X=154,800 m, /Rhén and Hartley 2009/.*

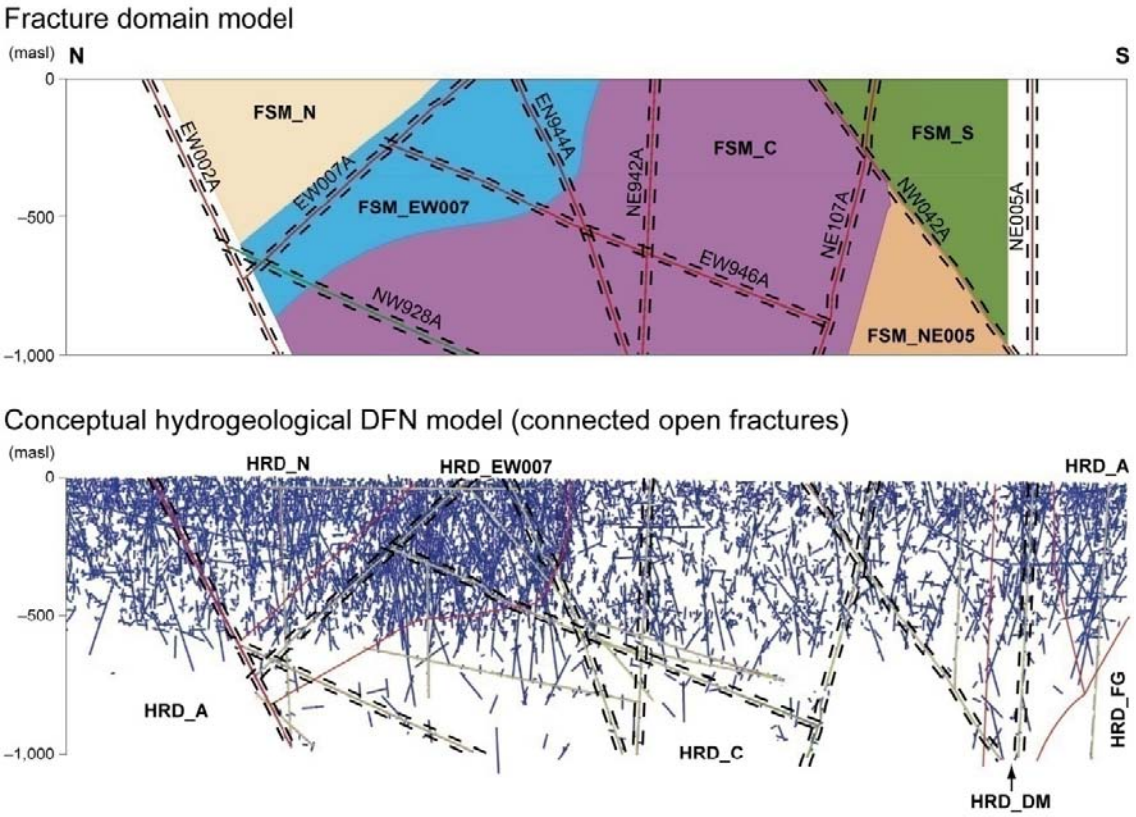

Figure 2-13. *Comparison of conceptual models for fracture domains, hydrogeological DFN and associated hydraulic rock mass domains along the N-S section cf. Figure 2-11. The length of the section is ~ 4,300 m. /SKB 2009/.*

Table 2-1. Proposed hydraulic property assignment of the regional-scale hydraulic rock mass domains to be used in SDM regional groundwater flow modelling /Rhén et al. 2008/.

Regional hydraulic rock mass domain	Suggested hydraulic properties based on hydrogeological DFN
HRD_A	HRD_N
HRD_A2	HRD_N, but rock below –650 masl is the same as –400 masl to –650 masl
HRD_D-E-M	HRD_C
HRD_B-C	HRD_C
HRD_F-G	HRD_N, but 10 times higher T
HRD_P	HRD_N

2.2.4 Hydraulic characteristics of the focused volume

The focused volume, cf. Figure 2-1, comprises HRD_C, HRD_W and the southern part of HRD_W, cf. Figure 2-11. HRD_EW007 is more conductive compared to HRD_C and HRD_W. An example of data used for the calibration of the hydrogeological DFN model is shown in Figure 2-14. The *base case* for SDM-Site Laxemar assumes a semi-correlated transmissivity model, cf. Table 2-3. The general characteristics of the HRDs are summarised in Table 2-5.

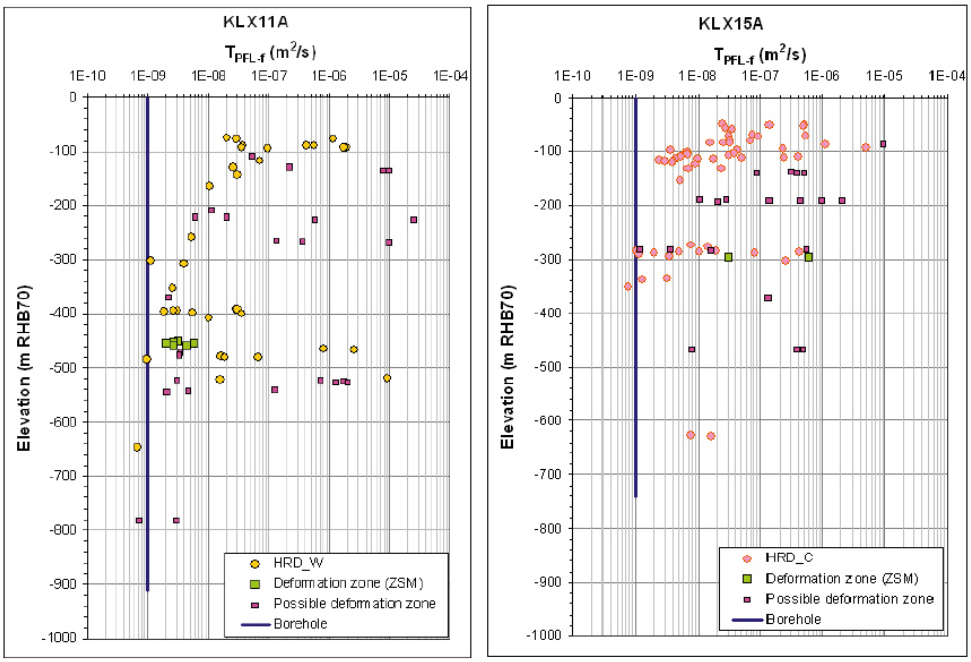

Figure 2-14. *Measured transmissivities (based on PFL-f) in fractures, located in deformation zones (squares) and in hydraulic rock mass domains (circles), in boreholes in the focused volume exemplified with two boreholes; KLX11A (HRD_W) and KLX15A (HRD_C) /SKB 2009/.*

Table 2-2 shows the laboratory measured permeability values of the rock matrix on core samples ranged from $7 \cdot 10^{-24}$ to $1 \cdot 10^{-19}$ m^2, corresponding to hydraulic conductivity values of $6 \cdot 10^{-17}$ to $1 \cdot 10^{-12}$ m/s, respectively. The presence of a fracture in one core sample (LAX-5) increased the permeability to c $1 \cdot 10^{-17}$ m^2.

The low hydraulic conductivity observed in the laboratory samples is supported by the field data shown in Figure 2-15. This figure shows a cumulative distribution plot of 631 $\log_{10}(K_{PSS})$ data measured with the Pipe String System (PSS) and a packer spacing[3] (test scale) of 5 m in the depth interval 0 to –1,000 m for rock between large deformation zones ("No-DZ"). Approximately 40% or more of the PSS data set below elevation –150 m have values below –9.9 (or $1.3 \cdot 10^{-10}$ m/s) which is the robust lower measurement limit of the PSS method /Rhèn et al. 2008/. These low conductive 5 m sections represents rock with low conductive fractures or borehole sections with no conductive fractures and a large part of these low conductive sections are considered to be measurement limit values; the hydraulic conductivity values are as low or lower than the value indicated in the plot.

Table 2-2. Sample positions along the borehole and average matrix permeability and corresponding hydraulic conductivity for confining pressures greater than 14 Mpa. Modified after /Vilks 2007/.

Sample	Core sample	Borehole length (m)	Permeability (m^2)	Conductivity (m/s)	Rock type
LAX -1*	KLX03–5	355.66	$(4\pm4)\cdot10^{-23}$	$(3\pm4)\cdot10^{-16}$	Ävrö granite
LAX-2	KLX03–8	524.63	$(8.6\pm0.9)\cdot10^{-22}$	$(7.5\pm0.8)\cdot10^{-15}$	Ävrö granite
LAX-3	KLX03–9	590.12	$(2.2\pm0.7)\cdot10^{-22}$	$(1.9\pm0.6)\cdot10^{-15}$	Ävrö granite
LAX-4	KLX03–9	590.12	$(4.1\pm1.1)\cdot10^{-21}$	$(3.6\pm0.9)\cdot10^{-14}$	Ävrö granite
LAX-5	KLX03–12	803.21	$1.45\cdot10^{-17}$	$1.27\cdot10^{-10}$	Quartz monzodiorite
LAX-6	KLX03–14	894.53	$(1.4\pm0.9)\cdot10^{-20}$	$(1.2\pm0.8)\cdot10^{-13}$	Quartz monzodiorite
LAX-7	KLX03–14	894.53	$(7.2\pm3.5)\cdot10^{-22}$	$(6.3\pm3.1)\cdot10^{-15}$	Quartz monzodiorite
LAX-8	KLX03–16	979.78	$(1.9\pm0.3)\cdot10^{-19}$	$(1.7\pm0.2)\cdot10^{-12}$	Quartz monzodiorite

* Average for confining pressures from 1.7 to 7.0 MPa.

The fracture transmissivity data acquired with the Posiva Flow Log (PFL) shown in Figure 2-14. The data are from the focused area/volume. As can be seen in the figure, there are hardly any conductive fractures below c –500 m elevation (the measurement limit if the PFL: c $T=1 \cdot 10^{-9}$ m^2/s). Other boreholes also indicate low frequencies of conductive fractures at depth, cf. /Rhén et al. 2008/ and the low frequency is illustrated in Figure 2-13.

Table 2-3. Transmissivity parameters used for all sets when matching measured PFL-f flow distributions. (Log base 10) /Rhén et al. 2008/.

Type	Description	Relationship	Parameters
Semi-correlated	Log-normal distribution about a power-law correlated mean	$\log(T) = \log(a\, r^{b}) + \sigma_{log(T)}\, N[0,1]$	a , b, $\sigma_{log(T)}$

[3] A telescopic approach is used for the single-hole hydraulic testing with the PSS method at Laxemar. Each borehole is measured with consecutive 100-m long, 20-m long and 5-m long packer intervals beginning with the longest packer interval. However, non-flowing 100-m long packer intervals are not studied with 20-m long packer intervals, etc. The telescopic measurement approach saves time but it assumes that low transmissive sections are correctly characterized. To display a cumulative plot of all 5 m sections a uniform distribution of transmissivity (T) is assumed in each low-transmissive 100 m or 20 m section and the corresponding unmeasured 5 m sections respectively, are a assigned a hydraulic conductivity (K) based on the measured larger measurement scales .

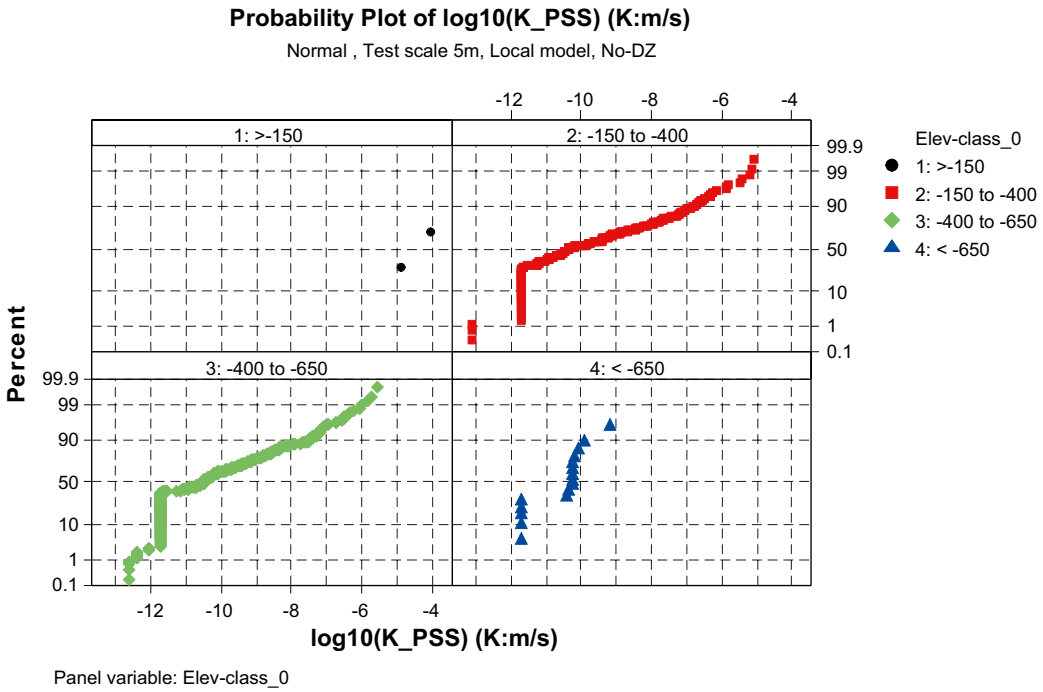

Figure 2-15. *Cumulative distribution plot of 631 log10(KPSS) data measured with a packer spacing (test scale) of 5 m between elevations 0 m to –1,000 m within the Local model volume in Laxemar, representing rock between deterministic deformation zones (Estimates of statistical distributions in /Rhén et al. 2008/).*

Table 2-4 provides detailed statistic of Terzaghi corrected frequencies (Terzaghi corrected to account for the bias in sampling fractures at different orientations to a given borehole, cf. e.g. /Rhén et al. 2008/) of flowing fractures (detected with the PFL method) in the Local area/volume and shows also the estimates of the fracture transmissivities, which in fact are the specific capacities of the flowing fractures. At repository depth (–400 to –650 m), the mean value of the Terzaghi corrected frequency of flowing fractures detected with the PFL method is low, approximately 0.1 fractures per metre. The geometric mean of the specific capacity is also low, approximately $1 \cdot 10^{-8}$ m^3/s per metre of head change, cf. Table 2-4. The product of these two values suggest an equivalent hydraulic conductivity of approximately $1 \cdot 10^{-9}$ m/s ($\sim 1 \cdot 10^{-16}$ m^2) for blocks of rock (between deterministic deformation zones) located between –400 to –650 m elevation. The validity of this simple calculation is confirmed by the measurements conducted with the PSS method shown in Figure 2-15. Table 2-5 provides a table of the schematic groundwater flow and solute transport characteristics under the current temperate climate conditions.

Table 2-4. Summary of transmissivity statistics of flowing features detected by PFL for the borehole intervals outside of interpreted deterministic deformation zones. MDZs are included in these statistics, but the transmissivity of individual PFL fractures are summed within an MDZ such that each is treated as a single feature. Modified after Tables 9-12 and 9-14 in /Rhén et al. 2008/).

Domain	Depth zone (m)	Min T m^2/s)	Max *T* (m^2/s)	Geometric mean (m^2/s)	PFL $P_{10,corr}$ (m^{-1})
HRD_EW007	50 to –150	4.4E–10	3.2E–05	3.58E–08	0.816
	–150 to –400	3.1E–10	3.7E–05	3.0E–08	0.550
	–400 to –650	7.9E–10	1.8E–06	2.6E–08	0.225
	–650 to –1,000	0.0E+00	0.0E+00	N/A	0.000
HRD_N	50 to –150	7.7E–10	6.5E–05	1.14E–07	0.773
	–150 to –400	8.3E–10	3.6E–05	7.4E–08	0.339
	–400 to –650	1.1E–09	5.2E–06	1.6E–08	0.115
	–650 to –1,000	1.3E–09	2.6E–08	4.6E–09	0.082
HRD_W	50 to –150	3.7E–10	4.6E–05	4.39E–08	0.499
	–150 to –400	1.1E–09	1.0E–05	1.4E–08	0.078
	–400 to –650	6.7E–10	9.2E–06	2.9E–08	0.060
	–650 to –1,000	3.7E–09	3.7E–09	3.7E–09	0.005
HRD_C	50 to –150	3.9E–10	3.8E–05	3.33E–08	0.564
	–150 to –400	3.7E–10	1.2E–05	1.1E–08	0.164
	–400 to –650	3.3E–10	1.1E–06	8.5E–09	0.107
	–650 to –1,000	1.5E–09	4.4E–07	2.3E–08	0.008

Table 2-5. Schematic summary of groundwater flow and solute transport characteristics under the current temperate climate conditions. Based on /Rhén et al. 2009/.

Depth zone	General characteristics
dZ1: > –150 m	Near-surface rock, characterised by a high intensity of conductive fractures. Sub-horizontal and steeply dipping fractures striking WNW dominate.
	Advection dominated – high groundwater flow rates with sub horizontal fracturing giving $K_h > K_v$ in many areas. Flushed by post-glacial meteoric water. High fracture intensity implies matrix blocks 1–2 m in size, which gives equilibrium in salinity between fracture and matrix on timescales of ~1,000 years.
dZ2: –150 m to –400 m	Intermediate-depth rock, characterised by an intermediate intensity of conductive fractures. Steeply dipping fractures striking WNW dominate except in HRD_W where no set is clearly dominant and in HRD_N and HRD_C the sub horizontal set is also important beside the WNW set.
	Some advection, but rock matrix diffusion (RMD) retards post-glacial meteoric penetration. Fracture intensity is generally much lower, reducing groundwater flux and increasing matrix blocks to typically ~5 m in size, such that porewater chemistry lags behind that of the fracture water by 1,000s of years.
dZ3: –400 m to –650 m	Rock at repository level, characterised by a low intensity of conductive fractures. Steeply dipping fractures striking WNW dominate except for HRD_W where no set is clearly dominant.
	Low advection. RMD important because advective flow rates are small. Fracture intensity lower still, with typical matrix blocks ~10 m in size, such that porewater chemistry lags behind that of fracture water ~10,000 years.
dZ4: < –650 m	Deep rock, characterised by a sparse network of conductive fractures. Steeply dipping fractures striking WNW dominate except for HRD_W where no set is clearly dominant (however rather few data occur within dZ4).
	Very low advection. RMD dominates Fracture intensity very low, with typical matrix blocks ~100 m in size, such that porewater chemistry lags behind that of fracture water ~100,000 years.

2.3 Summary of the Quaternary deposits hydrogeological model (HSD)

The stratigraphical distribution of Quaternary deposits in the investigated area is rather uniform. Till is the oldest Quaternary deposit in the area, and is consequently resting directly upon the bedrock surface. The till in the valleys is often overlain by glacial clay, which in many valleys is overlain by a thin layer of sand followed by clay gyttja and peat.

The model developed by /Nyman et al. 2008/ contains six layers of Quaternary deposits, denoted Z1–Z6; Z1 represents the upper layer of the Quaternary deposits. These layers, illustrated in the cross section in Figure 2-16, are defined and described briefly in /Rhén et al. 2009/ and in /Nyman et al. 2008, Sohlenius and Hedenström 2008/.

Figure 2-17 shows the modelled distribution of total overburden depth in the Laxemar-Simpevarp regional model area. Figure 2-18 illustrates the variable depth of the Quaternary deposits along a vertical north-south section across the E-W regional deformation zone in the northern part of the local model domain; the Mederhult zone (ZSMEW002A).

This detailed Quaternary deposit model was simplified in the SDM-Site regional groundwater flow modelling representing it by four element layers vertically, each of a constant 1 m thickness, with the horizontal extent of the hydrogeological grid element (40–120 m), to represent the HSD. The same hydraulic conductivity tensor was specified for each element in a vertical stack of 4 grid elements, but varied horizontally from element-to-element, and was anisotropic with regard to horizontal and vertical components in order to represent the effective hydraulic properties of the Quaternary deposit layers. The effective hydraulic conductivity tensor for the soil package was calculated according to the actual modelled thickness of the layers of the Quaternary deposits and the hydraulic conductivities of the soil types at that location. HSD properties used in the SDM-Site *base case model* are illustrated in Figure 2-19.

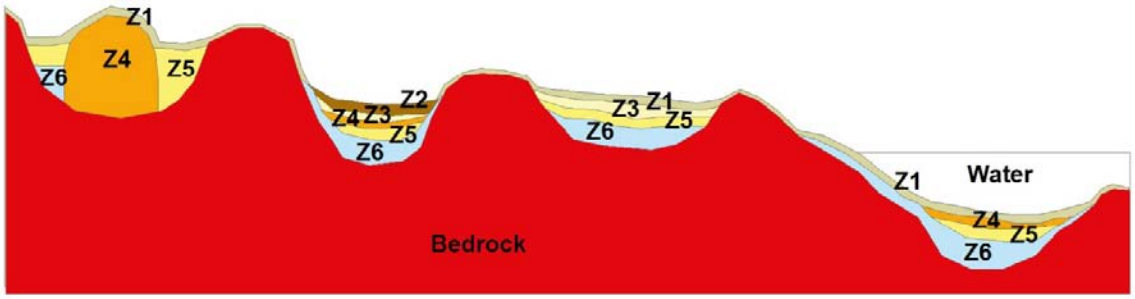

Figure 2-16. *The stratigraphical model which was used for modelling stratigraphy and total depth of Quaternary deposits in the Laxemar-Simpevarp regional model area. /Sohlenius and Hedenström 2008/. Layer Z1-6:*

Layer Z1 represents a thin surface(-affected) layer.

Layer Z2 represents (fen or bog) peat.

Layer Z3 represents postglacial clay, clay gyttja/gyttja clay, gyttja or recent fluvial sediments.

Layer Z4 represents postglacial sand/gravel, glaciofluvial sediments or artificial fill.

Layer Z5 represents glacial clay.

Layer Z6 represents (glacial) till.

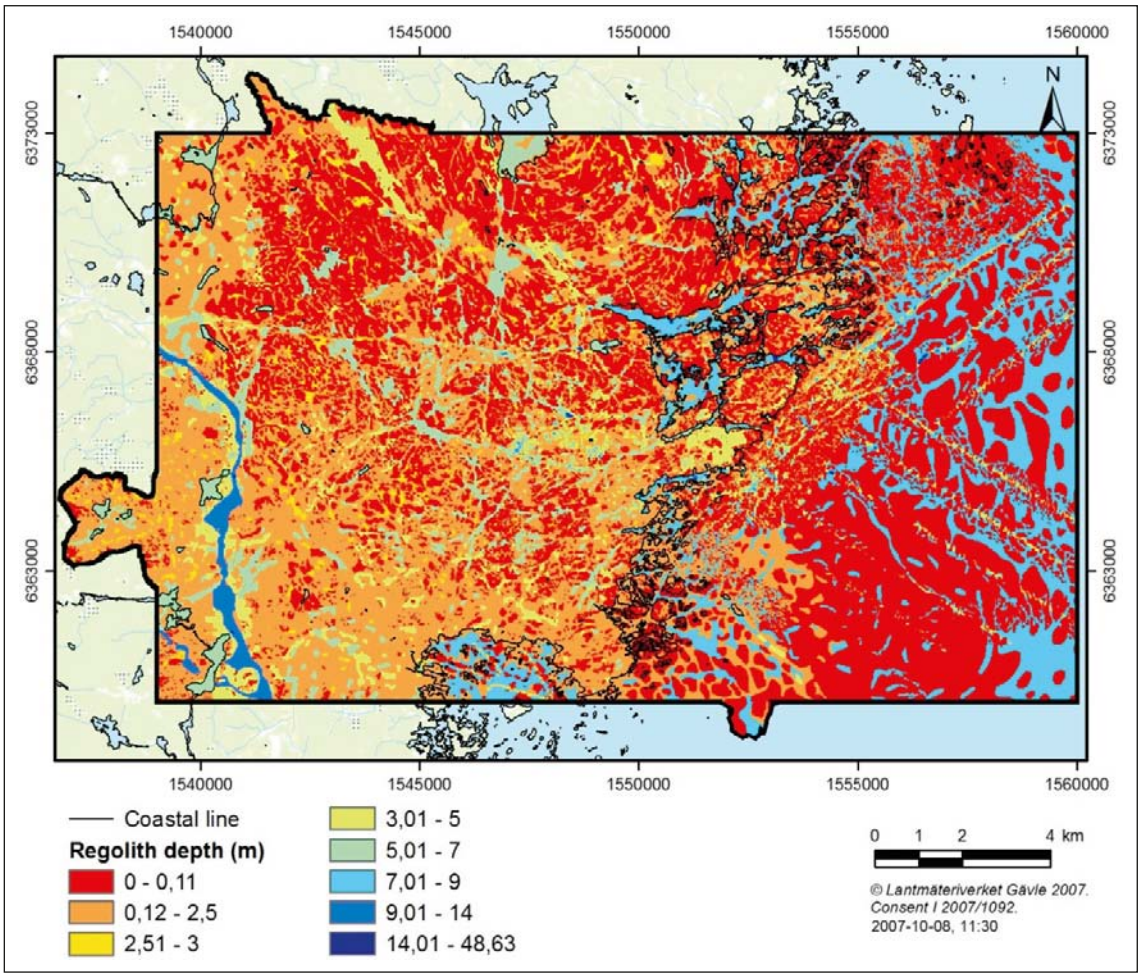

Figure 2-17. *The modelled distribution of total depths of the Quaternary deposits in the Laxemar-Simpevarp area. /Sohlenius and Hedenström 2008/.*

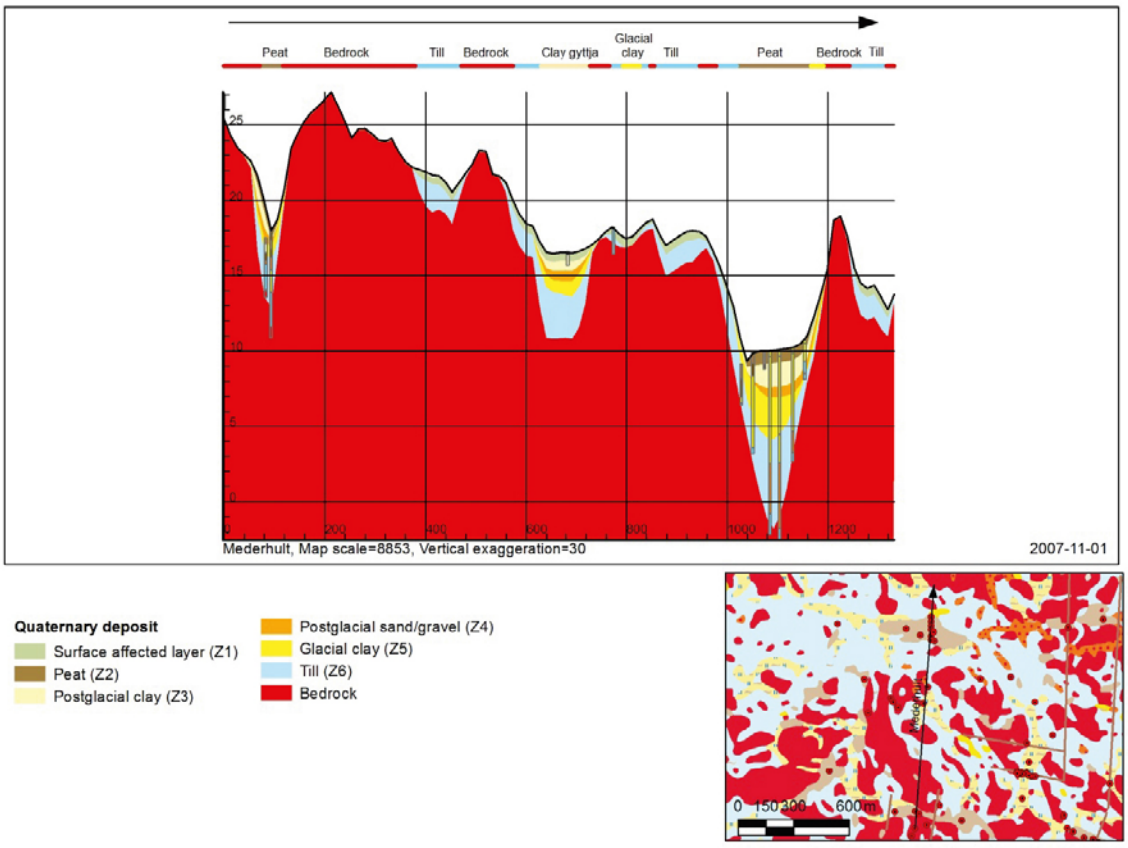

Figure 2-18. *The profile shows the total depth and stratigraphy of the Quaternary deposits in a north-south profile close to Mederhult. The valley in the right part of the profile (between 1,000 and 1,200 on the horizontal scale) is one of the largest lineaments in the model area (ZSMEW002A , cf. /Rhén et al. 2009, Figure 3-1 therein/), /Sohlenius and Hedenström 2008/.*

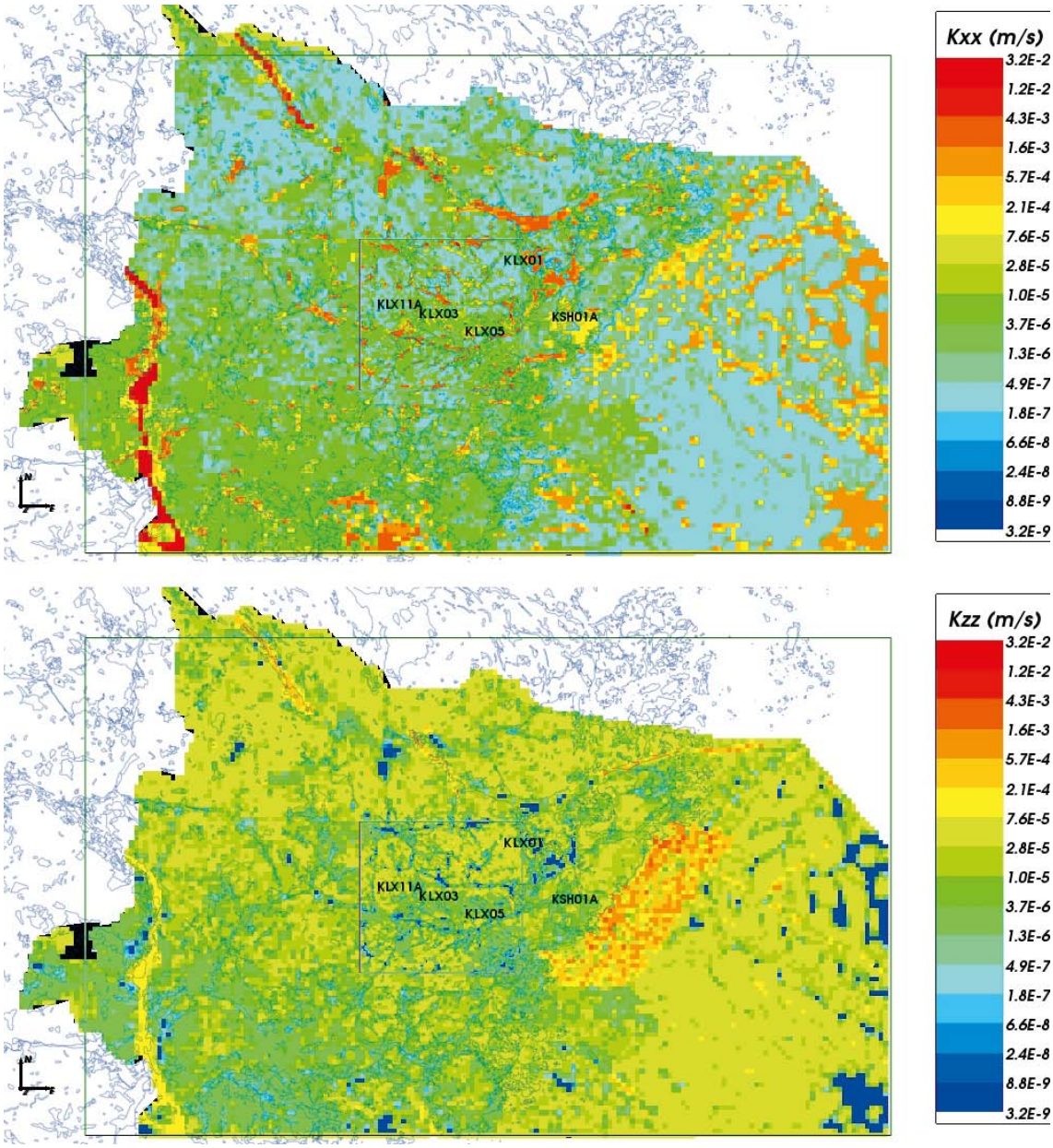

Figure 2-19. *Resulting effective hydraulic conductivity for HSD top layer based on layer thicknesses and hydraulic properties of the Quaternary deposits. Top: E-W horizontal component; Bottom: vertical component. /Rhén and Hartley 2009/.*

3 Assessment of model properties due to increased model domain

3.1 Hydrochemistry

The bedrock is investigated to approximately –1,600 m elevation, though most investigations are down to approximately –1,000 m at Laxemar, see Figure 3-1. The measured fracture water salinity at –1,000 m elevation is approximately 2.5%. At repository depth, the fracture water salinity is approximately 1.0%.

The deepest borehole investigated by SKB is borehole KLX02 at Laxemar. The vertical depth of KLX02 is 1,660 m and the salinity at the bottom of KLX02 is approximately 8%, see Figure 3-1.

Highly saline waters (TDS>100 g/L) are found in many places below c 1,000–2,000 m /Juhlin et al. 1998, Figure 13-1, Smellie 2004, Section 3-4/, which indicate that values observed in KLX02 at depth is not uncommon, cf. Figure 3-1.

Interpretation of hydrochemical data from Forsmark and Laxemar have indicated very old ground waters at c 600–1,000 m depth or deeper /Laaksoharju et al. 2009/, but data from other sites also indicate that groundwaters are very old deeper than 1,000–2,000 m /Juhlin et al. 1998, Smellie 2004, Smellie et al. 2008/, indicating low or insignificant groundwater flow.

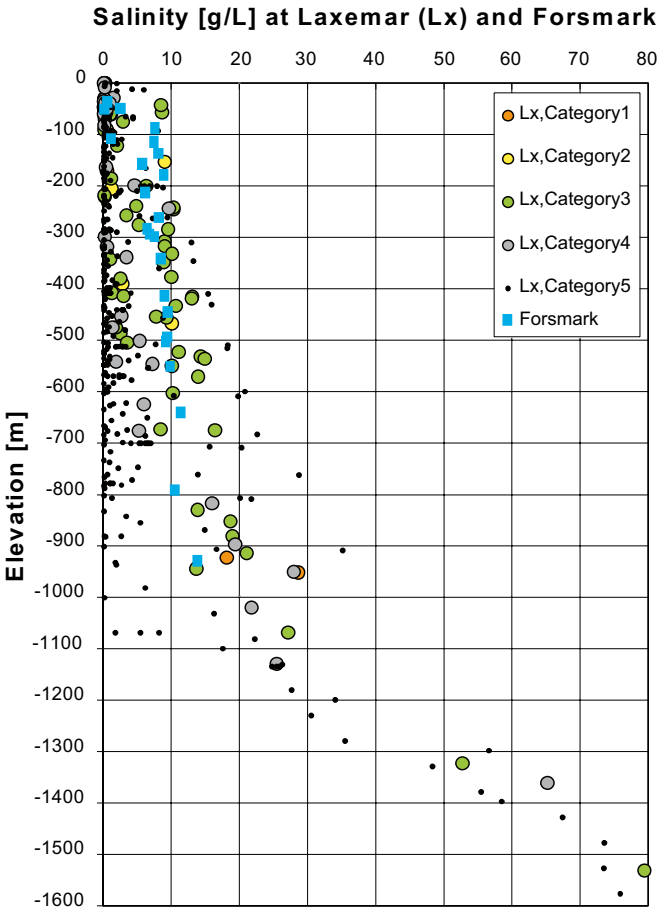

Figure 3-1. *Plot of all available salinity data from the core-drilled boreholes and percussion-drilled boreholes in Laxemar sorted according to quality category and in seven boreholes at Forsmark. The data in Laxemar are classified into five categories with regard to the quality of the sampling and/or analysis method, where category 1 represent the best quality and category 5 is the poorest. The Forsmark data are all of good quality in this regard (category 3 or better). (Modified after Figure 5-15 in /Follin et al. 2008/ and Figure 5-18 in /Rhén et al. 2009/.). Same as Figure 1-2.*

3.2 Hydraulic properties below the SDM-Site Laxemar

The information on properties below –1,000 m elevation is limited and below –1,600 m elevation no site specific information is available. The trends presented in /Rhén et al. 2008/ are based on data above –1,000 m and all usage below that elevation must therefore be viewed as uncertain.

The trend however could be used to put some constraints on the scatter on data at great depth at the SDM Laxemar site. On the hundred metre scale, the interval of expected hydraulic conductivity is reasonably argued to be within $1 \cdot 10^{-12}$ m/s and $1 \cdot 10^{-9}$ m/s at the depth of –4,000 metre elevation.

3.2.1 Deep properties as indicated from other sites than Laxemar

There are a few sites around the world with deep holes in crystalline rock that can provide indications of properties below 1,000 m depth.

Permeability of the rock is considered to decrease by depth, and sites in Gravberg (Sweden) and Kola (Russia) located in the Baltic Shield indicate hydraulic conductivities of c 10^{-10} m/s or lower below c 2,000 m depth /Juhlin et al. 1998/. The KTB site in the western margin of the crystalline Bohemian Massif indicate a slight higher permeability compared to Gravberg and Kola /Juhlin et al. 1998, Fig 10-1, Smellie 2004, Fig 3-4/.

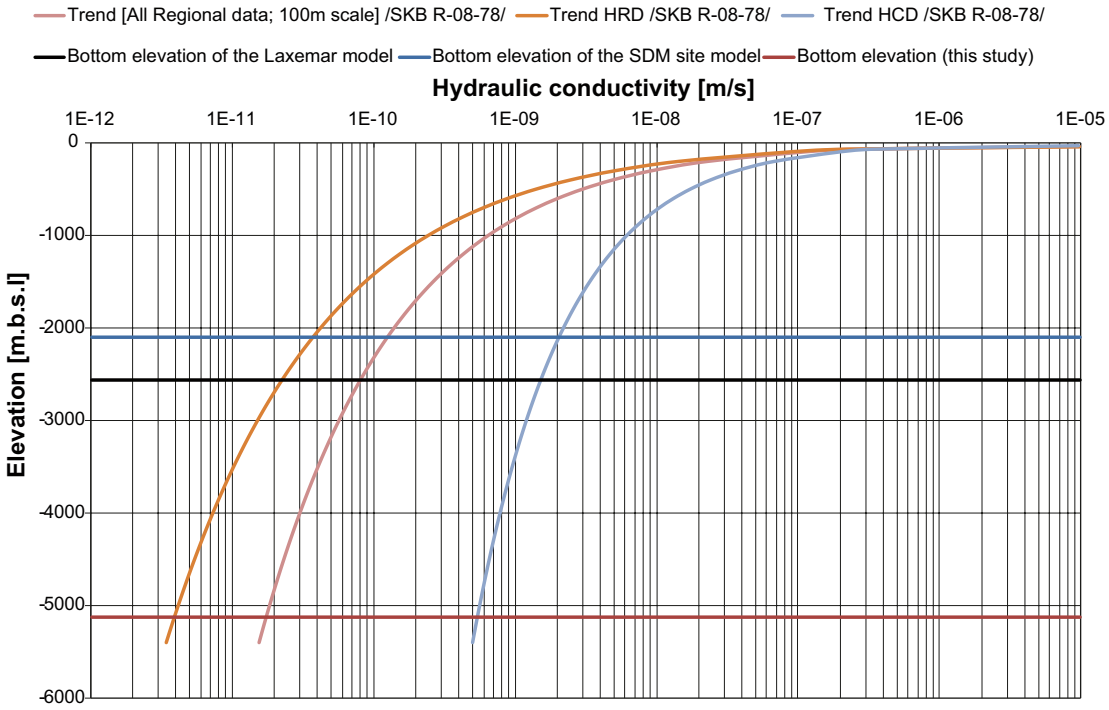

Figure 3-2. *Illustration of the assessed depth trends presented in /Rhén et al. 2008/.*

3.3 Extended SDM deformation zone model

The extended deformation zone model was constructed as follows:

The official regional deformation zone model from the Approved catalogue on SIMON[4] was extended down to a depth of 5,200 m by re-modelling and re-trimming all of the zones as hydrological surfaces, without thickness, and by applying the following cut-off depth criteria:

- Zones with length less than 2,000 m are cut-off at –1,500 m depth.
- Zones with length between 2,000 and 3,000 m are cut-off at –2,100 m depth.
- Zones with length greater than 3,000 m are cut-off at 5,200 m depth.

Some exceptions were made and explained as:

If a zone extends beyond the regional model boundary then it was extended to the bottom of the model volume (–5,200 m) since its actual length is highly uncertain.

The minimum length criterion for the Regional deformation zone model was 1,500 m. Four zones in the regional model have lengths shorter than 1,500 m but were subsequently included to allow better geological understanding for those using the model. These zones were ZSMEW120A, ZSMEW120A, ZSMNE063A and ZSMNE065A.

The official regional deformation zone model on SIMON has 171 modelled zone objects. The extended (5,200 m) model has 170 modelled zone objects. The difference lies in the fact that for geometrical reasons when re-modelling ZSMNS001C and ZSMNS001D from the original model have been combined to create a single DZ object ZSMNS001CD in the modified model.

[4] Database of SKB.

4 Surface conditions during glacial conditions

4.1 Conceptual model for the present work

The reference evolution in /SKB 2006a, SKB 2010/ considers permafrost conditions in front of an advancing ice sheet margin. However, a Glacial case without permafrost produces the largest hydraulic gradients at the ice sheet margin, hence the greatest effects on the studied performance measures with regard to Darcy flux and fracture (advective) flow salinity. Therefore, herein only a Glacial case without permafrost is investigated.

An infinite source of meltwater with a hydraulic head at the base of the ice sheet equal to 92% of the ice sheet thickness is assumed at all times in all simulations. The use of 92% of the ice sheet thickness reflects a situation where the sub-glacial pressure equals the ice sheet weight; hence the ice sheet practically floats on a thin layer of highly pressurised water at this boundary. The imposed boundary condition implies that sub-glacial meltwater infiltrates the sub-surface and flows from areas with high hydraulic heads to areas with lower hydraulic heads, where it discharges.

The conceptual model of the top boundary condition for the work reported here are summarised in the section below.

The model domain is approximately 5,200 metres deep. The local site information below –1,000 metres elevation is sparse and below approximately –1,600 metres elevation absent. The properties and initial conditions at elevations deeper than those depths are based on extrapolation of depth trends established on site data in the upper kilometre. At the model domain bottom, i.e. at –5,120 metres elevation, conditions are assumed to be stable at all times and the properties are assumed homogeneous and fairly low as compared with the detailed knowledge available in the upper kilometre.

Also, in accordance with the climate modelling in /SKB 2010/, sub-glacial runoff through structures embedded in the ice sheet or occurring at the ice/bedrock interface, e.g. sub-glacial meltwater tunnels, are not considered here.

The groundwater flow modelling of glacial climate conditions can be divided into three stages, pre-LGM[5], LGM and post-LGM. During the pre-LGM stage, either frozen (permafrost) or unfrozen (no permafrost) conditions can be considered. During the LGM stage, the model domain is completely covered by a thick ice sheet for thousands of years. During the post-LGM stage, submerged conditions are considered in the area in front of the retreating ice sheet margin. The glacial cycle simulated at Laxemar in /Vidstrand et al. 2010b/ comprise approximately 13,000 years between the first ice front passage until the site once again becomes ice free, however sub-merged beneath a fresh water lake.

For the present report the following is valid concerning simulations carried out:

- **Pre-LGM stage.** Advance from north-west. No permafrost.
- **LGM stage.** Not simulated.
- **Post-LGM stage.** Not simulated.

Figure 4-1 illustrates the considered scenario, without permafrost.

[5] LGM is a standard acronym used to denote the glacial maximum of the last glaciation (Weichsel), cf. /SKB 2010/.

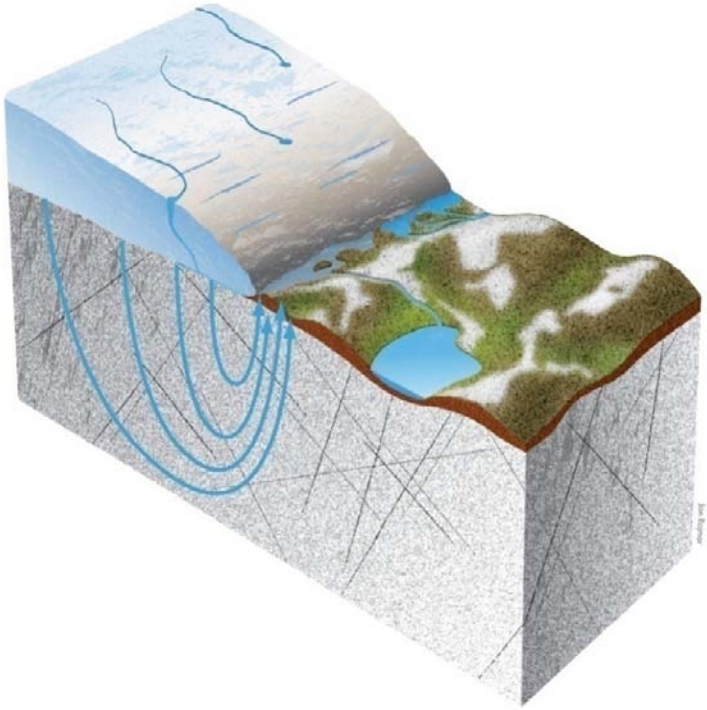

Figure 4-1. *Groundwater discharge for an advancing ice sheet margin occurs predominantly close to margin if there is no permafrost in the periglacial area.*

4.2 Ice sheet profile

Compared to present-day the key boundary condition during a glacial cycle is the thickness and the properties of the ice sheet (warm or cold based). The thickness and the properties affect all processes involved regardless of whether they are thermal (T), hydraulic (H), mechanical (M) or chemical (C). Below follows a short description of how the ice sheet profile is defined in the modelling work reported here.

Beneath the ice sheet, the pressure is specified using theoretical/empirical ice sheet thickness relationships /Paterson 1994/. This approach has been used in various earlier numerical groundwater flow simulations and is, in general, believed to overestimate the impact of an ice sheet, e.g. /Chan et al. 2005/.

/Paterson 1994/ reported two possible equations for expressing the ice sheet thickness. If the ice is assumed to be a perfectly plastic material the ice thickness adjusts to the shear stress at the base. For such conditions, the ice thickness can be expressed as:

$$h^2 = \frac{2 \cdot \tau_0}{\rho g} \cdot (L - x) \qquad (4\text{-}1)$$

where h [L] is the ice thickness at location x; L [L] is the size of the ice sheet between the front and its centre (origin of x). Hence, (L-x) is the distance backward from the ice sheet margin. τ_0 [$MT^{-2}L^{-1}$] is the shear stress at the base. Values on the shear stress are reported between 0 and 100 kPa with a mean at about 50 kPa /Paterson 1994/. Adopting 50 kPa yields:

$$h = 3.4 \cdot \sqrt{L - x} \qquad (4\text{-}2)$$

Equation 4-2 has previously been assessed in hydrogeological studies by SKB either as a specified head boundary condition e.g. /Vidstrand et al. 2007/ or as a criterion for assigning a head dependent flux, e.g. /Jaquet and Siegel 2006/.

If the assumption of perfect plasticity is dropped another equation for ice thickness is obtained:

$$h = H \cdot \left(1 - \left(\frac{x}{L} \right)^{\frac{4}{3}} \right)^{\frac{3}{8}} \qquad (4\text{-}3)$$

where H [L] is the ice sheet thickness at the centre and L [L] is the maximum ice sheet horizontal extension.

Equation 4-3 is applied in the rock mechanics modelling conducted by /Lönnqvist and Hökmark 2010/ and in groundwater flow modelling conducted by /Vidstrand et al. 2010a, b/, who set H to 3 km and L to 400 km. For the sake of comparison, Equation 4-3 yields an ice sheet thickness approximately twice the thickness of Equation 4-1.

Figure 4-2 shows the three ice sheet profiles discussed in /Vidstrand et al. 2010b/.

- The red graph is the so-called "theoretical maximum profile" presented in /SKB 2010/. This profile is considered valid for the pre-LGM stage (an advancing ice sheet margin) and is readily modelled by Equation 4-3. The dotted red line represents the specified pressure head curve assigned on the top boundary in the majority of the groundwater flow simulations reported here. The pressure head is set to 92% of the ice sheet thickness.
- The blue graph represents the shape of the "theoretical maximum profile" when the ice sheet margin has reached the last glacial maximum (LGM) south of the Baltic Sea. The solid black line represents the tangent to the blue graph at a location corresponding to the Laxemar site. During the period of complete ice sheet coverage at Laxemar, the slope of the tangent (2.1 m/km) is used to model the ice sheet profile in the work reported here.
- The green graph mimics the "simulated reference climate evolution profile" presented in /SKB 2010/. This profile is considered valid for the post-LGM stage (a retreating ice sheet margin) and applicable for describing ice thickness in terrestrial areas, i.e. areas that are unaffected by the increase in the sea level caused by the abundance of melt water.

In the work reported here, only the "theoretical maximum profile" is used.

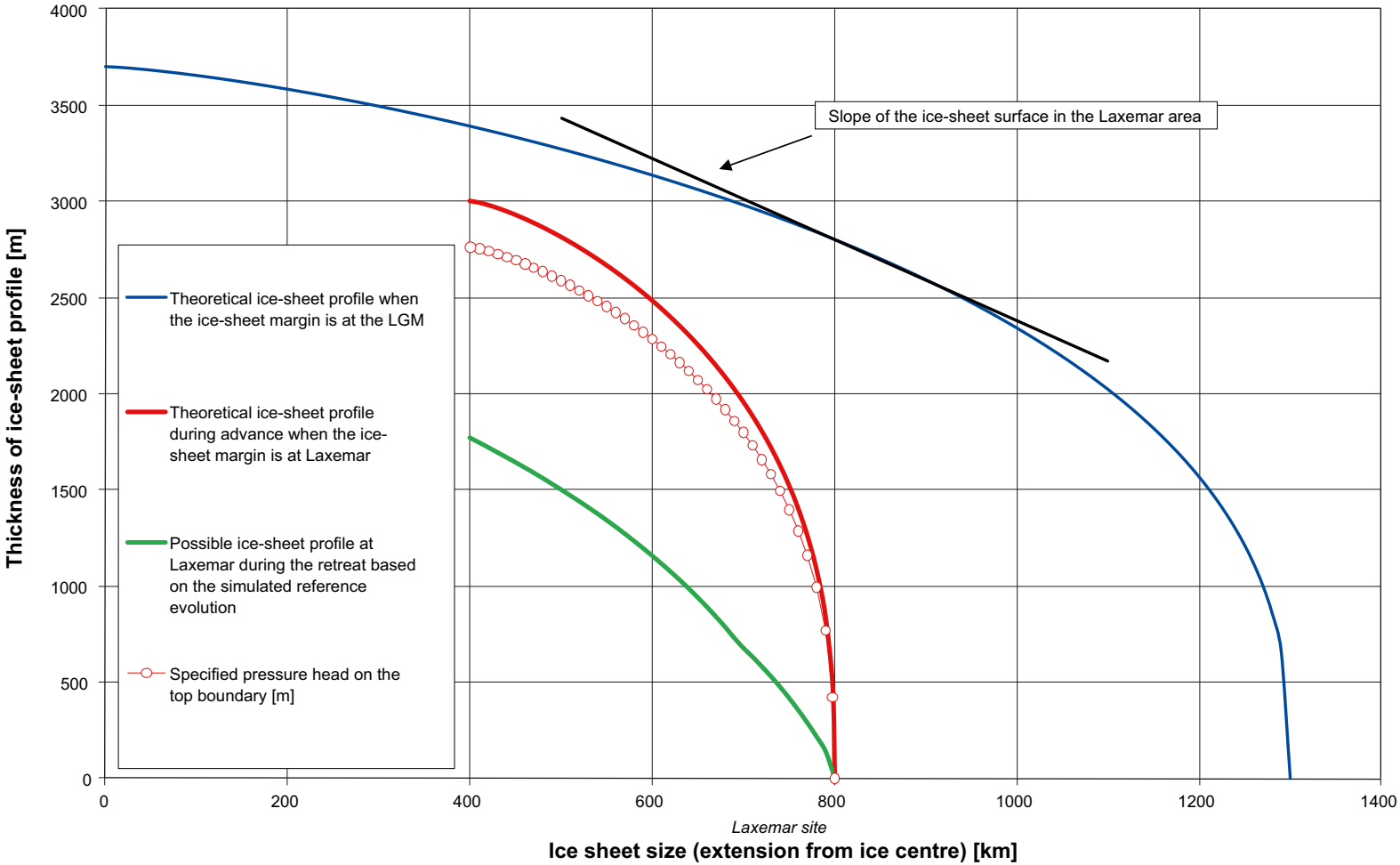

Figure 4-2. *Illustration of ice sheet profiles.*

5 Concepts and methodology

5.1 Governing equations

Coupled groundwater flow and salt transport in fractured rocks that give rise to variations in salinity and hence fluid density are modelled in DarcyTools according to the following formulation of the mass conservation equation:

$$\frac{\partial \rho\phi}{\partial t} + \frac{\partial}{\partial x}(\rho u) + \frac{\partial}{\partial y}(\rho v) + \frac{\partial}{\partial z}(\rho w) = Q \tag{5-1}$$

where ρ is fluid density [ML^{-3}], ϕ is the kinematic porosity [–], t is time [T], (u, v, w) are the directional components of the volumetric (Darcy) flux **q** [LT^{-1}] at the location (x, y, z) [L,L,L] in a Cartesian coordinate system, and Q is a source/sink term per unit volume of fluid mass [$ML^{-3}T^{-1}$]. The mass conservation equation is turned into a pressure equation by invoking the assumptions behind Darcy's law:

$$\begin{aligned} \rho u &= -\frac{K_x}{g}\frac{\partial P}{\partial x} \\ \rho v &= -\frac{K_y}{g}\frac{\partial P}{\partial y} \\ \rho w &= -\frac{K_z}{g}\frac{\partial P}{\partial z} - K_z(\rho - \rho_0) \end{aligned} \tag{5-2}$$

where K_x, K_y and K_z are the orthogonal components of the hydraulic conductivity tensor parallel to the Cartesian coordinate system [LT^{-1}], g is the acceleration due to gravity [LT^{-2}], ρ_0 is a reference fluid density [ML^{-3}], and P is the residual (dynamic) fluid pressure [$ML^{-1}T^{-2}$] at the location (x, y, z):

$$P = p + \rho_0 g z \tag{5-3}$$

where p is the gauge pressure [$ML^{-1}T^{-2}$] and $\rho_0 g\, z$ is the hydrostatic pressure, P_0.

The hydraulic conductivity K is related to the permeability k [L^2] through the relation:

$$K = \frac{\rho\, g}{\mu} k \tag{5-4}$$

where μ is the fluid dynamic viscosity [$ML^{-1}T^{-1}$]. For variable-density flow at isothermal conditions, ρ and μ are given by the following state laws:

$$\rho = \rho_0[1+\alpha C] \tag{5-5}$$

$$\mu = \mu_0 \tag{5-6}$$

where α and μ_0 are constants and C represents the salinity (mass fraction) [–]:

$$C = TDS/\rho \tag{5-7}$$

The migration of salt is modelled in DarcyTools in terms of advection and dispersion processes in the mobile (fracture) pore system and as a diffusion process in the immobile (rock matrix) pore system. The advection-dispersion equation for the mobile pore system is modelled in DarcyTools according to the following equation:

$$\begin{aligned} \rho\phi\frac{\partial C}{\partial t} &+ \frac{\partial}{\partial x}\left(\rho u C - \rho\gamma D_x \frac{\partial C}{\partial x}\right) \\ &+ \frac{\partial}{\partial y}\left(\rho v C - \rho\gamma D_y \frac{\partial C}{\partial y}\right) \\ &+ \frac{\partial}{\partial z}\left(\rho w C - \rho\gamma D_z \frac{\partial C}{\partial z}\right) = QC + Q_C \end{aligned} \tag{5-8}$$

where D_x, D_y and D_z are the orthogonal components of the diffusion tensor parallel to the Cartesian coordinate system [L^2T^{-1}], QC and Q_C are source/sink terms per unit volume of fluid mass [$ML^{-3}T^{-1}$], where Q_C represents the diffusive exchange of salt per unit volume of fluid mass between the mobile and immobile pore volumes [$ML^{-3}T^{-1}$], and γ is a dimensionless coefficient that describes the dependency of the kinematic porosity of the mobile pore system on the dynamic pressure:

$$\phi = \phi_0 \, \gamma \tag{5-9}$$

$$\gamma = 1 + \frac{S_s}{\phi_0} \frac{(P - P_0)}{\rho g} \tag{5-10}$$

where ϕ_0 [–] is the initial kinematic porosity, S_s is the specific storage of the conductive pore system [L^{-1}].

It is noted that the concept of longitudinal and transverse hydrodynamic dispersion (dispersivity) is not considered in DarcyTools, see Equation 5-8.

5.2 Methodology

5.2.1 Finite volume method

DarcyTools uses a staggered computational grid, which means that scalar quantities such as pressure, flow porosity and salinity use a cell-centred mesh, whereas directional quantities such as hydraulic conductivity, hydrodynamic diffusivity, mass flux, and Darcy flux use a mesh centred at the cell walls. This grid arrangement was first introduced by /Harlow and Welch 1965/ and is described in textbooks, e.g., /Patankar 1980/. Each variable is assumed to be representative for a certain control volume, which is the volume for which the equations are formulated. DarcyTools uses the finite volume method to transform the differential equations into algebraic equations of the type:

$$a_P \, \Phi_P = a_W \, \Phi_W + a_E \, \Phi_E + a_S \, \Phi_S + a_N \, \Phi_N + a_B \, \Phi_B + a_T \, \Phi_T + S_\Phi \tag{5-11}$$

where Φ denotes the variable in question, a_i are direction coefficients (West, East, South, North, Bottom, and Top) and S_Φ represents source/sink terms. The equations are solved by the MIGAL multi-grid equation solver.

5.2.2 Continuum representation of hydraulic properties of discrete fractures

Principle

The principle used to represent hydraulic properties of discrete fractures as equivalent grid cell hydraulic properties in DarcyTools works as follows:

A fracture variable (P_f) contributes to the grid cell variable (P_c) by an amount which is equal to the intersecting volume of the fracture (V_f) times the value of the fracture variable. Contributions from all fractures (N) that intersect the grid cell control volume are added and the sum is divided by the volume of the cell (V_c), i.e.:

$$P_c = \sum_{i=1}^{N} \left(V_f \, P_f \right)_i / V_c \tag{5-12}$$

The intersecting volume of the fracture f may be written as:

$$V_f = L_f \, W_f \, b_f \tag{5-13}$$

where L_f, W_f and b_f denote the physical dimensions (length, width and thickness) of the intersecting fracture in three orthogonal directions. For the sake of simplicity, it is assumed in the equations below that the fracture thickness b_f is much thinner than the geometrical resolution of the computational grid (the grid size).

Grid-cell hydraulic conductivity

DarcyTools assumes that fracture transmissivity (T_f) is a scalar quantity and that fracture hydraulic conductivity (K_f) may be written as:

$$K_f = T_f / b_f \tag{5-14}$$

Thus, the contribution from an intersecting fracture to the hydraulic conductivity of the intersected grid cell may be written as:

$$K_{c,f} = (L_f W_f T_f) / V_c \tag{5-15}$$

As DarcyTools uses a staggered computational grid, $K_{c,f}$ is a directional quantity.

Grid-cell kinematic porosity and fracture aperture

The contribution from an intersecting fracture, deterministic or stochastic, to the kinematic porosity of the intersected grid cell can approximately be written as:

$$\phi_{c,f} = (L_f W_f e_{T,f}) / V_c \tag{5-16}$$

where $e_{T,f}$ is the fracture transport aperture. In SDM-Site, a power-law function between the fracture aperture and the fracture transmissivity was assumed:

$$e_{T,f} = a\,(T_f)^b \tag{5-17}$$

with a = 0.46 and b = 0.5 /Dershowitz et al. 2003/.

In the work reported here, the transport apertures of the deterministically modelled deformation zones are based on Equation 5-17, whereas all stochastically modelled zones and fractures are given a constant transport aperture of $1 \cdot 10^{-4}$ m, see Appendix A for details.

Fracture transmissivity

The equations given above reveal that fracture transmissivity is the key hydraulic quantity in DarcyTools, i.e. fracture transmissivity is used to define both grid cell hydraulic conductivity and grid cell kinematic porosity.

DarcyTools assumes that a power-law function prevails between fracture transmissivity and fracture size (L_f). The power-law function may be written as /Svensson et al. 2010/:

$$\log(T_f) = \log\left[a_T \left(\frac{L_f}{100} \right)^{b_T} \right] + d_T\, U[-0.5,0.5] \tag{5-18}$$

where a_T is the transmissivity value of a fracture with L_f = 100 m and b_T is the exponent of the power-law function. d_T is a factor that scales a uniformly distributed[6] random deviate U and is used when uncertainty in the power-law function is addressed.

For the sake of clarity it is noted that the relationship between the power-law parameters used in DarcyTools (a_T,b_T) and the corresponding power-law parameters (a,b) derived in SDM-Site can be written as:

$$b_T = b \tag{5-19}$$

$$a_T = a\left(100/\sqrt{\pi}\right)^{b_T} \tag{5-20}$$

[6] In SDM-Site, the values of the random deviate were generated by means of a truncated normal distribution. This difference, normal vs. uniform, is considered insignificant in the work reported here.

5.2.3 Exchange of dissolved solids

In DarcyTools, the exchange of dissolved solids between the fracture water and the matrix porewater is modelled with a one-dimensional multi-rate diffusion model /Haggerty and Gorelick 1995/. The diffusion process is represented by a series of discrete exchange rate coefficients, α_{min}-α_{max} [T^{-1}], where the time scale of the remotest diffusive exchange is $1/\alpha_{min}$. Another parameter governing the diffusion process in the model of /Haggerty and Gorelick 1995/ is the ratio between the diffusive and advective pore spaces, β [–]. In fractured crystalline rock, the matrix porosity is approximately 10–100 times greater than the kinematic porosity /Follin et al. 2005/.

The chosen range of values of the exchange rate coefficients not only affects the time scales but also the penetration depths of the multi-rate diffusion process. In the work reported here, the value of α_{min} is set to $4 \cdot 10^{-12}$ s^{-1}, which implies a time scale of approximately 8,000 years for the remotest diffusive exchange, and the value of β is set to 10, i.e. ten times more pore space in the matrix than in the fractures.

6 Model specifications

6.1 Studied cases

In addition to the Glacial case without permafrost, a Temperate case is also studied. The Temperate case serves as a reference for the performance measures studied in the Glacial case without permafrost. Hence, the key "climate events" looked at in this work are:

- *Temperate* (used as a reference).
- *Glacial case without permafrost.*

Nine cases (variants) with different hydraulic properties have been tested as a sensitivity exercise in order to investigate the effect of properties and initial conditions on the stability of the hydro-geological and hydrochemical environment at great depths. In these simulations, the size of the model domain is not varied, i.e. it is fixed, and the resolution of the computational grid is not varied.

Table 6-1 illustrates how the variants relate to each other; Table 6-2 lists the nine variants and their main characteristics, also illustrated in Figure 6-1 and Figure 6-2. The initial conditions for salinity of the main variants can be considered as a minimum case for salinity at depth. This since data from other sites indicate that it is probably larger than assumed below some 2,000 m. Sub-variants b with a linear increase towards depth can possibly be seen as an upper bound case considering available data from other sites, cf. /Juhlin et al. 1998/ and /Smellie 2004/, states that TDS > 100 g/L is observed in several places below a depth of c 4,000 m.

Each of the variants is further described below in Section 6.1.1 up to 6.1.5.

Table 6-1. Overview of the five main variants and their sub-variants yielding in total nine reported variants in this study. The main characteristics of the variants are listed in Table 6-2.

Tested sub-variants / Main variants		Sub-variant b (increased salinity at depth)	Sub-variant c increased cell porosity	Sub-variant d Increased HCD transmissivity
Variant 1	X	X		
Variant 2	X	X	X	
Variant 3	X			X
Variant 4	X			
Variant 5	X			

Table 6-2. Overview of the nine studied variants. The main characteristics concerning hydraulic conductivity and salinity are visualised in Figure 6-1 and Figure 6-2, respectively.

Variant	Main characteristics
Variant 1	• No deformation zones present below –2,100 m elevation • Less permeable at depth (see Figure 6-1) – $5 \cdot 10^{-10}$ between –2,100 and –2,300 m – $5 \cdot 10^{-11}$ between –2,300 and –5,120 m • Less saline at depth (see Figure 6-2) – Initial conditions fixed at 7.2% below –2,100 m • Bottom boundary condition of salt specified as fixed salinity of 7.2%.
Variant 1b	• No deformation zones present below –2,100 m elevation • Less permeable at depth (see Figure 6-1) – $5 \cdot 10^{-10}$ between –2,100 and –2,300 m – $5 \cdot 10^{-11}$ between –2,300 and –5,120 m • Increasing salinity with depth (see Figure 6-2) – Initial conditions fixed at 7.2% at –2,100 m, increasing with gradient (0.0037%/metre) • Bottom boundary condition of salt specified as fixed salinity of 18.5%.

Variant	Main characteristics
Variant 2	• No deformation zones present below –2,100 m elevation • More permeable at depth (see Figure 6-1) – $9 \cdot 10^{-10}$ between –2,100 and –2,300 m – $5 \cdot 10^{-10}$ between –2,300 and –5,120 m • Less saline at depth (see Figure 6-2) – Initial conditions fixed at 7.2% below –2,100 m • Bottom boundary condition of salt specified as fixed salinity of 7.2%.
Variant 2b	• No deformation zones present below –2,100 m elevation • More permeable at depth (see Figure 6-1) – $5 \cdot 10^{-10}$ between –2,100 and –2,300 m – $5 \cdot 10^{-11}$ between –2,300 and –5,120 m • Increased salinity with depth (see Figure 6-2) – Initial conditions fixed at 7.2% at –2,100 m, increasing with gradient (0.0037%/metre) • Bottom boundary condition of salt specified as fixed salinity of 18.5%.
Variant 2c, increased cell porosity	• No deformation zones present below –2,100 m elevation • More permeable at depth (see Figure 6-1) – $9 \cdot 10^{-10}$ between –2,100 and –2,300 m – $5 \cdot 10^{-10}$ between –2,300 and –5,120 m • Less saline at depth (see Figure 6-2) – Initial conditions fixed at 7.2% below –2,100 m • Each numerical cell porosity multiplied with a factor 5 • Bottom boundary condition of salt specified as fixed salinity of 7.2%.
Variant 3	• Steeply deeping deformation zones present below –2,100 m elevation • Less permeable at depth (see Figure 6-1) – $5 \cdot 10^{-10}$ between –2,100 and –2,300 m – $5 \cdot 10^{-11}$ between –2,300 and –5,120 m • Less saline at depth (see Figure 6-2) – Initial conditions fixed at 7.2% below –2,100 m • Bottom boundary condition of salt specified as fixed salinity of 7.2%.
Variant 3d, increased HCD transmissivity	• Steeply deeping deformation zones present below –2,100 m elevation • Less permeable at depth (see Figure 6-1) – $5 \cdot 10^{-10}$ between –2,100 and –2,300 m – $5 \cdot 10^{-11}$ between –2,300 and –5,120 m • Less saline at depth (see Figure 6-2) – Initial conditions fixed at 7.2% below –2,100 m • Lowest deformation zone transmissivity multiplied with a factor 100 (cf. Section 6.1.3). • Bottom boundary condition of salt specified as fixed salinity of 7.2%.
Variant 4	• Steeply deeping deformation zones present below –2,100 m elevation • More permeable at depth (see Figure 6-1) – $9 \cdot 10^{-10}$ between –2,100 and –2,300 m – $5 \cdot 10^{-10}$ between –2,300 and –5,120 m • Less saline at depth (see Figure 6-2) – Initial conditions fixed at 7.2% below –2,100 m • Bottom boundary condition of salt specified as fixed salinity of 7.2%.
Variant 5	• Repetition of Variant 1 and Variant 2, however • Bottom boundary condition of salt specified as no flow

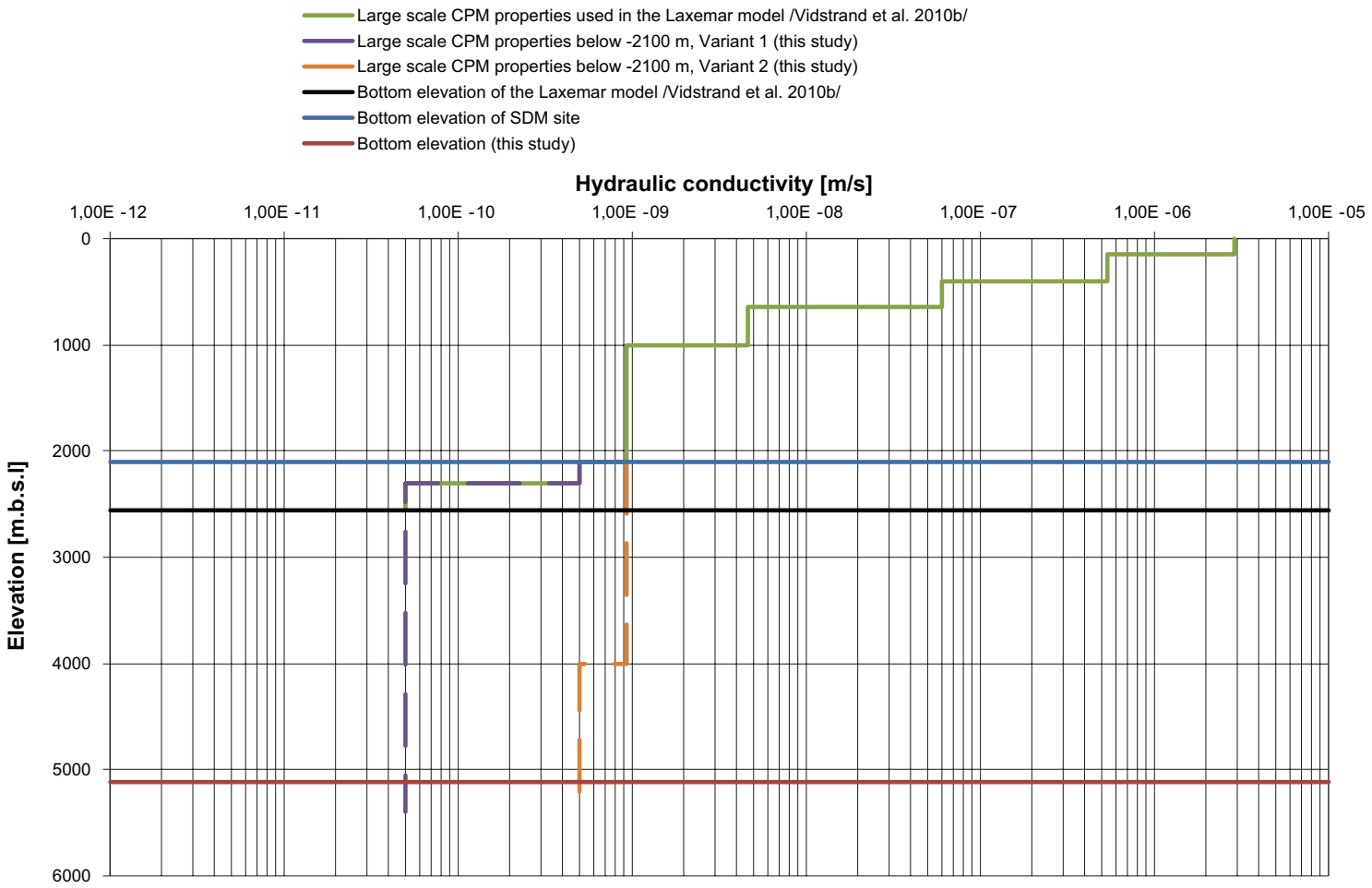

Figure 6-1. *Illustration of the two assessed depth trends for the hydraulic conductivity on the CPM parts of the model domain used herein.*

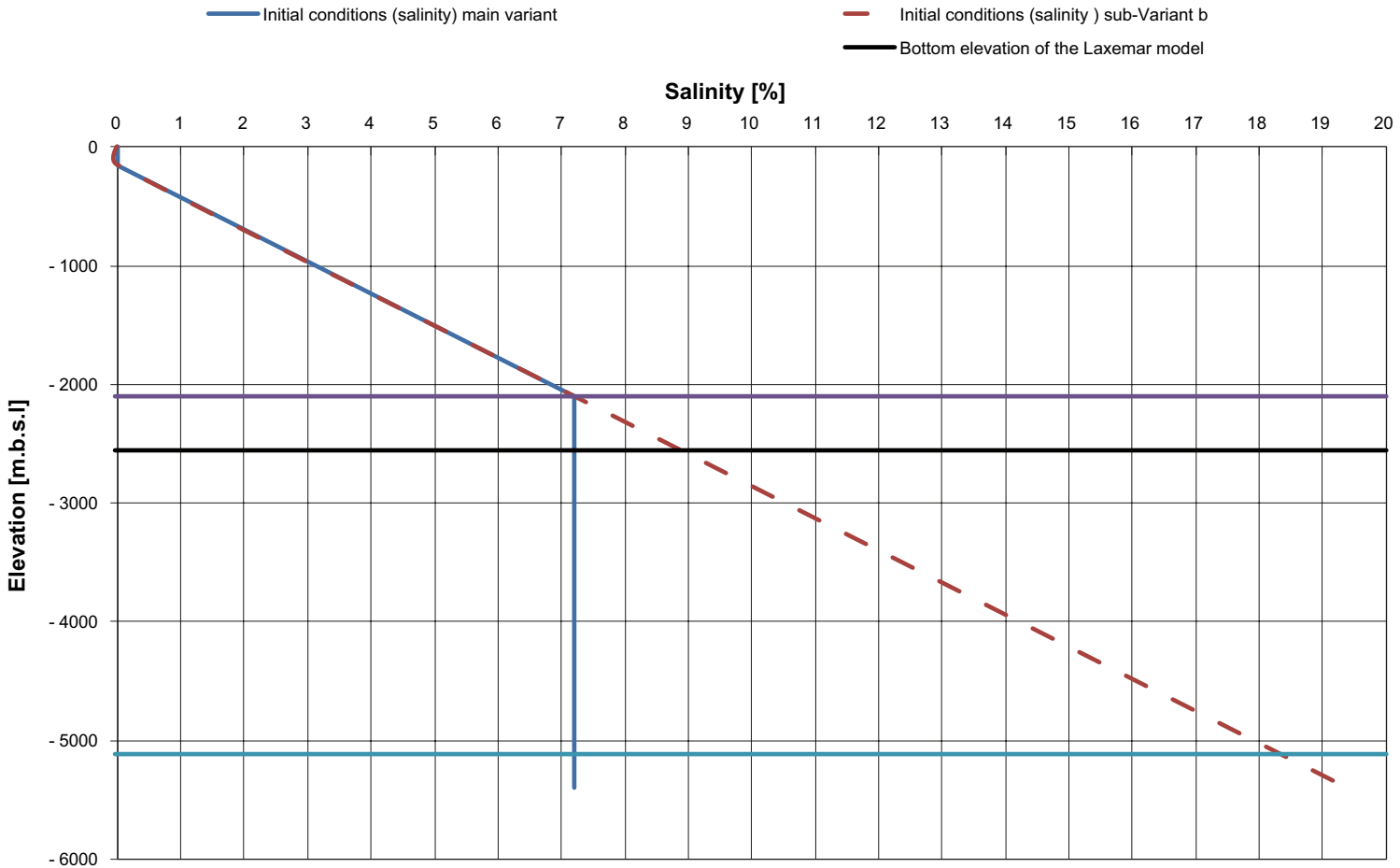

Figure 6-2. *Illustration of the two assessed initial condition depth trends of salinity in all parts of the model domain used herein.*

6.1.1 Variant 1

Variant 1 represents the Laxemar model main setting with an isotropic and homogeneous material specification (CPM) outside the SDM–Site defined volume. In the Laxemar model the hydraulic conductivity was specified to $5 \cdot 10^{-10}$ m/s at –2.1 km and this was maintained down to –2.3 km where the value was decreased one order of magnitude. This latter value, $5 \cdot 10^{-11}$ m/s, was in the Laxemar model fixed down to the bottom of the model at approximately –2.6 km. In Variant 1 of the present study, this latter value is extrapolated down to the model bottom at approximately –5.2 km.

The initial conditions of salinity is specified as in the Laxemar model /Vidstrand et al. 2010b/, i.e. fresh water down to –150 m, thereafter linearly increasing to 7.2% at –2.1 km. This value then continues all the way to the bottom of the domain.

As a sensitivity test, the depth trend of salinity is changed into a linearly increasing salinity with depth instead of the main setting of a fixed value of 7.2% below –2.1 km. This extrapolation renders a salinity of approximately 18% at –5.2 km, see Figure 6-5.

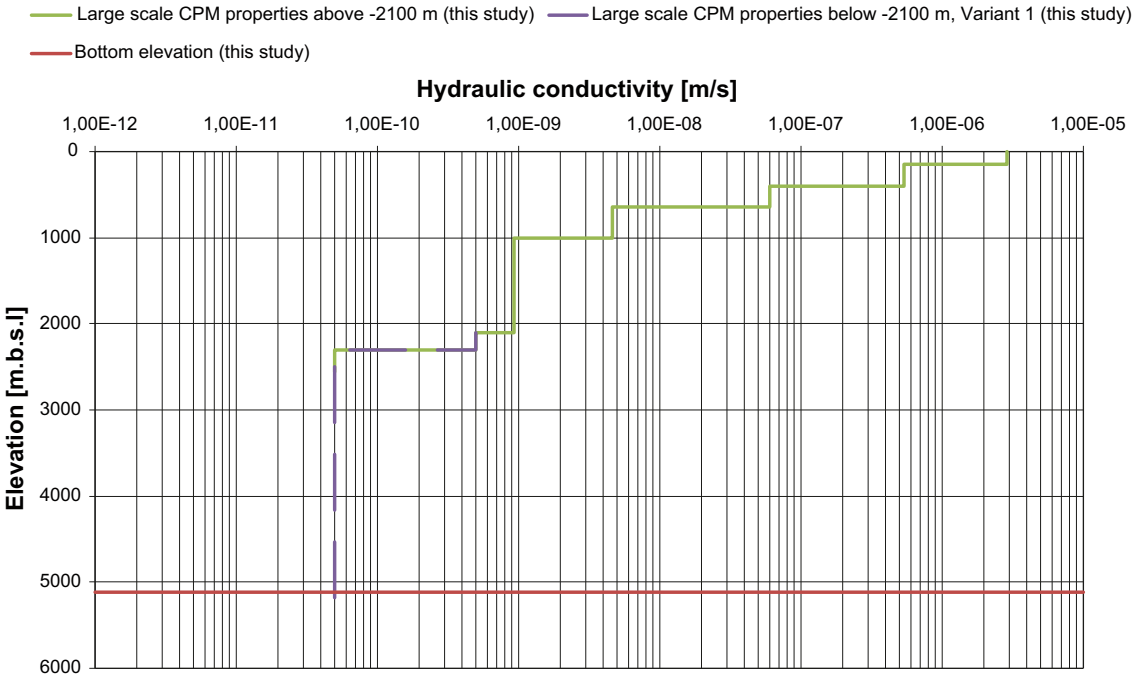

Figure 6-3. *Assessed CPM hydraulic conductivity used in Variant 1, Variant 3 and associated sensitivity tests.*

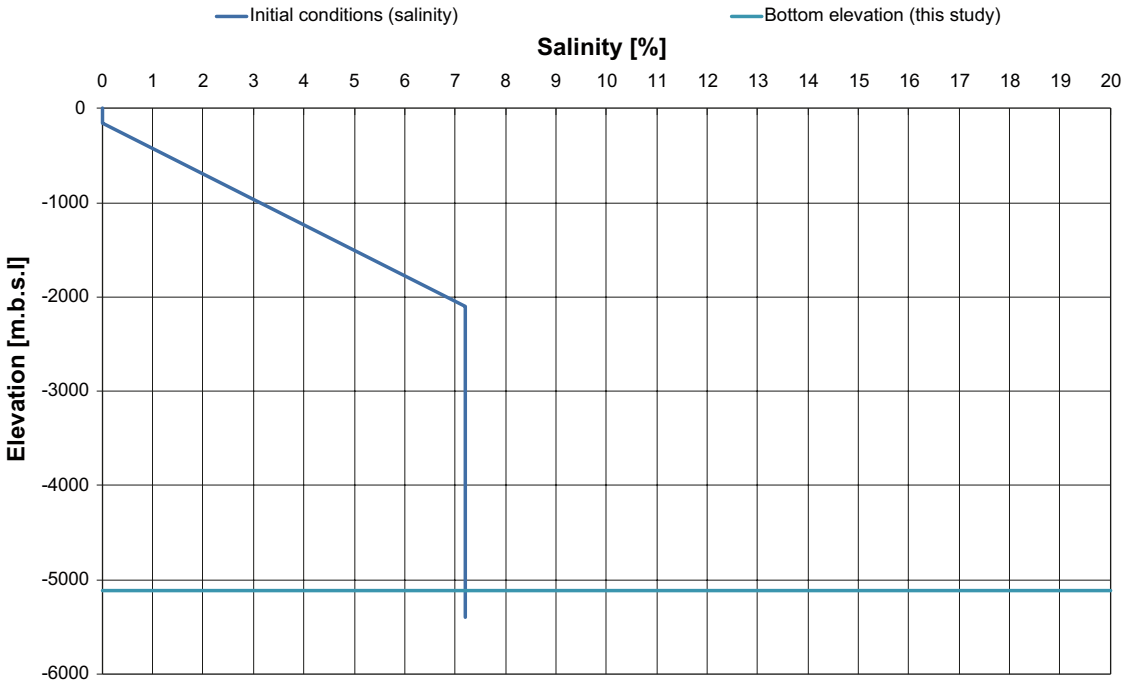

Figure 6-4. *The assessed initial condition of salinity used in Variant 1 – Variant 5.*

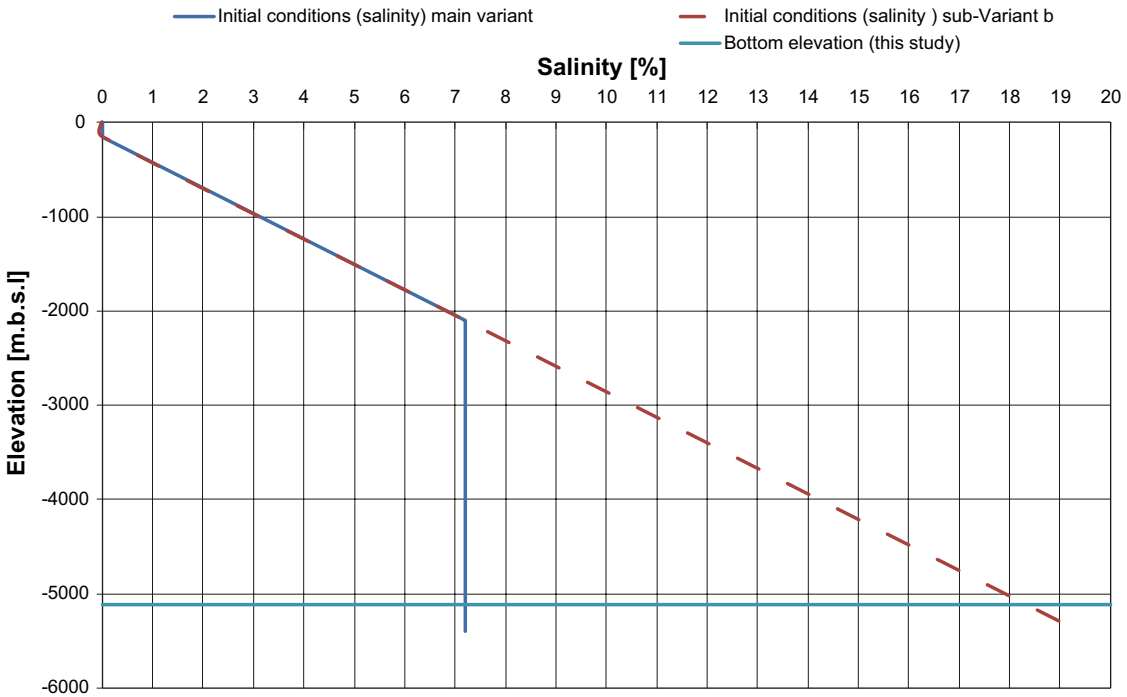

Figure 6-5. *The assessed initial condition of salinity used in Variant 1b and Variant 2b.*

6.1.2 Variant 2

Variant 2 represents a, at depth, more permeable model as compared to the Laxemar model main setting with an isotropic and homogeneous material specification below the SDM-Site defined volume. In Variant 2 of the present study, the lowest hydraulic conductivity value based on the SDM-Site defined CPM properties, $9 \cdot 10^{-10}$ m/s, is extrapolated down to approximately –4 km based on up-scaled PSS measurements and from there extrapolated depth trends (cf. Section 3.2). Below –4 km, the value is decreased to $5 \cdot 10^{-10}$ m/s. That is, the bottom of the deep model of Variant 2 is approximately one order of magnitude more permeable as compared to the Laxemar model main setting.

The salinity is treated the same as in Variant 1 and Variant 1b, respectively for Variant 2 and Variant 2b.

6.1.3 Variant 3

Variant 3 represents the Laxemar model main setting with an isotropic and homogeneous material specification below the SDM-Site defined volume. In the Laxemar model the hydraulic conductivity was specified to $5 \cdot 10^{-10}$ m/s at –2,100 m and this was maintained down to –2,300 m where the value was decreased one order of magnitude. This latter value, $5 \cdot 10^{-11}$ m/s, was in the Laxemar model fixed down to the bottom of the model at approximately –2.6 km. In Variant 3 this value is extrapolated down to the model bottom at approximately –5.2 km.

Compared to Variant 1, Variant 3 also contains an extended deformation zone model. The SDM-Site deformation zone model reached some 2.1 km deep. In the present work, the regional deformation zones of trace lengths significant for a depth of 5 km is extended (cf. Section 3.3). The extended deformation zones are uniformly given the lowest transmissivity value taken at the bottom of the SDM-Site deformation zone model. Also the thickness of the individual deformation zones is extended uniformly down to the bottom elevation at 5.2 km used in this study.

The deformation zone transmissivity below the SDM-Site model domain is specified to $1 \cdot 10^{-9}$ m^2/s and the thicknesses varies, in general, between some 10 to 50 metres.

As a sensitivity test, the lowest transmissivity value of all these regional deformation zones are increased by two orders of magnitude at all depths including an increase in the SDM-Site model domain, i.e. also at repository depth. This yields a lowest deformation zone transmissivity of $1 \cdot 10^{-7}$ m^2/s; where the deformation zone is more permeable than this value the original transmissivity value is not changed.

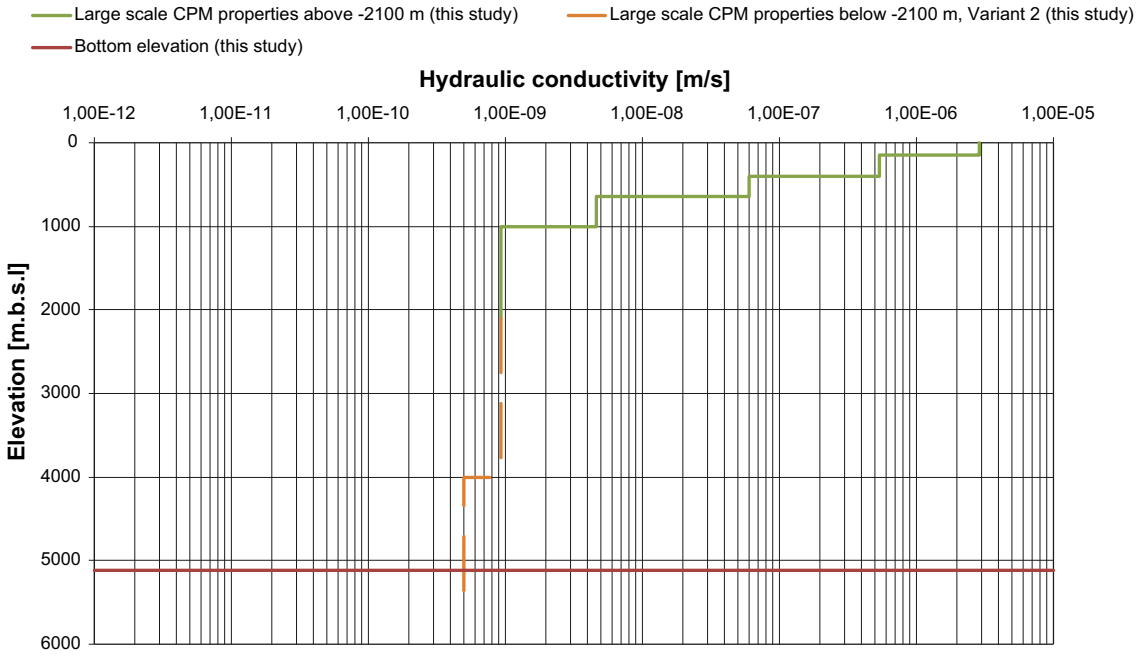

Figure 6-6. *The assessed CPM hydraulic conductivity used in Variant 2, Variant 4, Variant 5 and associated sensitivity tests.*

6.1.4 Variant 4

Variant 4 represents a, at depth, more permeable model as compared to the Laxemar main setting with an isotropic and homogeneous material specification below the SDM defined volume. In Variant 4 the lowest hydraulic conductivity value based on the SDM-Site defined CPM properties, $9 \cdot 10^{-10}$ m/s, is extrapolated down to approximately –4 km based on up-scaled PSS measurements and from there extrapolated depth trends (cf. Section 3.2). Below –4 km, the value is decreased to $5 \cdot 10^{-10}$ m/s. That is, the bottom of the deep model of Variant 4 is approximately one order of magnitude more permeable as compared to the Laxemar model main settings.

Compared to Variant 2, Variant 4 also contains an extended deformation zone model. The SDM model reached some 2.1 km. In the present study, the regional deformation zones of trace lengths significant for a depth of 5 km are extended (cf. Section 3.3). The extended deformation zones are uniformly given the lowest transmissivity value taken at the bottom of the SDM-Site deformation zone model. Also the thickness of the individual deformation zones are extended uniformly down to the now bottom elevation of 5.2 km.

The deformation zone transmissivity below the SDM-Site depth is specified to $1 \cdot 10^{-9}$ m^2/s, and the thicknesses varies, in general, between some 10 to 50 metres.

6.1.5 Variant 5

Variant 5 represents identical settings as Variant 1 and Variant 2 described above. However, compared to these variants, Variant 5 tests the influence of the specified bottom boundary condition concerning salt. In the Laxemar model /Vidstrand et al. 2010b/, the bottom boundary was fixed at a specified value (7.2%). This represents a source of salt if any salt was to be removed.

An alternative boundary condition could represent a limitation in salt from depth and be specified as a no-flow boundary, i.e. tight. This is the chosen setting for Variant 5. Simulations are conducted using the specifications of Variant 1 as well as of Variant 2.

6.2 Simulation methodology

6.2.1 Temperate case

Flow and salt transport

The governing equations for flow and salt transport are solved using fixed boundary conditions and initial conditions as applied in SDM-Site Laxemar /Rhén et al. 2009/. The initial (all variants except sub-variants b) and boundary conditions for the temperate case are shown in Table 6-3 and Table 6-4, respectively.

Output: Pressure (P), Darcy flux (q), salinity (C) at the four specified measurement localities (ML 2) at different depths.

6.2.2 Glacial cases without permafrost

Flow and salt transport

The flow and salt transport solutions derived for the temperate case are used as initial conditions together with the transient top boundary conditions shown in Table 6-5. The solutions to the governing equations for flow and salt transport are saved for different ice-front location. The time step of the simulations is 6 years. Such time step yields an ice front movement of 300 metres per time increment.

Output

See the corresponding paragraph in Section 6.2.1.

Table 6-3. Initial conditions of the fracture water and matrix porewater salinities. (inferred from /Rhén et al. 2009/) (valid for all main variants).

Depth interval	Initial salinity
Ground surface to –150 m	0%
–150 m to –2,100 m	Linearly increasing to 7.2%
Below –2,100 m	7.2%

Table 6-4. Boundary conditions for the temperate case (valid for all variants except sub-variants b).

Boundary	Boundary conditions
Shoreline elevation	0 m RHB 70
Top boundary, land above sea	P=0 at ground surface; C=0
Top boundary, land below sea	P=g ρ_0 (sea depth); C=0%
Lateral (vertical) boundaries	$\partial P/\partial x=\partial P/\partial y=0$ and $\partial C/\partial x=\partial C/\partial y=0$
Bottom boundary at –5,056 m	$\partial P/\partial z=0$; C=7.2% by weight

Table 6-5. Boundary conditions for the glacial cases without permafrost (valid for all variants except sub-variants b).

Boundary	Boundary conditions
Shoreline elevation	0 m RHB 70
Top boundary, land without ice	P=0 at ground surface; C=0
Top boundary, land below sea	Hydrostatic pressure: P=g ρ_0 (sea depth); C=0%
Top boundary, land below ice	P according to Equation 4-3; C=0%
Lateral (vertical) boundaries	$\partial P/\partial x=\partial P/\partial y=0$ and $\partial C/\partial x=\partial C/\partial y=0$
Bottom boundary at –5,056 m	$\partial P/\partial z=0$; C=7.2% by weight

6.3 Model domain, measurement localities and ice-front locations

A NW-SE orientation of the model domain is assumed to be the most appropriate orientation to study for an advancing ice sheet margin. Figure 6-7 shows the location of the NW-SE model domain studied in all variants.

The NW-SE model domain is approximately 36 km long, 20 km wide and 5.2 km deep. Hence, a super-regional modelling approach is used. Examples of previous studies for SKB focusing on hydro-geological issues on a super-regional scale are, among others, /Follin and Svensson 2003, Holmén et al. 2003, Holmén 2008, Ericsson et al. 2006, Ericsson and Holmén 2010, Vidstrand et al. 2010a, b/.

The coordinates of the four measurement locations (ML 2, depth) are shown in Table 6-6.

The Roman numeral shown in Figure 6-7 indicates the position of the studied ice-front location (herein only IFL II is shown) for the NW-SE model domain.

Table 6-6. Coordinates of the measurement localities ML 2, depth.

Measurement locality	Coordinate (x,y,z) (DarcyTools local)	Coordinate (x,y,z) (RT 90, RHB 70)
2, –500	(9250,6000, –500)	(1548250,6366000, –500)
2, –2,500	(9250,6000, –2,500)	(1548250,6366000, –2,500)
2, –3,000	(9250,6000, –3,000)	(1548250,6366000, –3,000)
2, –3,500	(9250,6000, –3,500)	(1548250,6366000, –3,500)

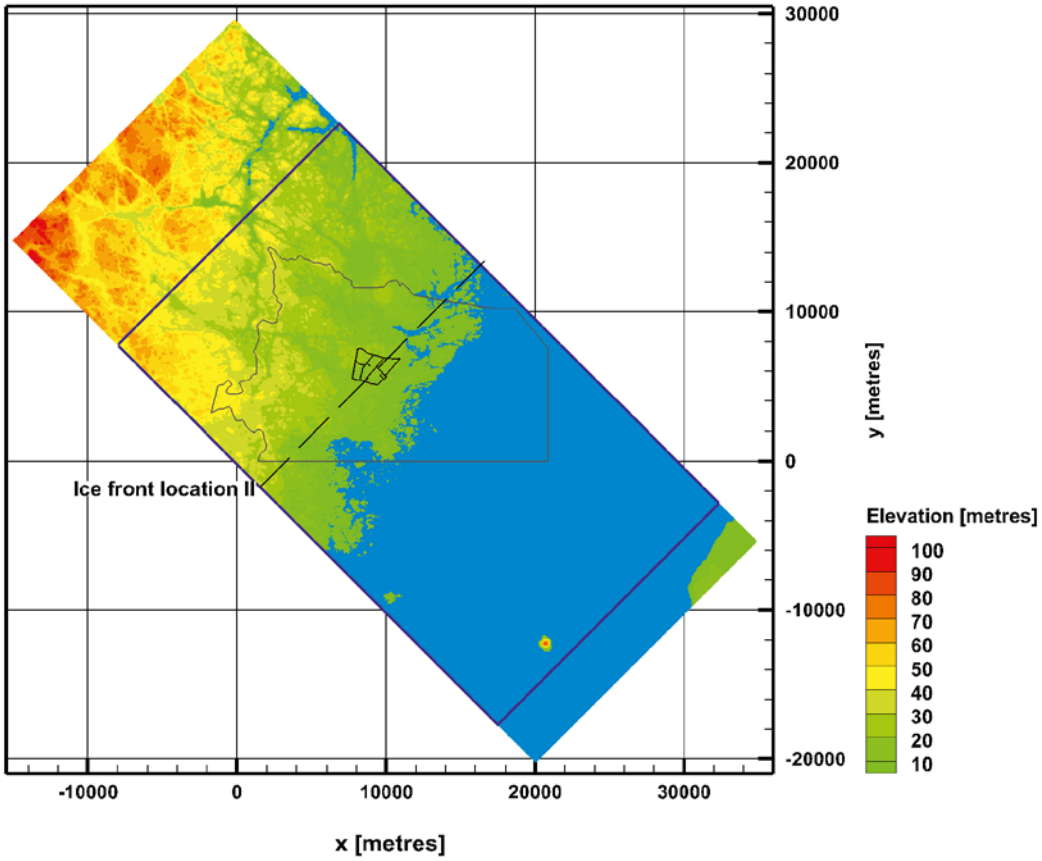

Figure 6-7. *Location of the Laxemar model domain assessed in /Vidstrand et al. 2010b/. The larger purple/black rectangle illustrates the model boundaries used in this study. The map shows the present-day topography at Laxemar-Simpevarp and the position of the studied ice-front location (IFL II). The large polygon in the centre is the regional flow domain used in the groundwater flow modelling for SDM-Site Laxemar /Rhén et al. 2009/. The location of the hypothetical final repository for spent nuclear fuel is also shown. The y-axis points towards north.*

6.4 Hydraulic properties

The geometry and hydraulic properties of discrete geological features in the bedrock such as deformation zones are the same as in SDM-Site. The data used here are imported from /Joyce et al. 2010/ and visualised in Figure 6-8. Figure 6-9 illustrates the difference in depth between the SDM site deformation zone model and the extended deformation zone model used in this study for Variant 3 and Variant 4.

Concerning the stochastic hydrogeological properties of the fracture domains within the focused area, a single realisation is studied in the work reported here.

The parameters and the parameter values used to generate a hydrogeological realisation of the fracture domains within the focused area are listed in Appendix A, which also presents the hydraulic properties used for the bedrock outside the fracture domains and the deformation zones modelled deterministically in SDM-Site.

The grid cell hydraulic properties of the uppermost 20 m of the model domain and the minimum values of the hydraulic properties below 20 m depth are shown in Table 6-7 and Figure 6-10.

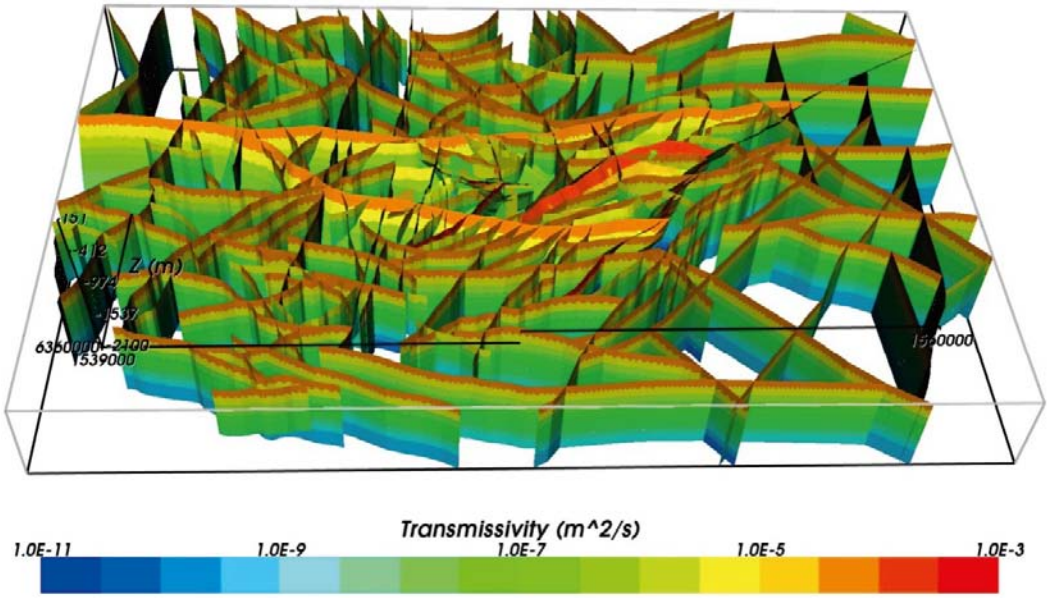

Figure 6-8. *Visualisation of regional and local scale deformation zones (HCD). Each zone is coloured by its hydraulic conductivity (cf. Figure 2-8). Oblique view looking from the south. /Rhén and Hartley 2009/.*

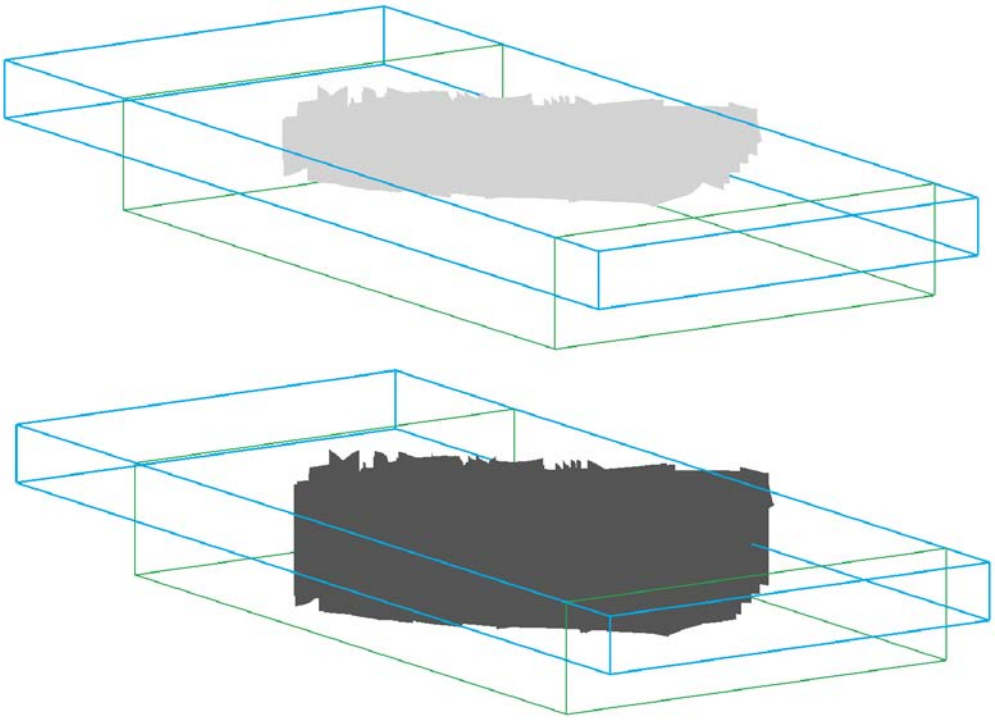

Figure 6-9. *Illustration of the difference in depth of the SDM site deformation zone model and the extended model used in Variant 3 and Variant 4.*

Table 6-7. Grid cell hydraulic properties applied in this work in the uppermost 20 m of the model domain and the minimum values allowed below this depth. (After /Vidstrand et al. 2010b/.)

Grid cell property	Depth interval	Value
Hydraulic conductivity K_c [m/s]	< 20 m depth	$K_{c,h} = \max \begin{cases} 1 \cdot 10^{-7} \\ 5 \cdot 10^{-3}\, 10^{-Depth/3} \end{cases}$ $K_{c,v} = 1 \cdot 10^{-6}$
	> 20 m depth	$K_{c,h} \geq 3 \cdot 10^{-11}$ $K_{c,h} \leq 3 \cdot 10^{-11}$
Kinematic porosity ϕ_c [–]	< 20 m depth	$\phi_c = \max \begin{cases} 1 \cdot 10^{-3} \\ 5 \cdot 10^{-2}\, 10^{-Depth/20} \end{cases}$
	> 20 m depth	$\phi_c \geq 1 \cdot 10^{-5}$
Specific storage $S_{s,c}$ [m^{-1}]	> 0 m depth	$S_{s,c} = 1 \cdot 10^{-9}$

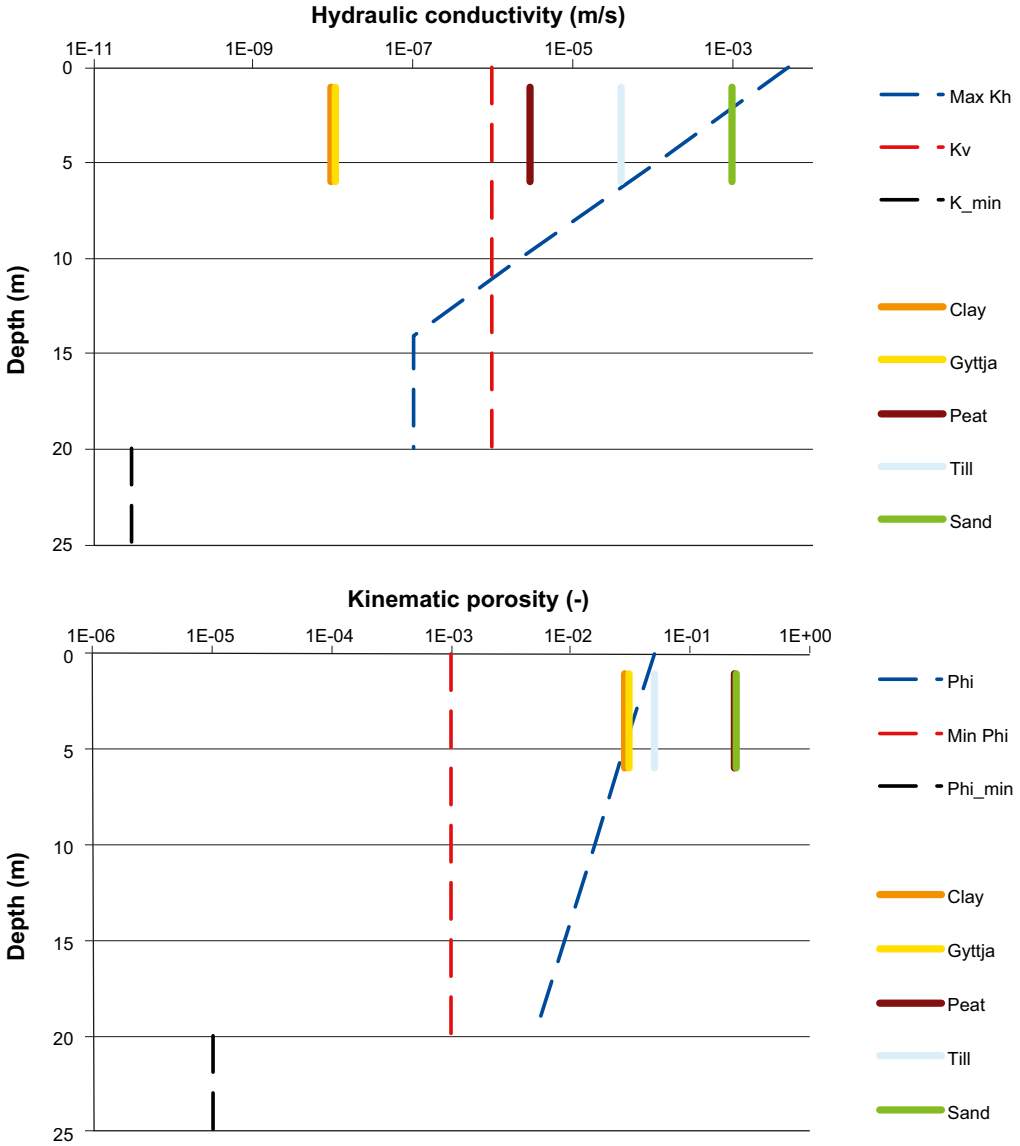

Figure 6-10. *The blue and red dashed lines show the values used in this work to simulate the hydraulic properties of the Quaternary deposits and the uppermost bedrock, i.e. above 20 m depth and shown along with the measured SDM-Site values for different rheological units. The black dashed line represents the minimum values of hydraulic properties assigned to numerical cells of parts with no fractures of the bedrock below this depth (cf. Table 6-7).*

6.5 Computational grid

The model domain is discretised by an unstructured grid. Close to ground surface, a 50 m digital elevation model is refined (interpolated) to fit a grid cell size of 32 m in the horizontal directions. The resolution of the topographic variations in the vertical direction is set to 2 m. The bottom of the model domain is located at an elevation of –5,120 m. The thickness of the bottom cell layer is constant throughout the model domain and set to128 m. (The elevation of the pressure node in bottom cell layer is located at –5,056 [= –5,120 m+(128 m/2)].)

Within the area specified in Table 6-8, the cell size is $(32\ m)^3$ (cf. the area shown in Figure 6-11). Far away from this area, the largest cell size is $(512\ m)^3$. In between, a varying cell size is used. In total, the model domain consists of 6.1 million cells.

Table 6-8. Corner coordinates of the area shown in Figure 6-11.

Corner	Coordinate (x,y) (DarcyTools local)	Coordinate (x,y) (RT90)
NW	(7000,8000)	(1546000,6368000)
NE	(11500,8000)	(1550500,6368000)
SW	(7000,4500)	(1546000,6364500)
SE	(11500,4500)	(1550500,6364500)

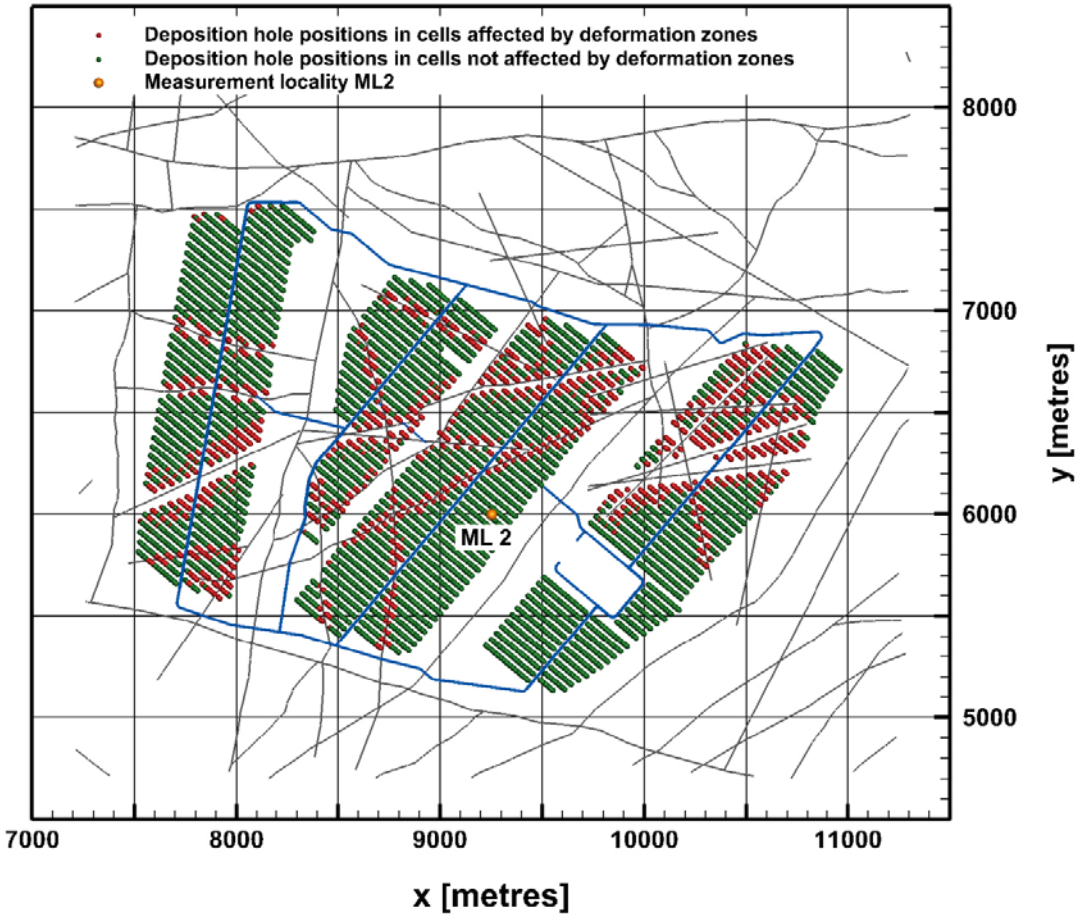

Figure 6-11. *Plane view of the studied repository layout at –500 m elevation. The thin lines represents deformation zones. The dot labelled ML 2 represents the measurement locality ML2, –500 m. The three other measurement localities are located straight beneath ML 2 but on elevation –2,500 m, –3,000 m and –3,500 m respectively. The hydraulic properties in the model at these localities are presented in Section 6.6. The y-axis points towards north. Observe that the repository is not explicitly modeled in this study.*

6.6 Permeability at the four measurement localities

Measurement locality ML 2, –500 m is located in the centre of the repository area. Figure 6-12 shows a close-up view around measurement locality ML 2. The hydraulic properties of the grid cells containing red dots are affected by the hydraulic properties of the deformation zones nearby as a result of the chosen discretisation.

Figure 6-13 shows the position of the measurement locality (ML 2) and the permeability field at repository depth.

- ML 2, –500 m is placed in the centre of the target volume and is not affected by any deformation zone. The maximum hydraulic conductivity of the grid cell hosting ML 2 is $2.5 \cdot 10^{-8}$ m/s.
- ML 2, –2,500 m is placed in an isotropic and homogeneous surrounding with properties of either $5 \cdot 10^{-11}$ m/s or $9 \cdot 10^{-10}$ m/s depending on variant tested.
- ML 2, –3,000 m is placed in an isotropic and homogeneous surrounding with properties of either $5 \cdot 10^{-11}$ m/s or $9 \cdot 10^{-10}$ m/s depending on variant tested.
- ML 2, –3,500 m is placed in an isotropic and homogeneous surrounding with properties of either $5 \cdot 10^{-11}$ m/s or $9 \cdot 10^{-10}$ m/s depending on variant tested.

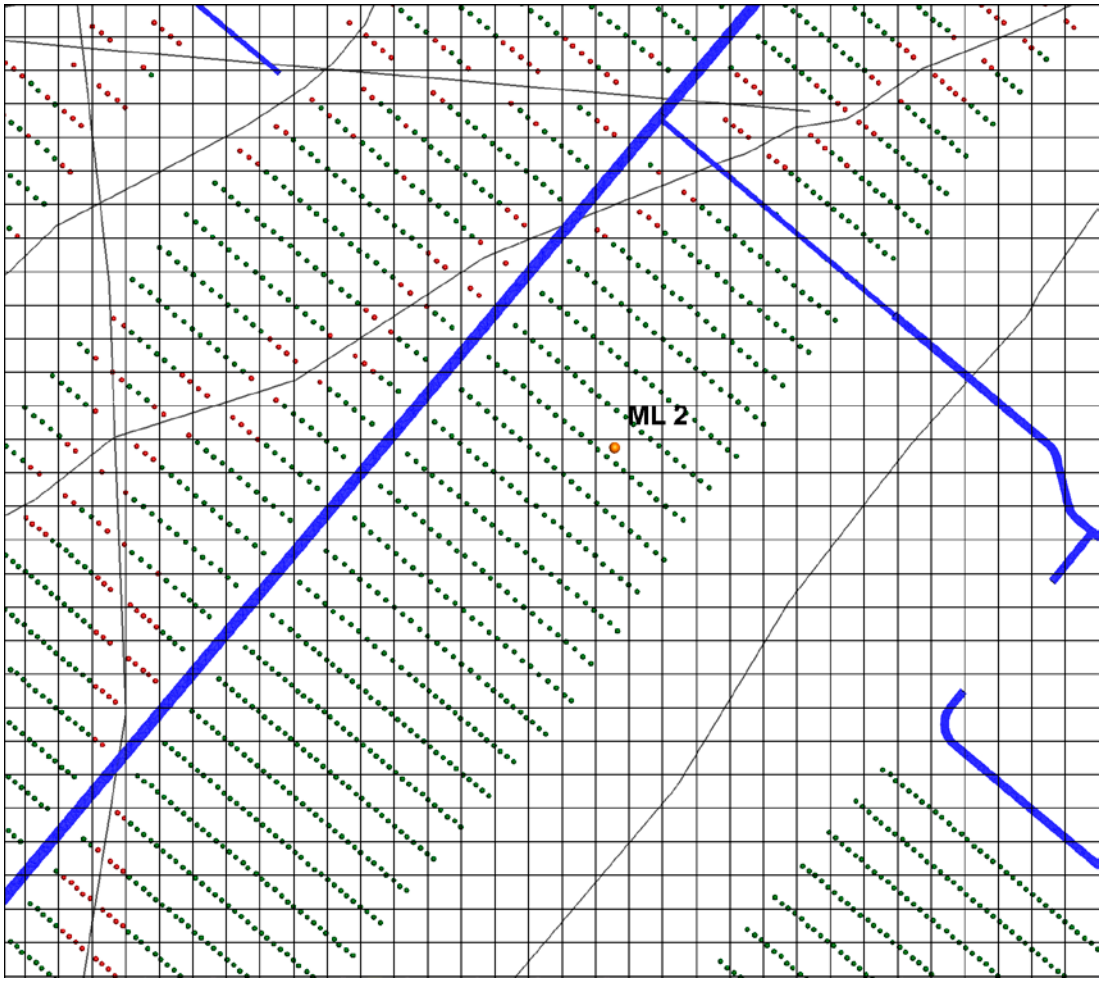

Figure 6-12. *Horizontal view of the computational grid around measurement locality number 2. The resolution of the computational grid adjacent to the repository is 32 m. The transport tunnels are shown as blue lines and the deposition hole positions as dots. The dots are coloured red or green depending on if they are positioned within grid cells that also contain one or several intercepts with the deterministically modelled deformation zones (red dot) or not (green dot). That is, the hydraulic properties of the cells with red dots are affected by the hydraulic properties of the deformation zones as a result of the chosen discretisation. The deformation zones are here visualised as trace lines (scan lines without geological thickness).*

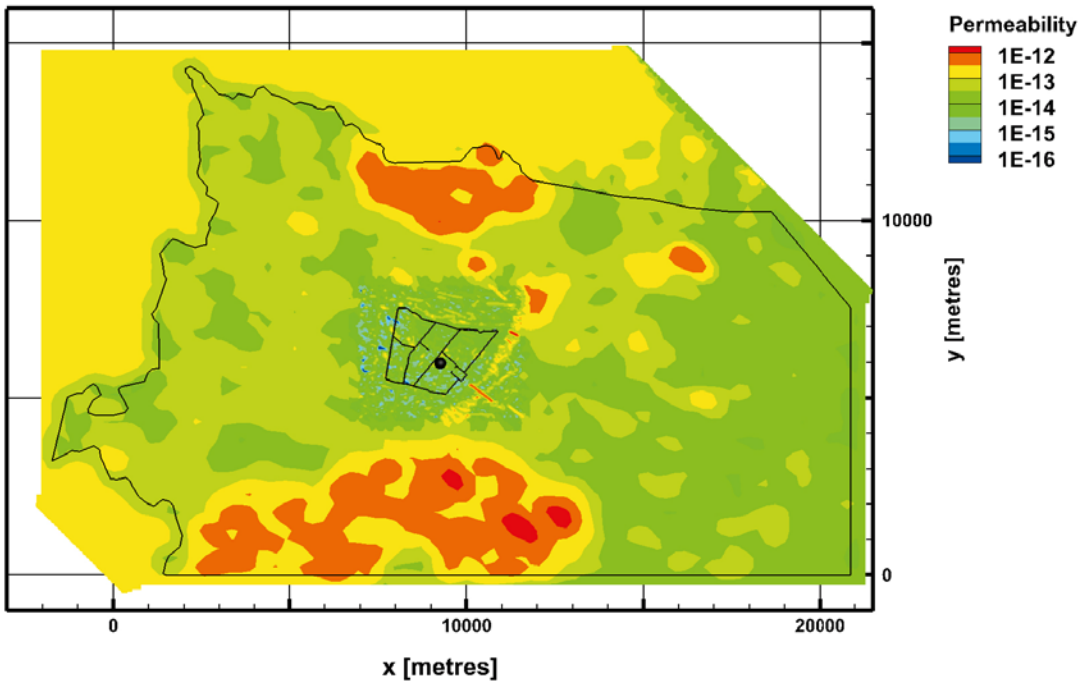

Figure 6-13. *Horizontal view showing the measurement locality (ML 2) and the permeability field at repository depth (elevation –500 m). The three other measurement localities are located straight beneath ML 2 but on elevation –2,500 m, –3,000 m and –3,500 m, respectively. The large polygon shows the regional flow domain used in SDM-Site /Rhén et al. 2009/. The y-axis points towards north.*

7 Results

7.1 Darcy flux during the ice front passage

The Darcy flux at the four measurement localities are monitored with an increment of 6 years, i.e. the ice front moves in a forward manner with about 300 metres per time increment.

Results from three of the tested variants are described in the subsequent Sections 7.2.1 to 7.2.3 below. The reported results are focussed on the variants including significant changes in the hydraulic conductivity of the model.

7.1.1 Variant 1

The development of the Darcy flux during the ice front passage for the four different depth locations along the ML2 location line is illustrated in Figure 7-1.

The increase in Darcy flux is almost two orders of magnitude regardless of the initial value and depth location. For the deeper locations, however, the increase is distributed over a longer time and the peak is less pronounced.

7.1.2 Variant 2

The development of the Darcy flux during the ice front passage for three different depth locations along the ML2 location line is illustrated in Figure 7-2. Compared to Variant 1 which is less permeable at depth, Variant 2 yields higher fluxes.

The increase in Darcy flux is almost two orders of magnitude regardless of the initial value and depth location. For the deeper locations, however, the increase is distributed over a longer time and the peak is less pronounced.

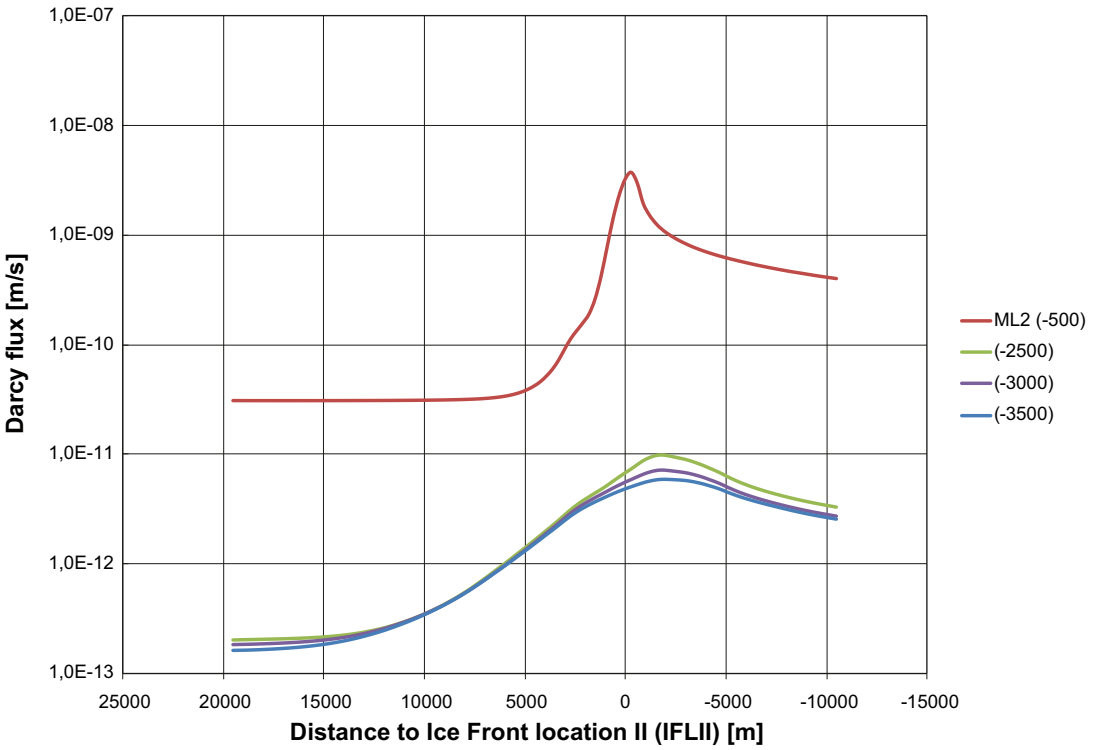

Figure 7-1. *Development of Darcy flux along the ice front passage for four different depth locations along the ML2 locality line. The results are for Variant 1. Positions to the right of 0 are covered by the ice sheet.*

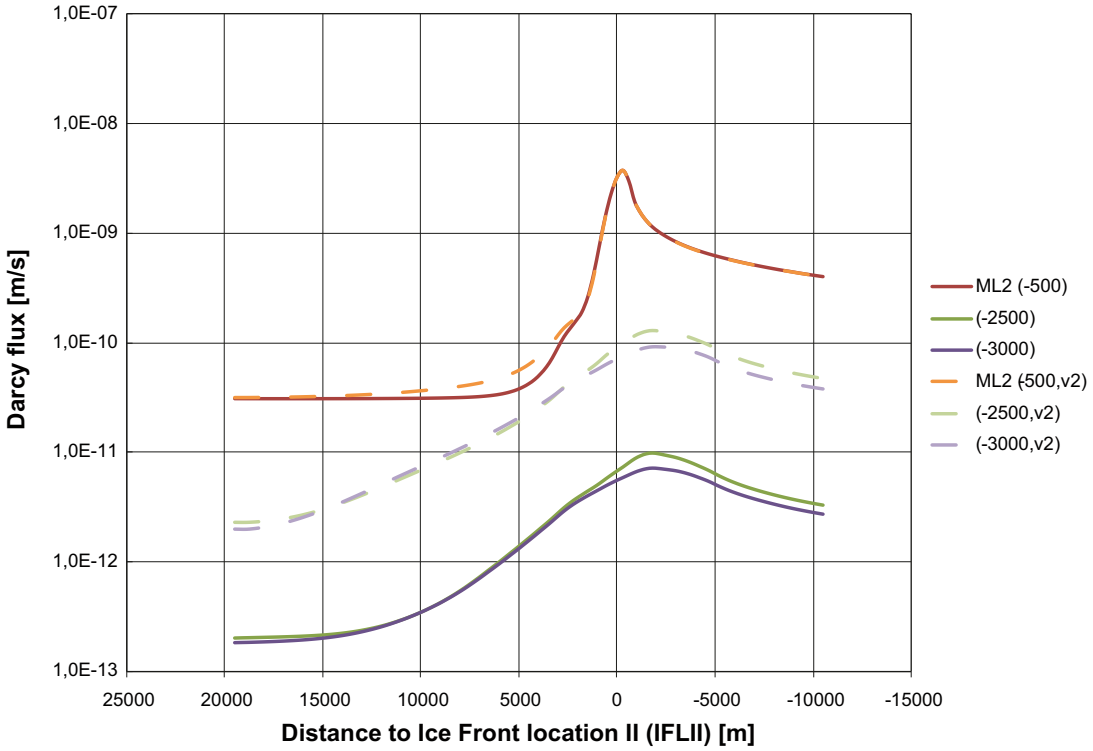

Figure 7-2. *Development of Darcy flux along the ice front passage for three different depth locations along the ML2 locality line. The results are for Variant 1 along with Variant 2. Positions to the right of 0 are covered by the ice sheet.*

7.1.3 Variant 3d, Increased deformation zone transmissivity by a factor of 100

The development of the Darcy flux during the ice front passage for three different depth locations along the ML2 location line is illustrated in Figure 7-3. Compared to Variant 1, Variant 3d – with a more permeable deformation zone model – yields higher Darcy fluxes at depth primarily as a result of the slightly more permeable deeper part of the model.

The increase in Darcy flux is almost two orders of magnitude regardless of the initial value and depth location. For the deeper locations, however, the increase is distributed over a longer time and the peak is less pronounced.

7.2 Salinity during the ice front passage

The salinity at the four measurement localities is monitored transiently with increments of 6 years, i.e. the ice front moves in a forward manner with about 300 metres per time increment. Results from all nine tested variants are described in the subsequent Sections 7.1.1 to 7.1.9, below.

7.2.1 Variant 1

The change in salinity during the ice front passage at four different depth locations along the ML2 location line is illustrated in Figure 7-4.

The salinity development at repository depth is described in more detail in /Vidstrand et al. 2010b/. The repository depth is initially fresh but experiences a sudden increase in salinity during the ice front passage with peak values around 2% by weight. The –2.5 kilometres deep location is found to experience a weak, however observable, increase during the ice front passage. This slow increase continues for a while longer than for the peak behaviour found at repository depth. After the ice front passage, this depth responds with a slowly decreasing salinity.

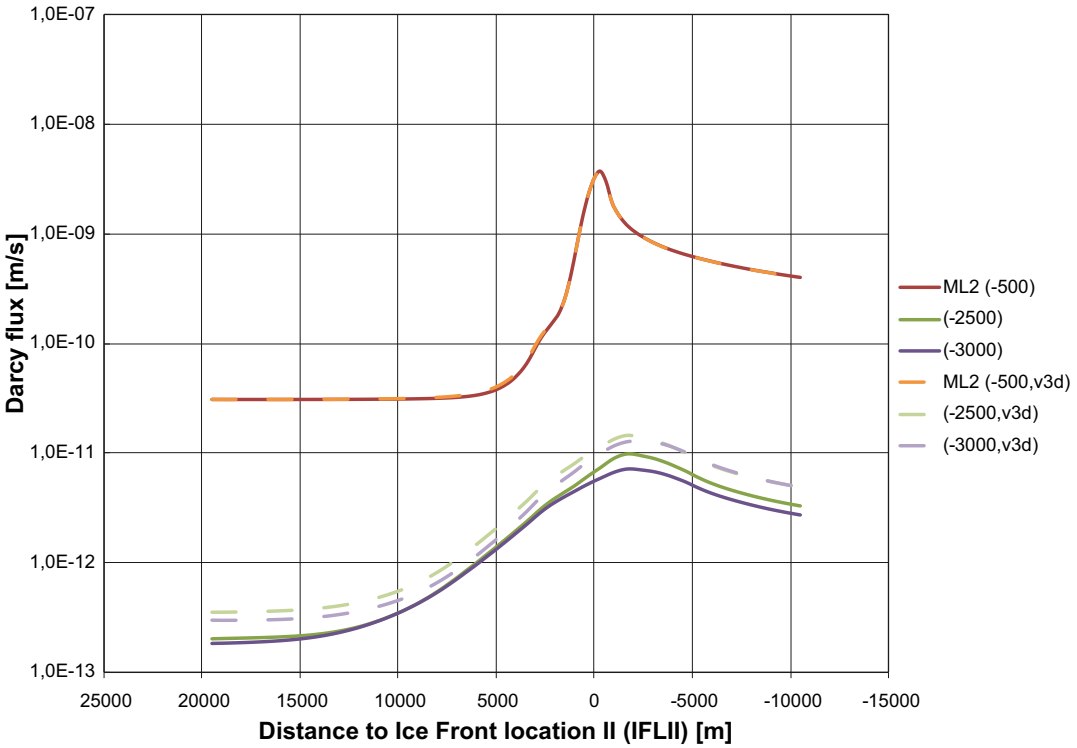

Figure 7-3. *Development of Darcy flux along the ice front passage for three different depth locations along the ML2 locality line. The results are for Variant 1 along with Variant 3d. Positions to the right of 0 are covered by the ice sheet.*

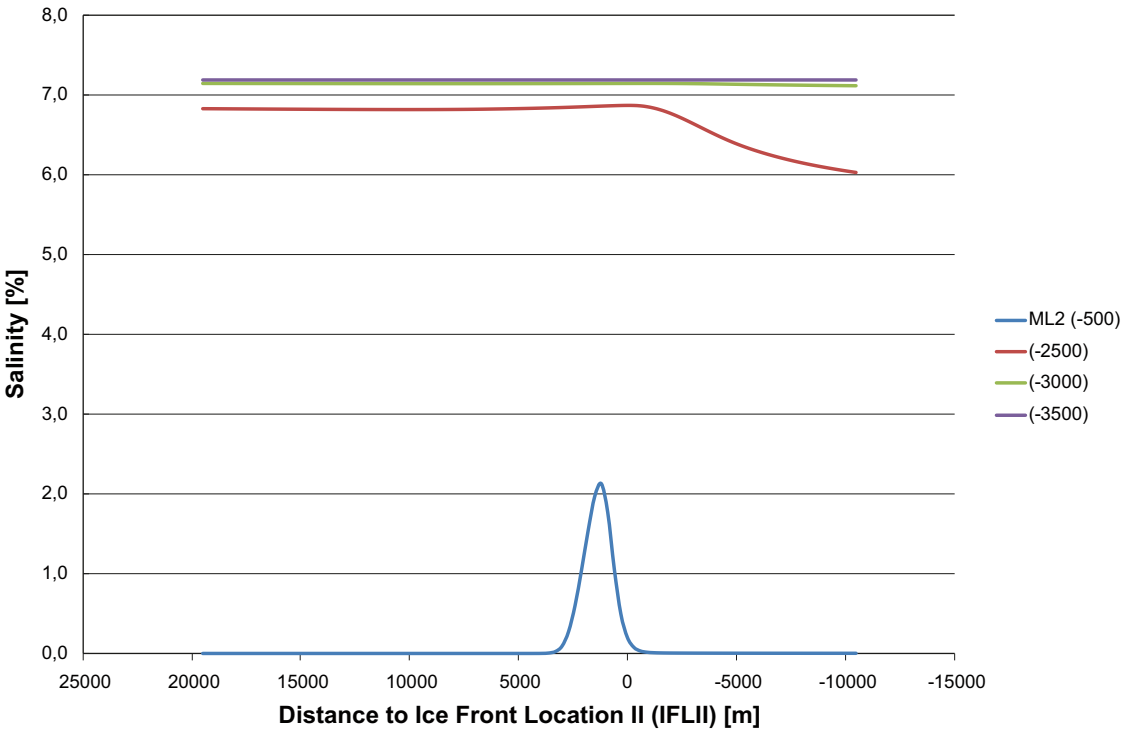

Figure 7-4. *Development of salinity along the ice front passage for four different depth locations along the ML2 locality line. The results are for Variant 1. Positions to the right of 0 are covered by the ice sheet.*

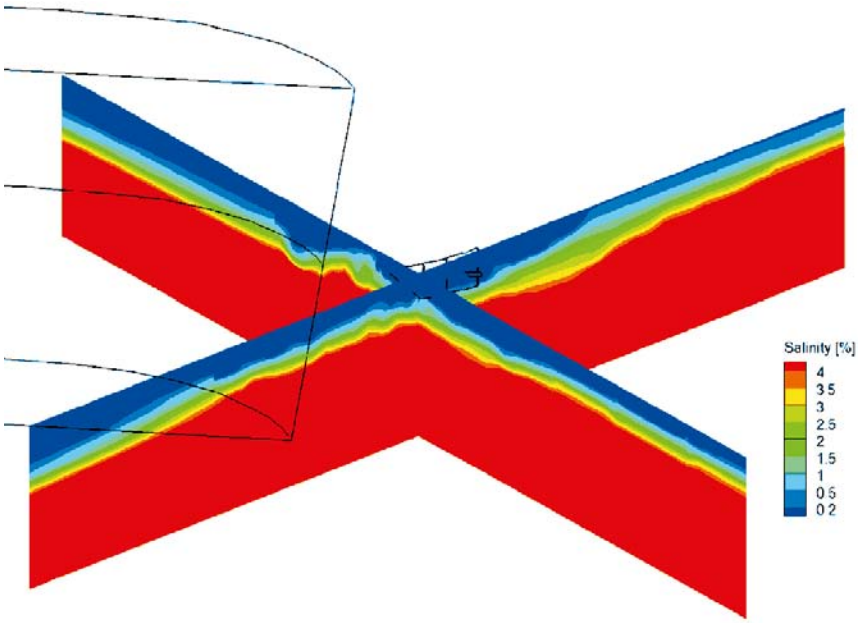

Figure 7-5. *A snap-shot illustration of the salinity field along two cross-sections for a situation where the ice front is found approximately 2 kilometres northwest (upstream) of the repository location. The repository design is presented in the figure along with a sketch of the ice sheet indicating front location and ice shape, with a strong ice surface gradient close to the front and an almost flat ice surface further away from the ice front. The results are for Variant 1.*

For the two deepest locations, –3,000 m and –3,500 m, no distinct increase during the passage can be observed. However, both locations experience a minor but observable decrease after the passage. For all the deep locations the salinity is still high after the ice front passage.

7.2.2 Variant 1b

The change in salinity during the ice front passage at four different depth locations along the ML2 location line is illustrated in Figure 7-6. For comparison, the corresponding results of Variant 1 described above are also included.

Compared to Variant 1, Variant 1b, which has an increased salinity with depth, experiences a slightly higher increase in salinity during the upconing event. All depth locations show a minor increase during the upconing; during the subsequent flushing, the decrease is significant for the measurement locality at –2,500 m.

For the two deepest locations, –3,000 m and –3,500 m, no distinct decrease after the passage can be observed.

For all deep locations the salinity is still high after the ice front passage.

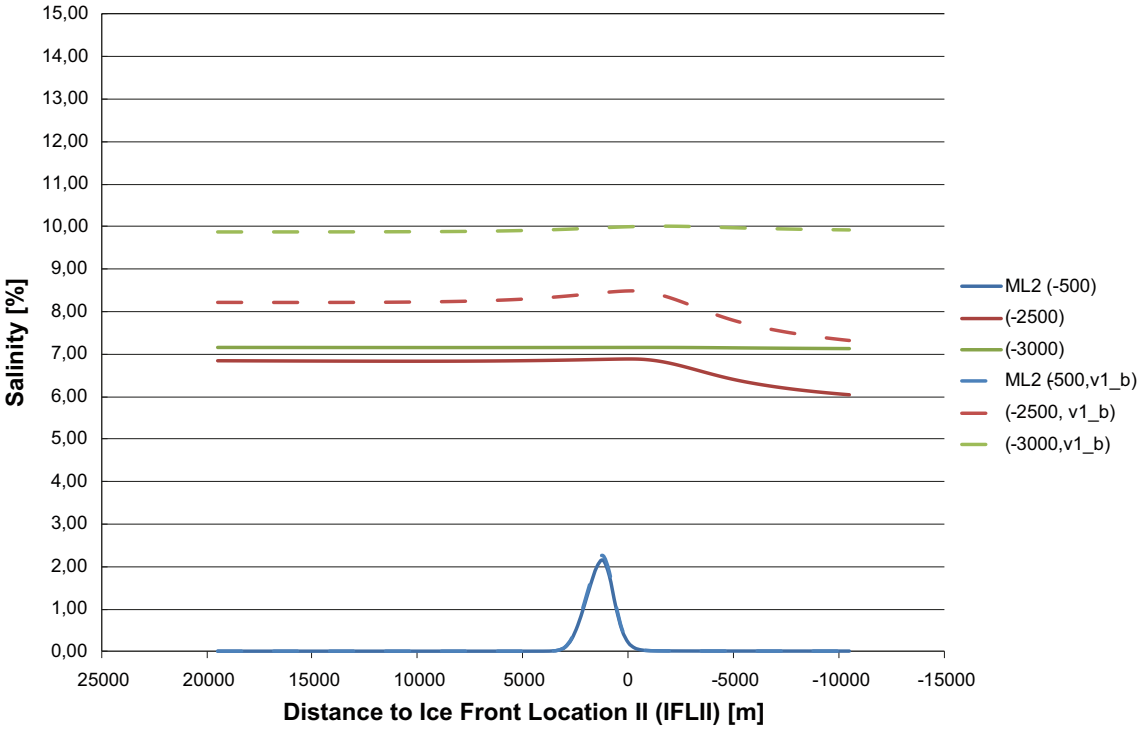

Figure 7-6. *Development of salinity along the ice front passage for four different depth locations along the ML2 locality line. Variant 1 along with Variant 1b (dashed). Positions to the right of 0 are covered by the ice sheet.*

7.2.3 Variant 2

Variant 2 represents a case with higher hydraulic conductivity at depth. The change in salinity during the ice front passage at four different depth locations along the ML2 location line is illustrated in Figure 7-7.

Repository depth is initially characterised by fresh water, but experiences a sudden increase during the ice front passage with peak values around 4% by weight. It is noteworthy that the change in permeability is made only in the deep sections of the model, i.e. below –2,100 m. However, this results in a change in salinity at repository depth during the ice front passage. For this particular property setting, the peak values during the ice front passage are about two times larger than the results reported in /Vidstrand et al. 2010b/. The results reported here are associated with a significant uncertainty since the knowledge of the properties at depth is limited. However, it should be stated that the extrapolated properties used in Variant 2 are based on hydraulic information from deformation zones. On larger scale properties from the bedrock in-between deformation zones should have a significant influence. It is hence plausible that the properties used in Variant 1 are the most probable and even that the properties may be even less permeable at depth than indicated in Variant 1.

The 2.5 kilometres deep location is found to experience a small, however observable, increase during the ice front passage. This slow increase continues for a while longer than for the peak behaviour found at repository depth. After the passage, a significant decrease in salinity is observed.

For the two deepest locations, –3,000 m and –3,500 m, no distinct increase during the passage can be observed. However, both locations experience a small, and for the –3,000 m location significant, decrease after the passage. However, for all the deep locations the salinity is still high after the ice front passage.

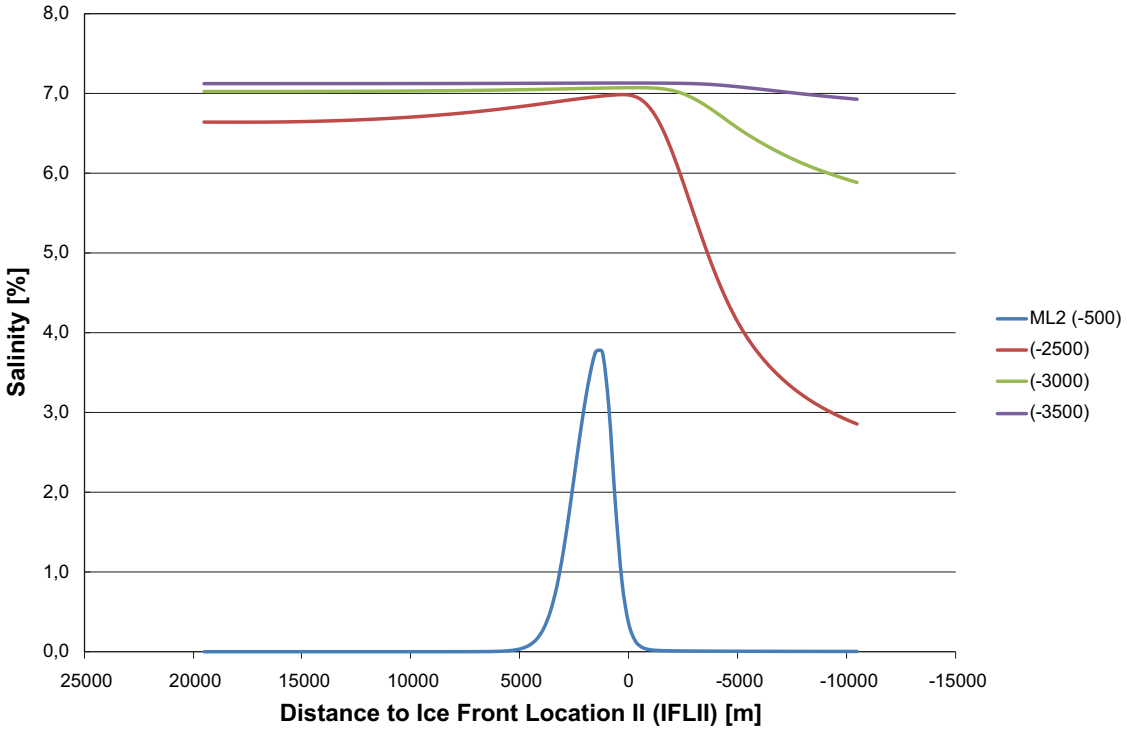

Figure 7-7. *Development of salinity along the ice front passage for four different depth locations along the ML2 locality line. The results are for Variant 2. Positions to the right of 0 are covered by the ice sheet.*

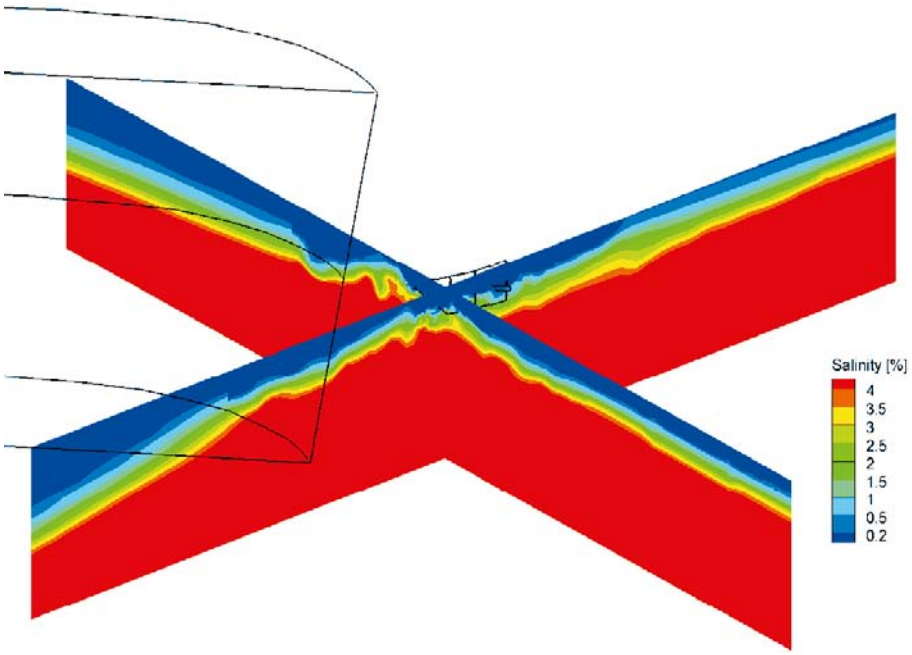

Figure 7-8. *A snap-shot illustration of the salinity field along two cross-sections for a situation where the ice front is found approximately 2 kilometres northwest (upstream) of the repository location. The repository design is presented in the figure along with a sketch of the ice sheet indicating front location and ice shape. The results are for Variant 2.*

7.2.4 Variant 2b

The change in salinity during the ice front passage at four different depth locations along the ML2 location line is illustrated in Figure 7-9. For comparison, the results of Variant 2, described above, are also shown.

Compared to Variant 2, Variant 2b which has an increased salinity with depth, experiences a higher salinity increase during the upconing event. All depth locations show an increase during the upconing. During the subsequent flushing, the decrease is significant for the measurement localities at –2,500 m and –3,000 m.

For all the deep locations the salinity is still high after the ice front passage.

7.2.5 Variant 2c, Increased cell porosity by a factor 5

The change in salinity during the ice front passage at four different depth locations along the ML2 location line is illustrated in Figure 7-10. For comparison, the results of Variant 2, described above, are also shown.

Compared to Variant 2, Variant 2c with increased cell porosity experiences a slightly smaller salinity increase during the upconing event. Repository depth is initially characterised by fresh water, but experiences a sudden increase during the ice front passage with peak values around 3% by weight. The –2.5 kilometres deep location is found to experience a weak, however, observable increase during the ice front passage. This slow increase continues for a longer period of time than the peak behaviour found at repository depth. After the passage, salinity decreases slowly at this depth.

For the depth location at –3,000 m, no distinct increase during the passage can be observed. However, a minor but observable decrease is observed after the passage.

For all the deep locations the salinity is still high after the ice front passage.

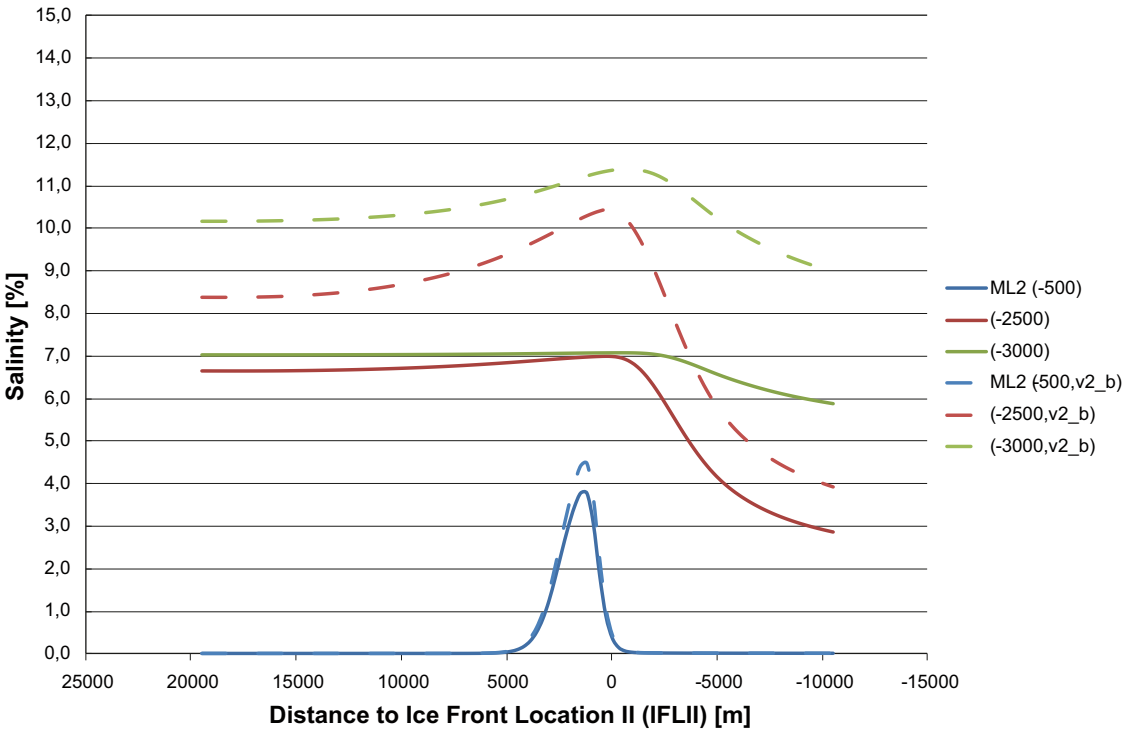

Figure 7-9. *Development of salinity along the ice front passage for four different depth locations along the ML2 locality line. Variant 2 along with Variant 2b (dashed). Positions to the right of 0 are covered by the ice sheet.*

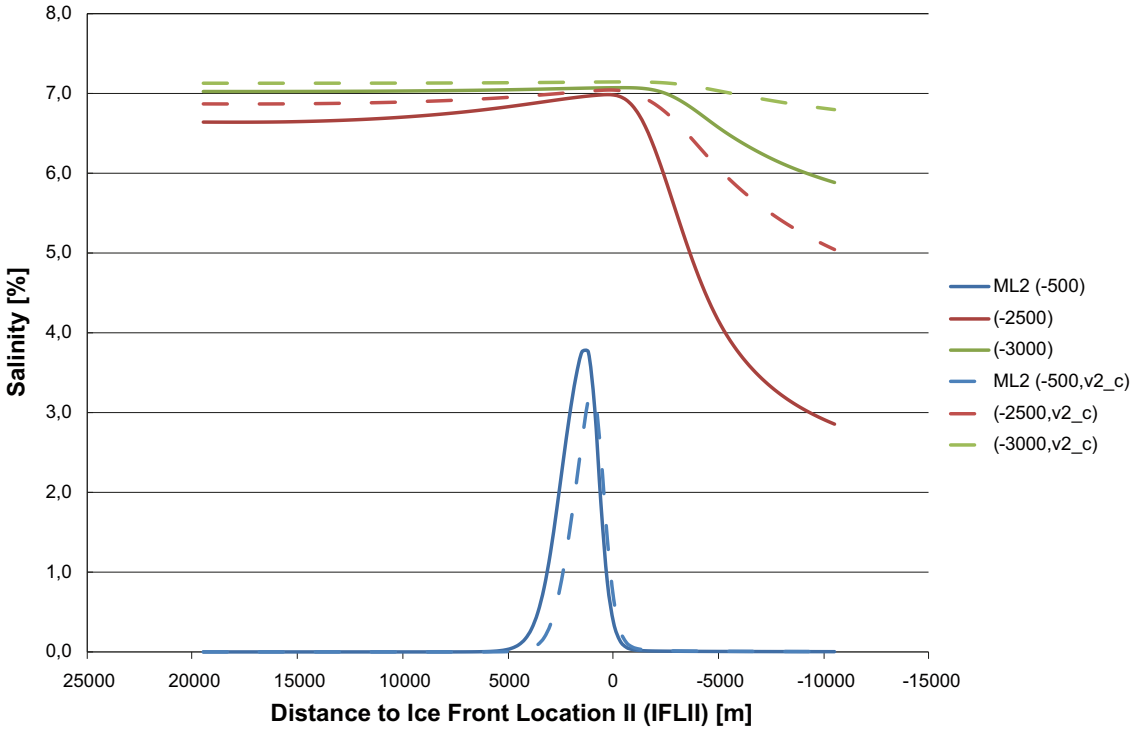

Figure 7-10. *Development of salinity along the ice front passage for four different depth locations along the ML2 locality line. Variant 2 along with Variant 2c (dashed). Positions to the right of 0 are covered by the ice sheet.*

7.2.6 Variant 3

The change in salinity during the ice front passage at four different depth locations along the ML2 location line is illustrated in Figure 7-11. For comparison, the results of Variant 1, described above, are also shown.

Compared to Variant 1, Variant 3 which has an extended deformation zone model (cf. Section 3.3 for details) cannot be distinguished from Variant 1. See Variant 1 for detailed accounts.

7.2.7 Variant 3d, Increased deformation zone transmissivity by a factor of 100

The change in salinity during the ice front passage at four different depth locations along the ML2 location line is illustrated in Figure 7-12. For comparison, for the results of Variant 1, described above, are shown.

Compared to Variant 3, Variant 3d shows a clear response at the depth of –500 m and –2,500 m due to the increased deformation zone transmissivity yielding a higher permeability at depth. Repository depth is initially characterised by fresh water but experiences a sudden increase during the ice front passage with peak values around 2.5% by weight.

The –2.5 kilometres deep location is found to experience a weak increase during the ice front passage. This slow increase continues for a longer period of time than the peak behaviour found at repository depth. After the passage, a slowly decreasing salinity is observed at this depth.

For the two deepest locations, –3,000 m and –3,500 m, no distinct increase during the ice front passage can be observed. However, both locations experience a minor but observable decrease after the passage. Compared to Variant, 3 the salinity is slightly more affected also at –3,000 m and –3,500 m. However, for all the deep locations, the salinity is still high after the ice front passage.

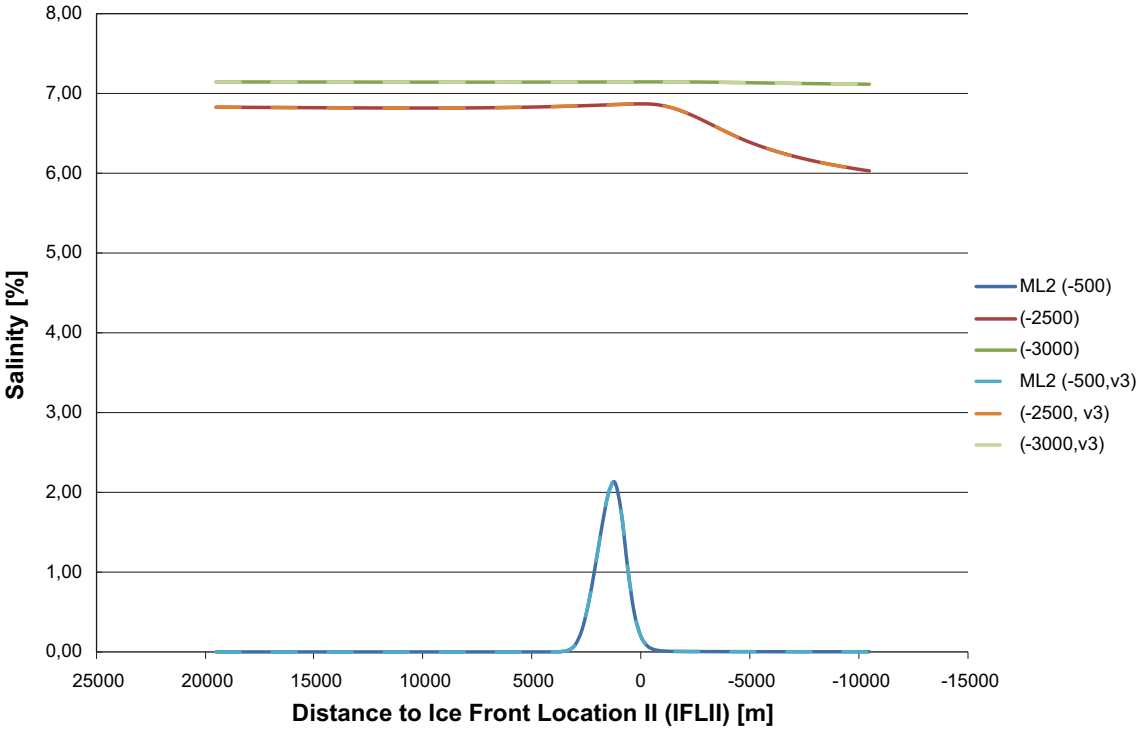

Figure 7-11. *Development of salinity along the ice front passage for four different depth locations along the ML2 locality line. Variant 1 along with Variant 3 (dashed). Positions to the right of 0 are covered by the ice sheet.*

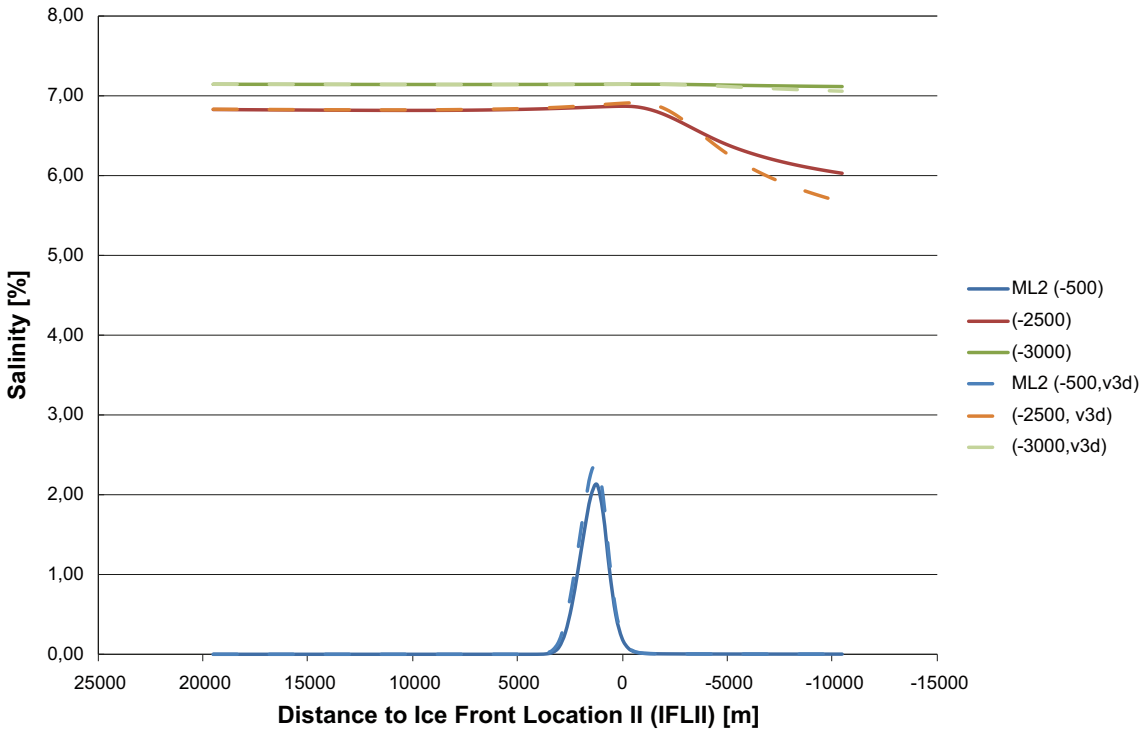

Figure 7-12. *Development of salinity along the ice front passage for four different depth locations along the ML2 locality line. Variant 1 along with Variant 3d (dashed). Positions to the right of 0 are covered by the ice sheet.*

7.2.8 Variant 4

The change in salinity during the ice front passage at four different depth locations along the ML2 location line is illustrated in Figure 7-12. For comparison, for the results of Variant 2, described above, are shown.

Compared to Variant 2, Variant 4 with an extended deformation zone model (cf. Section 3.3 for details), cannot be distinguished but shows the same results. See Variant 2 for detailed accounts.

7.2.9 Variant 5

The development of the salinity along with the ice front passage for four different depth locations along the ML2 location line, is illustrated in Figure 7-14 in comparison with the development for Variant 2, described above.

As compared with Variant 2, Variant 5 with a changed bottom boundary condition, cannot be distinguished but show the same results. See Variant 2 for detailed accounts.

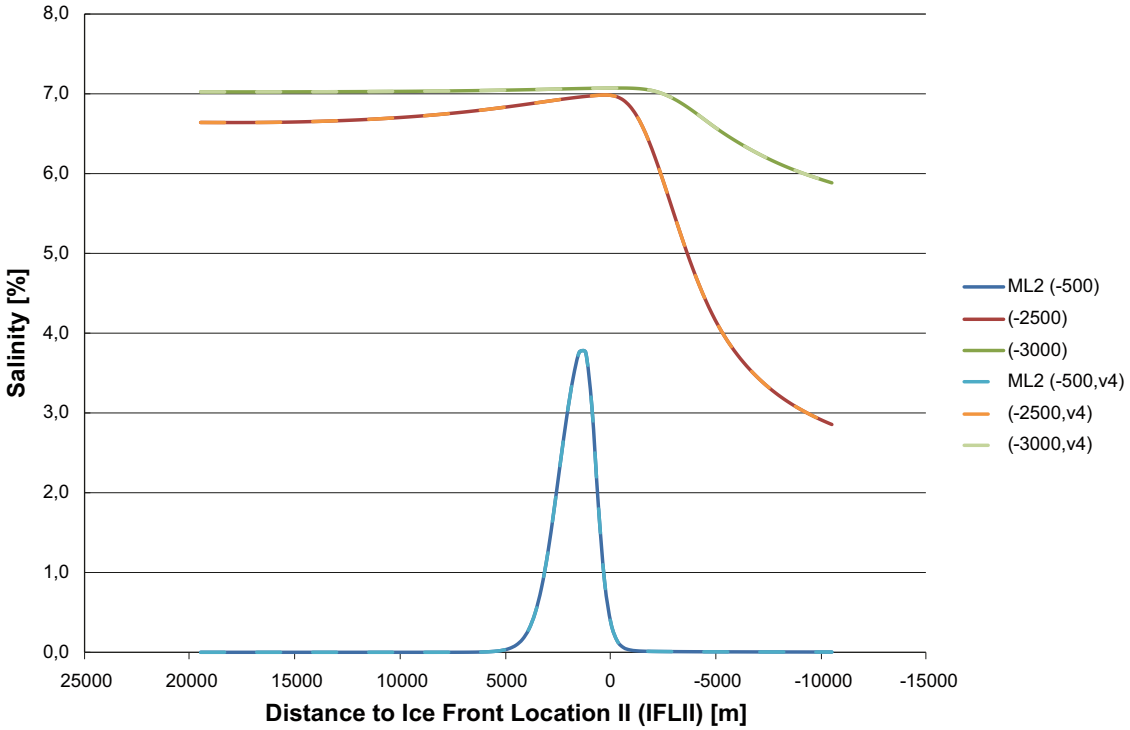

Figure 7-13. *Development of salinity along the ice front passage for four different depth locations along the ML2 locality line. Variant 2 along with Variant 4. Positions to the right of 0 are covered by the ice sheet.*

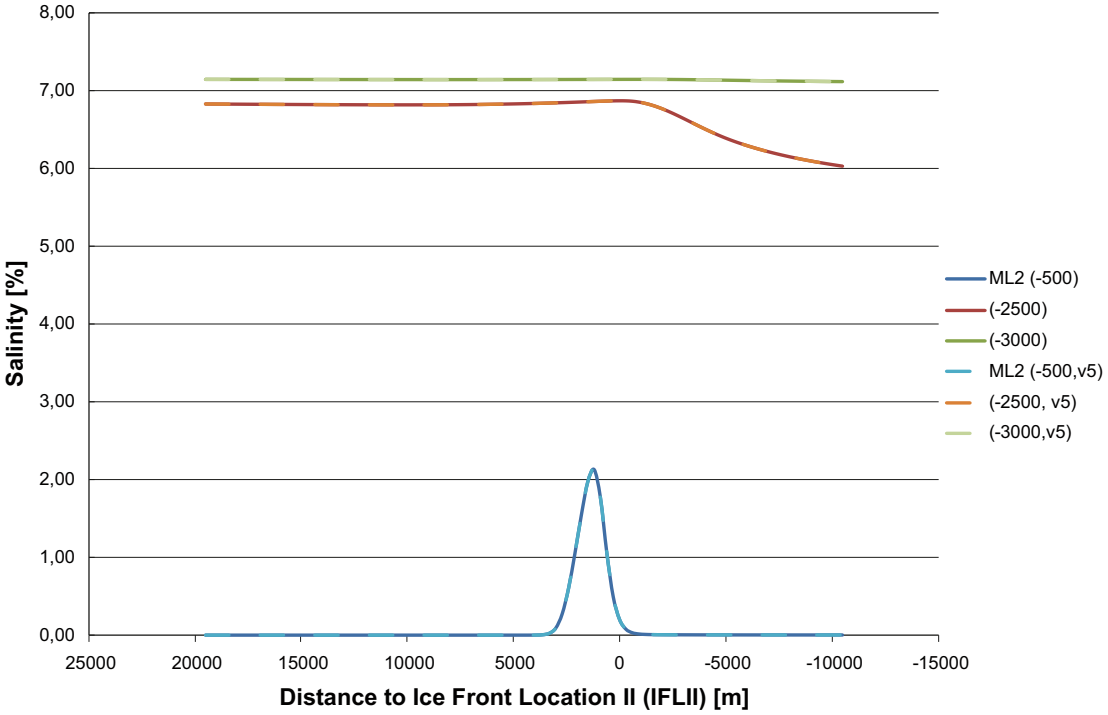

Figure 7-14. *Development of salinity along the ice front passage for four different depth locations along the ML2 locality line. Variant 2 along with Variant 5 (dashed). Positions to the right of 0 are covered by the ice sheet.*

7.3 Pressure during the ice front passage

The pressure at the four measurement localities are monitored transiently with time steps of 6 years, i.e. the ice front moves in a forward manner with about 300 metres per time increment.

Results from two of the tested variants are described in the subsequent Sections 7.3.1 to 7.3.2 below. The variants shown are Variant 1 and Variant 2, with the purpose of indicating the differences due to the permeability field at depth.

7.3.1 Variant 1

The development of the pressure during the ice front passage for four different depth locations along the ML2 location line is illustrated in Figure 7-15 .

The increase in pressure starts earlier at depth compared to at repository depth which in principle responds instantaneously to the top load during the passage. In the deeper parts with higher salinity the pressure increases well before the ice front passes over the locality.

For a short period after the passage of the ice front, the pressure at repository depth is higher than the pressure at the deeper measurement localities.

7.3.2 Variant 2

The development of the pressure during the ice front passage for two different depth locations along the ML2 location line is illustrated in Figure 7-16 together with the results of Variant 1.

The increase in pressure starts earlier at depth compared to at repository depth which in principle responds instantaneously to the top load during the passage. In the deeper parts with higher salinity the pressure increases well before the ice front passes over the locality. For a more permeable variant (Variant 2), the increase at depth is initiated even earlier but during the ice front passage the pressure curves merge.

For a short period after the passage of the ice front, the pressure at repository depth is higher than the pressure at the deeper measurement localities.

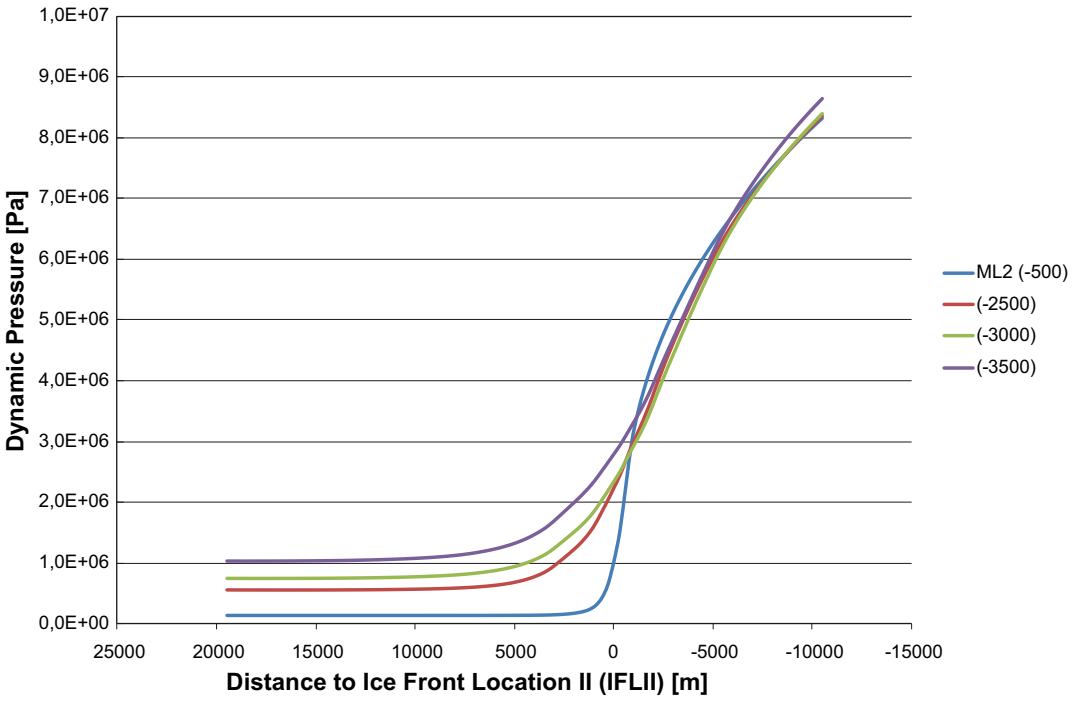

Figure 7-15. *Development of pressure along the ice front passage for four different depth locations along the ML2 locality line. The results are for Variant 1. Positions to the right of 0 are covered by the ice sheet.*

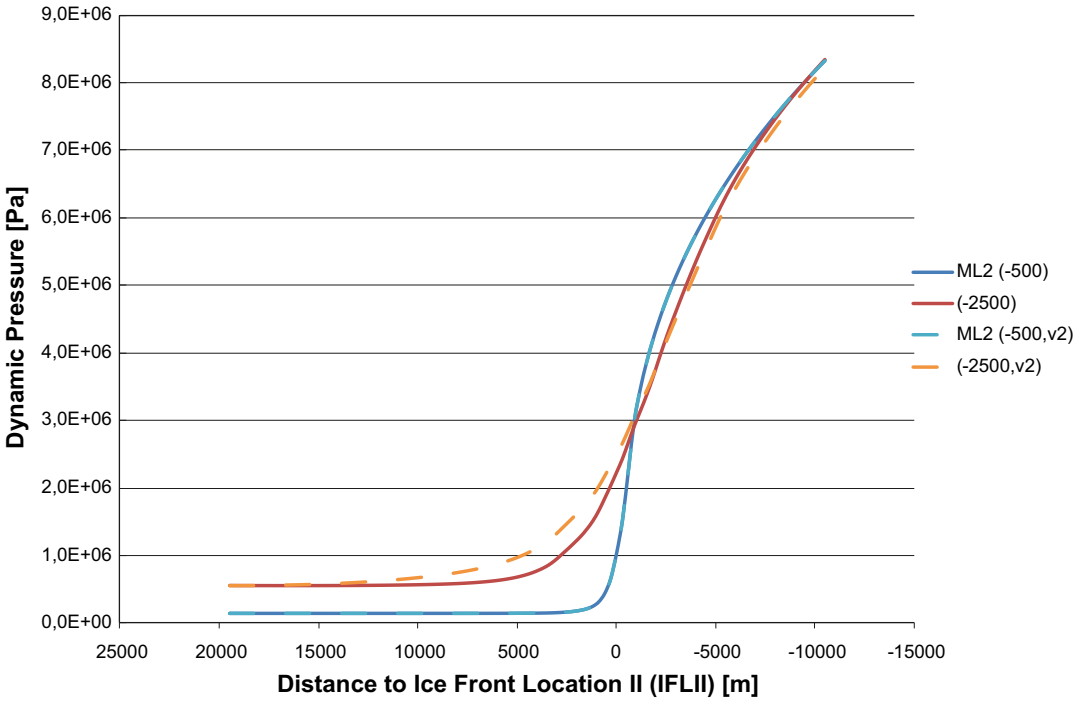

Figure 7-16. *Development of pressure along the ice front passage for two different depth locations along the ML2 locality line. Variant 1 compared with Variant 2. Positions to the right of 0 are covered by the ice sheet.*

8 Discussion

8.1 Introduction

Groundwater flow during glacial climate conditions is simulated in a 5.2 km deep, super-regional model domain. The sensitivity of the penetration depth of the hydraulic disturbance is studied by altering the hydraulic properties. The average advance rate and the thickness of the ice sheet profile are coordinated with SKB's climate report /SKB 2010/. The groundwater pressure, Darcy flux and salinity are monitored at four different depths along a vertical scan line through the centre of a KBS-3 type repository located at Laxemar. The depths of the monitoring points are –0.5 km (repository depth), –2.5 km, –3 km and –3.5 km.

8.2 Result summary

The magnitudes of the Darcy fluxes during temperate climate conditions are small; the temperate value is 10^{-11} m/s at –0.5 km and 10^{-13} m/s at –3.0 km. The relative increase in Darcy flux during the ice front passage is approximately two orders of magnitude at all measurement points.

At –0.5 km, where the water is initially fresh, the passage of the ice front causes a significant, temporal, increase in salinity, from 0% to above 2%. As the ice sheet margin moves forward, the salinity at –0.5 km decreases and eventually goes back to zero. At –3.5 km depth, the disturbance on the salinity is considerably less, in practise constant at the temperate value throughout the simulation.

8.3 Assumptions

The results reported here represent a groundwater flow model that is based on the following assumptions:

1. A super-regional model domain with a fixed resolution of the computational grid.
2. A thick ice sheet with a steep profile at the front.
3. A hydraulic pressure beneath the ice sheet that equals 92% of the ice thickness.
4. A low advance rate of the ice sheet margin.
5. No permafrost beneath the ice sheet or in front of the ice sheet margin.
6. Isotropic and homogeneous grid cell hydraulic properties beneath –2.1 km elevation.
7. Isothermal flow conditions.

These assumptions have the following consequences, among others:

1. A potential impact of numerical dispersion.
2. A floating ice sheet with a maximum recharge rate on the top boundary.
3. No thermally induced flows due to convection.

All assessments of ice sheet effects in the geosphere depend on the assumptions made concerning the driving forces created by the ice sheet. Herein, the modelled ice sheet represents an infinite source of melt water. The abundance of melt water is in turn responsible for raising the hydraulic pressure in the ground just beneath the ice/bedrock interface up to a freshwater head that equals 92% of the ice sheet thickness above the same location. This assumption implies a floating ice sheet. Higher pressures will not develop since all excess melt water immediately will be discharged above ground.

An assumption of an infinite melt water production is not necessarily the most likely situation even if it cannot be ruled out. Indeed, it has been shown in the literature that for some geological settings, the sub-glacial pressures reach the floatation pressure at least for parts of a year, see e.g. /Boulton et al. 2007/. Still, assessing the floatation pressure is an assumption leading to a maximum hydraulic disturbance on the geosphere due to an ice sheet.

Further, the advancing ice sheet is assumed to have a shape that maximises the hydraulic pressure at the ice front margin. The advance rate of the ice sheet margin is relatively low over the permeable, non-frozen, ground. However, for most situations, the ice sheet will advance over a permafrost affected region. Such conditions will change the effects of the strong hydraulic gradient from an influence on the vertical advective flow component towards a larger change in the horizontal advective flow components. This change is due to the fact that permafrost almost completely inhibits through flow. Hence, when permafrost is present, discharge primarily occurs in taliks (unfrozen parts in the ground); taliks may very well be located at a significant distance from the recharge beneath the ice sheet. The groundwater flow is hence forced horizontally beneath the permafrost towards discharge locations within taliks. As permafrost is not a part of this study the effects on the vertical advective flow is likely overestimated while on the other hand the effects on the horizontal advective flow is most likely somewhat underestimated.

Investigating the changes in salinity, pressure, and Darcy flux at great depths within the deep saline waters in a numerical model relies heavily on the correctness of the assessed boundary conditions for the saline water domain, along with the hydraulic properties at depth, e.g. grid cell permeability and kinematic porosity. The results reported here are associated with uncertainties since the knowledge of properties at depth is limited. The extrapolated properties based on hydraulic information from deformation zones are less likely representative for the bulk rock mass at great depth.

Figure 8-1shows the depth-trend functions for the hydraulic conductivity (K) that have provided the basis for the assignment of the hydraulic conductivity in the groundwater flow model. The figure is the same as Figure 3-2 but with data from the deep boreholes KLX02 added as an example. The points above 1,000 m depth have a test scale of 100 m, and points below 1,000 m have a test scale of c 300 m. In the figure it is indicated if the test section is intersected by a large conductive deterministic deformation zone, here called HCD. If no HCD is present, the data represent rock between the deformation zones, here called HRD. The variability of individual 100 m sections is large within depth intervals (std(Log10(K))= c 1 to 1.7) , as was shown in /Rhén et al. 2008/ and as indicated by the few HRD values in Figure 8-1. The trend functions in /Rhén et al. 2009/ was based on data with test section length of 100 m down to a depth of c 1,000 m but as can be seen in the figure the two 300 m sections below 1,000 m depth are fairly close to the trend function for HCDs. These two sections include heavily fractured sections, cf. /Ekman 2001/, comparable with sections above 1,000 m depth defined as HCDs. The high permeability within the highly fractured part of KLX02 between borehole length 1,000 to 1,120 m is confirmed by PFL-test results /Rhén et al. 2006/. As pointed out in Section 3.2, other sites in crystalline rock where data from great depths are available indicate similar ranges as the trend functions in Figure 8-1.

Conceptually, groundwater flow models rely on that, in the time span modelled, saline waters can be viewed as stationary, i.e. non-flowing, within the bounds of the model domain simulated. The fresh water on top of the saline waters are more governed by local topographical gradients than the deep saline waters e.g. /Ericsson and Holmén 2010/. Further, the saline waters are likely to incorporate deep and local flow cells caused by temperature differences (convection), deep gas migration, or tidal effects all effective within the highly heterogeneous bedrock e.g. /Raffensperger and Vlassopoulos 1999, Svensson et al. 2008/. Together, these matters point at deep saline waters that are within a slow transient movement. Hence, it is not realistic to assume that the numerically modelled values of salinity and Darcy fluxes at great depth are entirely correct, since it is assumed that the salinity field at the model boundary at 5.2 km depth is stable and non-flowing. At best, the relative changes caused by the ice front passage indicate the order of magnitude effect the ice sheet has on the geosphere.

In DarcyTools, dispersion effects in salt transport calculations are mainly related to the chosen spatial discretisation, i.e. grid cell size and grid cell orientation, since DarcyTools uses a fully implicit time solution routine and hydrodynamic dispersion is not modelled, see Chapter 4. A scoping calculation using the simulated vertical grid cell component of the Darcy flux solution at –2,500 m elevation, $(1\text{-}10)\cdot10^{-11}$ m/s, suggests that during the time it takes for the ice front to pass the position of the scan line (here assessed as 50 years), the vertical advective flux could transport water particles somewhere between 160–1,600 metres depending on the cell specific kinematic porosity used (here assumed to be $1\cdot10^{-4}$). In comparison, the vertical advective flux during temperate climate boundary conditions could transport water particles on the order of a few centimetres. This significant difference in flux-related transport distance suggests that the simulated changes reported here are not simply due to numerical dispersion in the salt transport calculations.

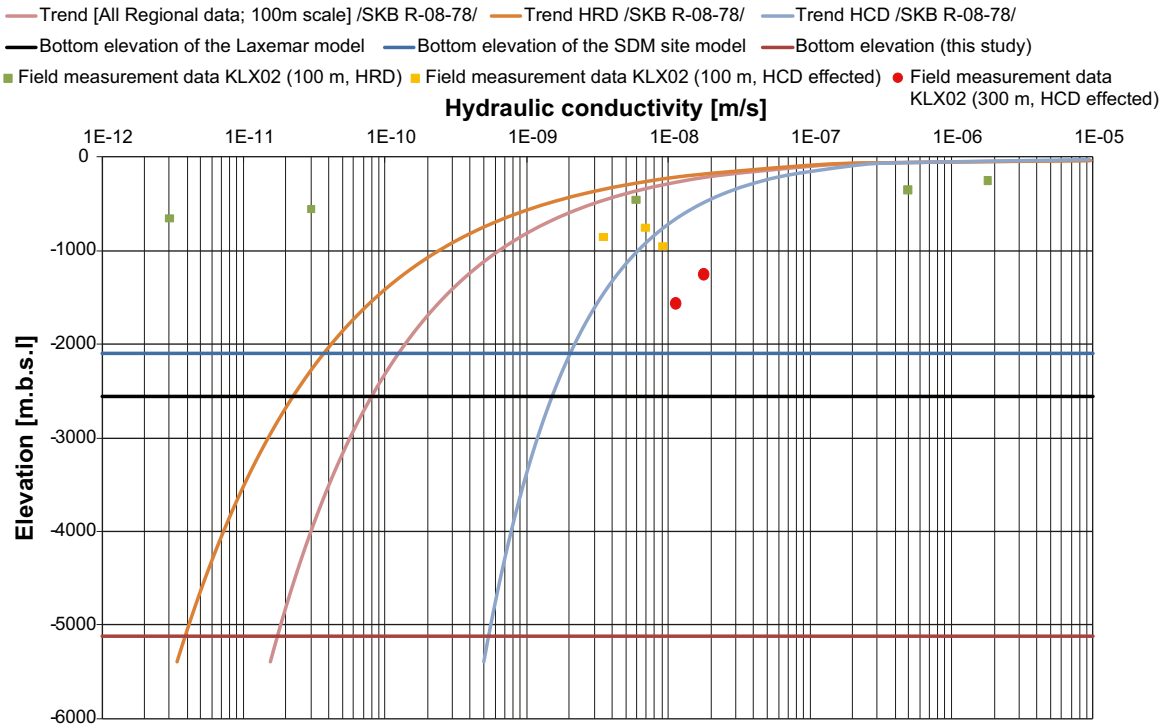

Figure 8-1. *Illustration of the assessed depth trends presented in /Rhén et al. 2008/. The dots illustrate field measurement data from KLX02.*

After the passage of the ice front, the ice sheet covers the site with an initially downward directed vertical advective flux that is on the same order of magnitude as the upconing related flux at the ice front. However, in contrast to the ice front related flux, the downward flux behind the ice front will prevail for many hundreds of years continuously but slowly pushing the elevated salt downward beneath the ice sheet. During the long period of complete ice coverage that follows the passage of ice front, the hydraulic gradients at depth are very small; hence it takes several thousands of years before the grid cell salinity at –2.5 km depth is fully recovered. The deep saline waters seem to adjust to these movements with an elevated interface in-front of the ice sheet much in the same way as the Earth's crust creates a forebulge in front of the ice sheet as a response to isostatic movements.

In summary, it is plausible that the tested model specifications are relevant for calculating indicative results of relative changes in salinity, pressures, and Darcy fluxes due to a passage of an ice front.

8.4 Discussion of results

Concerning the sensitivity of the results, it is clearly observed that an increase in the kinematic porosity dampens the simulated salinity changes both at repository depth as well as in the deeper model sections. The importance of this issue for the work reported here is not readily addressed since it is difficult to assign a realistic grid cell kinematic porosity value when the fracture spacing is low. On longer time scales, such as a glaciation sequence, it may be even more difficult to realistically model the salinity evolution since part of the total porosity may become important in terms of matrix diffusion during the long period of slow advective transport.

Extending the regional deformation zones does not affect the results as long as the properties are maintained as specified in the SDM-Site work. However, an increase of two orders of magnitude in deformation zone transmissivity yields a higher and heterogeneous permeability at depth and consequently affects the results in all monitored depth locations. The sensitivity case investigated here implies changes in resulting salinity values by a factor of 2–3. Also the time during which an initially fresh repository depth is exposed to a higher salinity can be expected to be effected; however, the time scale of such a change is still short and not deemed significant on a glacial-cycle time scale.

In the deep model used in this study, a changed bottom boundary condition from fixed salinity value to a specified zero flux of salt at –5.2 km, does not affect the monitored performance measures in any of the observed localities. This implies that the depth of the model domain is sufficient.

In all simulations studied in the work reported here, a decrease in salinity of at least 1% by weight is observed at –2.5 km. It is noted that this elevation coincides with the depth of the no-flow boundary and fixed salinity bottom layer of the Laxemar model studied by /Vidstrand et al. 2010b/. Although the fixed salinity used at the bottom layer in /Vidstrand et al. 2010b/ obviously implies a salt source, it is concluded that the change in salinity at –0.5 km, which was the focus of the Laxemar model in /Vidstrand et al. 2010b/, is the same as in this study. Hence, the no flow boundary and fixed salinity bottom layer of the Laxemar model used in /Vidstrand et al. 2010b/ does not considerably affect the results inferred for a repository at –0.5 km.

In comparison, the results from the study of groundwater flow during glacial climate conditions at Forsmark for SR-Site by /Vidstrand et al. 2010a/ appear more robust as the permeability already at a repository depth of –500 m are significantly lower compared to the Laxemar site values at –2 km. Hence, the handling of the hydrogeological conditions at the bottom boundary in /Vidstrand et al. 2010a/ are considered appropriate for the objectives of SR-Site.

Finally, the apparent uncertainty of the salinity trend with depth is tested with two variants. It is concluded that a more saline model results in slightly higher salinity values during the peak caused by the upconing event during the ice front passage. However, it is not possible to be more conclusive on the realism of the alternative salinity trend without data.

9 Conclusions

This study is conducted in order to investigate the question whether a potential site, under certain conditions, could experience a hydrogeological disturbance at a depth of 2–4 km. The simulations are based on a model that maximises the potential impact. This means that the influence of the adopted top boundary condition is maximised and the permeability of the bedrock is maximised.

Based on the simulation results, a set of general conclusions can be stated:

The salinity at repository depth responds to the parameterisation at depth. Especially, the chosen permeability at depth is important. If a more permeable model at depth is chosen, the assumed initial conditions concerning salt become more important.

Even if a change to more permeable conditions at depth is imposed, the duration of an increased salinity at repository depth (–0.5 km) is not affected significantly. Instead, the increased salinity is strongly correlated to the duration of the passage of the ice front.

All measurement points below 2 km depth show a response to the passage of the ice front in terms of increasing pressures and Darcy fluxes. The responses at depth, though similar to the shallower locality in terms of relative change, do not cause any high Darcy fluxes and possible advective transport distances, for e.g. salt are limited. Responses are larger for more permeable conditions at depth. Hence, the deep groundwater system is not completely stable, i.e. a water particle could experience upward as well as downward transport depending on the location of the ice sheet margin. However, the results obtained do not indicate that a significant depletion of salt in the deep bedrock is plausible.

The results of this study imply that the fixed salinity used at the bottom layer in the Laxemar model /Vidstrand et al. 2010b/ obviously function as a salt source. However it is concluded that the change in salinity at –0.5 km, which was the focus of the Laxemar model is the same as in this study. Hence, the no flow boundary and fixed salinity bottom layer of the Laxemar model used in /Vidstrand et al. 2010b/ does not considerably affect the results inferred for a repository at –0.5 km.

10 References

SKB's (Svensk Kärnbränslehantering AB) publications can be found at www.skb.se/publications.

Boulton G S, Lunn R J, Vidstrand P, Zatsepin S, 2007. Subglacial drainage by groundwater-channel coupling, and the origin of esker systems: Part I – glaciological observations. Quaternary Science Reviews, 26, pp 1067–1090.

Chan T, Christiansson R, Boulton G S, Ericsson L O, Hartikainen J, Jensen M R, Mas Ivars D, Stanchell F W, Vistrand P, Wallroth T, 2005. DECOVALEX III BMT3/BENCHPAR WP4: The thermo-hydro-mechanical responses to a glacial cycle and their potential implications for deep geological disposal of nuclear fuel waste in a fractured crystalline rock mass. International Journal of Rock Mechanics and Mining Sciences, 42, pp 805–827.

Dershowitz W, Winberg A, Hermanson J, Byegård J, Tullborg E-L, Andersson P, Mazurek M, 2003. Äspö Hard Rock Laboratory. Äspö Task Force on modelling of groundwater flow and transport of solutes. Task 6c. A semi-synthetic model of block scale conductive structures at the Äspö HRL. SKB IPR-03-13, Svensk Kärnbränslehantering AB.

Ekman L, 2001. Project Deep Drilling KLX02 – Phase 2. Methods, scope of activities and results. Summary report. SKB TR-01-11, Svensk Kärnbränslehantering AB.

Ericsson L O, Holmén J, 2010. Storregional grundvattenmodellering – en känslighetsstudie av några utvalda konceptuella beskrivningar och förenklingar. SKB R-10-43, Svensk Kärnbränslehantering AB.

Ericsson L O, Holmén J, Rhén I, Blomquist N, 2006. Storregional grundvattenmodellering – fördjupad analys av flödesförhållanden i östra Småland. Jämförelse av olika konceptuella beskrivningar. SKB R-06-64, Svensk Kärnbränslehantering AB.

Follin S, 2008. Bedrock hydrogeology Forsmark. Site descriptive modelling, SDM-Site Forsmark. SKB R-08-95, Svensk Kärnbränslehantering AB.

Follin S, Svensson U, 2003. On the role of mesh discretisation and salinity for the occurrence of local flow cells. Results from a regional-scale groundwater flow model of Östra Götaland. SKB R-03-23, Svensk Kärnbränslehantering AB.

Follin S, Stigsson M, Svensson U, 2005. Variable-density groundwater flow simulations and particle tracking – numerical modelling using DarcyTools. Preliminary site description Simpevarp subarea – version 1.2. SKB R-05-11, Svensk Kärnbränslehantering AB.

Follin S, Hartley L, Jackson P, Roberts D, Marsic N, 2008. Hydrogeological conceptual model development and numerical modelling using CONNECTFLOW, Forsmark modelling stage 2.3. SKB R-08-23, Svensk Kärnbränslehantering AB.

Fredén C (ed), 2002. Sveriges nationalatlas. Berg och Jord (in Swedish). Stockholm: SNA publishing.

Haggerty R, Gorelick S M, 1995. Multiple-rate mass transfer for modeling diffusion and surface reactions i media with pore-scale heterogeneity. Water Resources Research, 31, pp 2383–2400.

Harlow F H, Welsch J E, 1965. Numerical calculations of time-dependent viscous incompressible flow of fluid with free surface. Physics of Fluids, 8, pp 2182–2189.

Holmén J G, 2008. Premodelling of the importance of the location of the upstream hydraulic boundary of a regional flow model of the Laxemar-Simpevarp area. Site descriptive modeling, SDM-Site Laxemar. SKB R-08-60, Svensk Kärnbränslehantering AB.

Holmén J G, Stigsson M, Marsic N, Gylling B, 2003. Modelling of groundwater flow and flow paths for a large regional domain in northeast Uppland. A three-dimensional, mathematical modelling of groundwater flows and flow paths on a super-regional scale, for different complexity levels of the flow domain. SKB R-03-24, Svensk Kärnbränslehantering AB.

Jaquet O, Siegel P, 2006. Regional groundwater flow model for a glaciation scenario. Simpevarp subarea – version 1.2. SKB R-06-100, Svensk Kärnbränslehantering AB.

Joyce S, Simpson T, Hartley L, Applegate D, Hoek J, Jackson P, Roberts D, Swan D, Gylling B, Marsic N, Rhén I, 2010. Groundwater flow modelling of periods with temperate climate conditions – Laxemar. SKB R-09-24, Svensk Kärnbränslehantering AB.

Juhlin C, Wallroth T, Smellie J, Eliasson T, Ljunggren C, Leijon B, Beswick J, 1998. The Very Deep Hole Concept – Geoscientific appraisal of conditions at great depth. SKB TR 98-05, Svensk Kärnbränslehantering AB.

Laaksoharju M, Smellie J, Tullborg E-L, Wallin B, Drake H, Gascoyne M, Gimeno M, Gurban I, Hallbeck L, Molinero J, Nilsson A-C, Waber N, 2009. Bedrock hydrogeochemistry Laxemar. Site descriptive modelling, SDM-Site Laxemar. SKB R-08-93, Svensk Kärnbränslehantering AB.

Larsson-McCann S, Karlsson A, Nord M, Sjögren J, Johansson L, Ivarsson M, Kindell S, 2002. Meteorological, hydrological and oceanographical information and data for the site investigation program in the community of Oskarshamn. SKB TR-02-03, Svensk Kärnbränslehantering AB.

Lemieux J-M, Sudicky E A, Peltier W R, Tarasov L, 2008a. Simulating the impact of glaciations on continental groundwater flow systems: 1. Relevant processes and model formulation. Journal of Geophysical Research, 113, F03017, doi:10.1029/2007JF000928.

Lemieux J-M, Sudicky E A, Peltier W R, Tarasov L, 2008b. Simulating the impact of glaciations on continental groundwater flow systems: 2. Model application to the Wisconsinian glaciation over the Canadian landscape. Journal of Geophysical Research, 113, F03018, doi:10.1029/2007JF000929.

Lemieux J-M, Sudicky E A, Peltier W R, Tarasov L, 2008c. Dynamics of groundwater recharge and seepage over the Canadian landscape during the Wisconsinian glaciation. Journal of Geophysical Research, 113, F01011, doi:10.1029/2007JF000838.

Lönnqvist M, Hökmark H, 2010. Assessment of potential for glacially induced hydraulic jacking at different depths. SKB R-09-35, Svensk Kärnbränslehantering AB.

Nyman H, Sohlenius G, Strömgren M, Brydsten L, 2008. Depth and stratigraphy of regolith. Site descriptive modelling, SDM-Site Laxemar. SKB R-08-06, Svensk Kärnbränslehantering AB.

Patankar S V, 1980. Numerical heat transfer and fluid flow. New York: Hemisphere.

Paterson W S B, 1994. The physics of glaciers. Elsevier Science Ltd. Third edition.

Raffensperger J P, Vlassopoulos D, 1999. The potensial for free and mixed convection in sedimentary basins. Hydrogeology Journal, 7, pp 505–520.

Rhén I, Hartley L, 2009. Bedrock hydrogeology Laxemar. Site descriptive modelling, SDM-Site Laxemar. SKB R-08-92, Svensk Kärnbränslehantering AB.

Rhén I, Follin S, Hermanson J, 2003. Hydrological Site Descriptive Model – a strategy for its development during site investigations. SKB R-03-08, Svensk Kärnbränslehantering AB.

Rhén I, Forsmark T, Forsman I, Zetterlund M, 2006. Evaluation of hydrogeological properties for Hydraulic Conductor Domains (HCD) and Hydraulic Rock Domains (HRD). Laxemar subarea – version 1.2. SKB R-06-22, Svensk Kärnbränslehantering AB.

Rhén I, Forsmark T, Hartley L, Jackson P, Roberts D, Swan D, Gylling B, 2008. Hydrogeological conceptualisation and parameterisation. Site descriptive modelling, SDM-Site Laxemar. SKB R-08-78, Svensk Kärnbränslehantering AB.

Rhén I, Forsmark T, Hartley L, Joyce S, Roberts D, Gylling B, Marsic N, 2009. Bedrock hydrogeology. Model testing and synthesis. Site descriptive modelling, SDM-Site Laxemar. SKB R-08-91, Svensk Kärnbränslehantering AB.

SKB, 2006a. Climate and climate-related issues for the safety assessment SR-Can. SKB TR-06-23, Svensk Kärnbränslehantering AB.

SKB, 2006b. Preliminary site description. Laxemar subarea – version 1.2. SKB R-06-10, Svensk Kärnbränslehantering AB.

SKB, 2008. Site description of Forsmark at completion of the site investigation phase. SDM-Site Forsmark. SKB TR-08-05, Svensk Kärnbränslehantering AB.

SKB, 2009. Site description of Laxemar at completion of the site investigation phase. SDM-Site Laxemar. SKB TR-09-01, Svensk Kärnbränslehantering AB.

SKB, 2010. Climate and climate-related issues for the safety assessment SR-Site. SKB TR-10-49, Svensk Kärnbränslehantering AB.

Smellie J, 2004. Recent geoscientific information relating to deep crustal studies. SKB R-04-09, Svensk Kärnbränslehantering AB.

Smellie J, Tullborg E-L, Nilsson A-C, Sandström B, Waber N, Gimeno M, Gascoyne M, 2008. Explorative analysis of major components and isotopes. SDM-Site Forsmark. SKB R-08-84, Svensk Kärnbränslehantering AB.

Sohlenius G, Hedenström A, 2008. Description of regolith at Laxemar-Simpevarp. Site descriptive modelling, SDM-Site Laxemar. SKB R-08-05, Svensk Kärnbränslehantering AB.

SSM, 2009. Granskning av SKB:s komplettering av Fud-program 2007. Stockholm: Strålsäkerhetsmyndigheten (Swedish Radiation Safety Authority). (SSM 2009/1365).

Svensson U (ed), Vidstrand P, Neretnieks I, Wallin B, 2008. Towards a new generation of flow and transport models for the Äspö Hard Rock Laboratory. Main results from the project Äspömodels 2005. SKB R-08-74, Svensk Kärnbränslehantering AB.

Svensson U, Ferry M, Kuylenstierna H-O, 2010. DarcyTools, Version 3.4. Concepts, methods and equations. SKB R-07-38, Svensk Kärnbränslehantering AB.

Vidstrand P, Näslund J-O, Hartikainen J, Svensson U, 2007. Hydrogeological flux scenarios at Forsmark. Generic numerical flow simulations and compilation of climatic information for use in the safety analysis SFR1 SAR-08. SKB R-07-63, Svensk Kärnbränslehantering AB.

Vidstrand P, Follin S, Zugec N, 2010a. Groundwater flow modelling of periods with periglacial and glacial climate conditions – Forsmark. SKB R-09-21, Svensk Kärnbränslehantering AB.

Vidstrand P, Rhén I, Zugec N, 2010b. Groundwater flow modelling of periods with periglacial and glacial climate conditions – Laxemar. SKB R-09-25, Svensk Kärnbränslehantering AB.

Vilks P, 2007. Oskarshamn site investigation. Rock matrix permeability measurements on core samples from borehole KLX03. SKB P-07-204, Svensk Kärnbränslehantering AB.

Wahlgren C-H, Curtis P, Hermanson J, Forssberg O, Öhman J, Fox A, La Pointe P, Drake H, Triumf C-A, Mattsson H, Thunehed H, Juhlin C, 2008. Geology Laxemar. Site descriptive modelling, SDM-Site Laxemar. SKB R-08-54, Svensk Kärnbränslehantering AB.

Walsh R, Avis J, 2010. Glacial scenario: groundwater and radionuclide transport studies. NWMO TR-2010-09, Nuclear waste Management Organization, Canada.

Werner K, Öhman J, Holgersson B, Rönnback K, Marelius F, 2008. Meteorological, hydrological and hydrogeological monitoring data and near-surface hydrogeological properties data from Laxemar-Simpevarp. Site descriptive modelling, SDM-Site Laxemar. SKB R-08-73, Svensk Kärnbränslehantering AB.

Appendix A

Parameters for HRD modelling

A.1 Introduction

This appendix presents the model parameters used in DarcyTools for generating stochastic hydro-geological discrete fracture network (DFN) properties of the fracture domains within the focused area. The up-scaling of these properties to equivalent continuous porous medium (ECPM) properties is conducted inside the code DarcyTools, see /Svensson et al. 2010/ for details. This appendix specifies also the hydraulic continuous porous media (CPM) properties used for the fracture domain located outside the SDM-Site regional flow domain.

A.2 Fracture size-intensity relationship

In DarcyTools, the number of fractures (n) in the size range [L, $L+dL$] may be calculated as:

$$n = I\left[\left(\frac{L+dL}{L_{ref}}\right)^{D} - \left(\frac{L}{L_{ref}}\right)^{D}\right] / D \qquad \text{(A-1)}$$

where I is the number of fractures of size L_{ref} per unit volume and D is the exponent (shape factor) of a power law size distribution. The relationships between the notation used in DarcyTools and that reported for SDM-Site Laxemar may be written as:

$$L_0 = r_0 \cdot \sqrt{\pi} \qquad \text{(A-2)}$$

$$I = P_{32}\,[r_0, \infty] \cdot L_0^{(k_r-2)} / L_{ref}^{k_r} \qquad \text{(A-3)}$$

$$D = -k_r \qquad \text{(A-4)}$$

$$\lambda_1 = \cos(90-tr)\cdot\cos(pl)\cdot\kappa \qquad \text{(A-5)}$$

$$\lambda_2 = \sin(90-tr)\cdot\cos(pl)\cdot\kappa \qquad \text{(A-6)}$$

$$\lambda_3 = -\sin(pl)\cdot\kappa \qquad \text{(A-7)}$$

where L_0 [m] equals the side length of the smallest fracture generated (represented as a square), r_0 [m] is its equivalent radius and $P_{32}[r_0,\infty]$ [L^2/L^3] is the fracture surface area per unit volume for all fractures in the size range [r_0,∞]. Each fracture set is assumed to obey a Fisher distribution of its own, which is characterised by a Fisher concentration κ, a mean trend tr and a mean plunge pl. Moreover, the sizes of the generated fractures are assumed to be power-law distributed, with one shape factor k_r per fracture set. The orientations of the generated fractures are fully described by λ_1–λ_3, which are the normal vectors.

The relationship between the incremental fracture intensity, $P_{32}[r_1, r_2]$, and the total intensity, $P_{32}[r_0,\infty]$, may be written as:

$$P_{32}[r_1, r_2] = P_{32}[r_0, \infty]\left(\frac{(r_1)^{(2-k_r)} - (r_2)^{(2-k_r)}}{(r_0)^{(2-k_r)}}\right) \qquad \text{(A-8)}$$

A.3 Fracture input statistics

As explained in the work by /Joyce et al. 2010/, two hydrogeological discrete fracture network (Hydro-DFN) models are defined at Laxemar; the Hydrogeological base case and the Elaborated Hydro-DFN.

- The first model, the Hydrogeological base case, builds upon the Hydro-DFN model derived within SDM-Site /Rhén and Hartley 2009/.
- The second model, the Elaborated Hydro-DFN, is a refinement of the Hydrogeological base case /Joyce et al. 2010/.

The reason for the Elaboarted Hydro-DFN can be summarised as follows. During SDM-Site, the flow modelling of the palaeohydrogeological evolution at the Laxemar site showed that the derived Hydro-DFN for SDM-Site (i.e. the Hydrogeological base case) is slightly too transmissive. Reducing the permeabilities below –150 m by a factor of three improved the match to measured values. This calibration resulted in the Elaborated Hydro-DFN.

For the detailed defined HRDs illustrated in Figure A-1, statistics described in Table A-1 to A-12 was used for generation of one realisation of fractures. The Elaborated Hydro-DFN was used for all fracture domains except HRD_N where the SDM-Site Hydro-DFN was used.

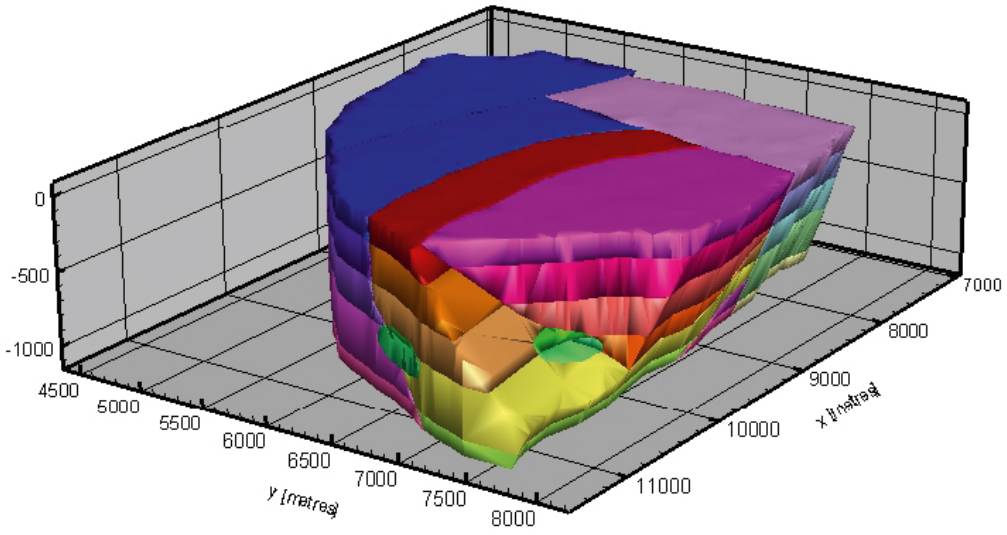

Figure A-1. *Illustrations of HRD assessed in the SDM local model. The upper layer consists of HRD_C (blue), HRD_EW007 (red), HRD_N (purple), and HRD_W (greyish purple). The layers beneath consists of the different depth intervals.*

Table A-1. Parameters values used for fracture domain HRD_C.(based on data from /Joyce et al. 2010/).

Elevation [m RHB 70]	Fracture set name	Orientation set pole: (trend, plunge), conc. κ [°,°, –]	Size model, power-law (k_r , r_0) [– , m]	Intensity, ($P_{32,open}$), valid size interval: (r_0, 564 m) [m^2/m^3]	Semi-correlated transmissivity model $log(T) = log(a\ r^b)+\sigma_{log(T)}\ N(0,1)$)
–150 to 0	ENE	(155.1,3.4), 9.6	(2.70, 0.038)	0.52	SC: (2 10^{-7}, 0.7, 0.4)
	WNW	(204,1.6), 12	(2.49, 0.038)	0.95	SC: (2 10^{-7}, 0.9, 0.6)
	N-S	(270.2,8.4), 7.8	(2.80, 0.038)	0.54	SC: (8 10^{-8}, 0.5, 0.4)
	Sub-H	(46.3,84.7), 12	(2.59, 0.038)	1.20	SC: (6 10^{-8}, 0.7, 0.5)
–400 to –150	ENE	(155.1,3.4), 9.6	(3.00, 0.038)	0.47	SC: (6 10^{-7}, 0.7, 0.9)
	WNW	(204,1.6), 12	(2.44, 0.038)	0.55	SC: (1 10^{-8}, 0.5, 0.7)
	N-S	(270.2,8.4), 7.8	(2.91, 0.038)	0.63	SC: (1 10^{-8}, 0.7, 0.2)
	Sub-H	(46.3,84.7), 12	(2.87, 0.038)	0.71	SC: (3.5 10^{-8}, 1.2, 0.9)
–650 to –400	ENE	(155.1,3.4), 9.6	(2.87, 0.038)	0.38	SC: (8 10^{-8}, 0.8, 0.6)
	WNW	(204,1.6), 12	(2.54, 0.038)	0.74	SC: (3 10^{-9}, 0.8, 0.6)
	N-S	(270.2,8.4), 7.8	(2.87, 0.038)	0.47	SC: (6 10^{-9}, 0.4, 0.4)
	Sub-H	(46.3,84.7), 12	(3.00, 0.038)	0.58	SC: (2 10^{-7}, 0.8, 0.7)
below –650	ENE	(155.1,3.4), 9.6	(2.96, 0.038)	0.46	SC: (1 10^{-8}, 0.7, 0.4)
	WNW	(204,1.6), 12	(3.00, 0.038)	0.73	SC: (3 10^{-7}, 0.7, 0.4)
	N-S	(270.2,8.4), 7.8	(3.00, 0.038)	0.25	SC: (1 10^{-8}, 0.7, 0.4)
	Sub-H	(46.3,84.7), 12	(2.97, 0.038)	0.35	SC: (1 10^{-7}, 0.7, 0.4)

Table A-2. DFN parameter values used in the present report for fracture domain HRD_C.

Elevation [m RHB 70]	Set	λ_1 (–)	λ_2 (–)	λ_3 (–)	D (–)	l_{ref} (m)	l (m^{-3})
–150 to 0	ENE	4.03483	–8.69230	–0.56934	–2.70	1	0.05514
	WNW	–4.87894	–10.95827	–0.33506	–2.49	1	0.12524
	NS	–7.71628	0.02693	–1.13945	–2.80	1	0.04993
	sub-H	0.80137	0.76581	–11.94870	–2.59	1	0.14463
–400 to –150	ENE	4.03483	–8.69230	–0.56934	–3.00	1	0.03166
	WNW	–4.87894	–10.95827	–0.33506	–2.44	1	0.07493
	NS	–7.71628	0.02693	–1.13945	–2.91	1	0.04923
	sub-H	0.80137	0.76581	–11.94870	–2.87	1	0.05910
–650 to –400	ENE	4.03483	–8.69230	–0.56934	–2.87	1	0.03163
	WNW	–4.87894	–10.95827	–0.33506	–2.54	1	0.09362
	NS	–7.71628	0.02693	–1.13945	–2.87	1	0.03912
	sub-H	0.80137	0.76581	–11.94870	–3.00	1	0.03907
below –650	ENE	4.03483	–8.69230	–0.56934	–2.96	1	0.03314
	WNW	–4.87894	–10.95827	–0.33506	–3.00	1	0.04917
	NS	–7.71628	0.02693	–1.13945	–3.00	1	0.01684
	sub-H	0.80137	0.76581	–11.94870	–2.97	1	0.02480

Table A-3. Transmissivity values used for fracture domains HRD_C.

Elevation [m RHB 70]	Set	a_T (m^2/s)	b_T (–)	c_T (m^2/s)	d_T (–)
–150 to 0	ENE	$3.3653 \cdot 10^{-6}$	0.7	1	0.8
	WNW	$7.539 \cdot 10^{-6}$	0.9	1	1.2
	NS	$6.009 \cdot 10^{-7}$	0.5	1	0.8
	sub-H	$1.0096 \cdot 10^{-6}$	0.7	1	1.0
–400 to –150	ENE	$1.0096 \cdot 10^{-5}$	0.7	1	1.8
	WNW	$7.5113 \cdot 10^{-8}$	0.5	1	1.4
	NS	$1.6827 \cdot 10^{-7}$	0.7	1	0.4
	sub-H	$4.4236 \cdot 10^{-6}$	1.2	1	1.8
–650 to –400	ENE	$2.0148 \cdot 10^{-6}$	0.8	1	1.2
	WNW	$7.5555 \cdot 10^{-8}$	0.8	1	1.2
	NS	$3.0111 \cdot 10^{-8}$	0.4	1	0.8
	sub-H	$5.037 \cdot 10^{-6}$	0.8	1	1.4
below –650	ENE	$1.6827 \cdot 10^{-7}$	0.7	1	0.8
	WNW	$5.048 \cdot 10^{-6}$	0.7	1	0.8
	NS	$1.6827 \cdot 10^{-7}$	0.7	1	0.8
	sub-H	$1.6827 \cdot 10^{-6}$	0.7	1	0.8

Table A-4. Parameters values used for fracture domain HRD_W. (based on data from /Joyce et al. 2010/).

Elevation [m RHB 70]	Fracture set name	Orientation set pole: (trend, plunge), conc. κ [°,°, –]	Size model, power-law (k_r , r_0) [– , m]	Intensity, ($P_{32,open}$), valid size interval: (r_0, 564 m) [m^2/m^3]	Semi-correlated transmissivity model $log(T) = log(a\ r^b)+\sigma_{log(T)}\ N(0,1)$)
–150 to 0	ENE	(340.3,1.2), 15	(2.59, 0.038)	0.44	SC: (2.1 10^{-8}, 0.7, 0.6)
	WNW	(208.9,2.2), 10.9	(2.54, 0.038)	0.61	SC: (7 10^{-8}, 0.8, 1.0)
	N-S	(272.8,12), 11.5	(2.52, 0.038)	0.54	SC: (4 10^{-8}, 0.7, 0.8)
	Sub-H	(277.1,84.3), 11.1	(2.50, 0.038)	1.03	SC: (8 10^{-8}, 0.7, 0.7)
–400 to –150	ENE	(340.3,1.2), 15	(2.54, 0.038)	0.28	SC: (2.2 10^{-9}, 0.5, 0.4)
	WNW	(208.9,2.2), 10.9	(2.65, 0.038)	0.38	SC: (1.5 10^{-8}, 0.5, 1.2)
	N-S	(272.8,12), 11.5	(3.00, 0.038)	0.40	SC: (5 10^{-9}, 0.4, 0.3)
	Sub-H	(277.1,84.3), 11.1	(2.72, 0.038)	0.50	SC: (1.2 10^{-7}, 0.7, 1.2)
–650 to –400	ENE	(340.3,1.2), 15	(3.00, 0.038)	0.17	SC: (3 10^{-9}, 0.6, 0.4)
	WNW	(208.9,2.2), 10.9	(2.61, 0.038)	0.33	SC: (1.5 10^{-8}, 0.5, 0.3)
	N-S	(272.8,12), 11.5	(2.53, 0.038)	0.30	SC: (5 10^{-8}, 0.2, 0.2)
	Sub-H	(277.1,84.3), 11.1	(2.72, 0.038)	0.38	SC: (2 10^{-7}, 0.8, 0.8)
below –650	ENE	(155.1,3.4), 9.6	(3.00, 0.038)	0.12	SC: (1 10^{-8}, 0.7, 0.4)
	WNW	(208.9,2.2), 10.9	(3.00, 0.038)	0.09	SC: (3 10^{-8}, 0.7, 0.4)
	N-S	(272.8,12), 11.5	(2.53, 0.038)	0.14	SC: (1 10^{-8}, 0.7, 0.4)
	Sub-H	(277.1,84.3), 11.1	(3.00, 0.038)	0.65	SC: (3 10^{-8}, 0.7, 0.4)

Table A-5. DFN parameter values used in the present report for fracture domain HRD_W.

Elevation [m RHB 70]	Set	λ_1 (–)	λ_2 (–)	λ_3 (–)	D (–)	l_{ref} (m)	l (m^{-3})
–150 to 0	ENE	–5.05532	14.11896	–0.31414	–2.59	1	0.05303
	WNW	–5.26390	–9.53553	–0.41843	–2.54	1	0.07717
	NS	–11.23527	0.54950	–2.39098	–2.52	1	0.06952
	sub-H	–1.09400	0.13626	–11.04512	–2.50	1	0.13476
–400 to –150	ENE	–5.05532	14.11896	–0.31414	–2.54	1	0.03542
	WNW	–5.26390	–9.53553	–0.41843	–2.65	1	0.04285
	NS	–11.23527	0.54950	–2.39098	–3.00	1	0.02694
	sub-H	–1.09400	0.13626	–11.04512	–2.72	1	0.05166
–650 to –400	ENE	–5.05532	14.11896	–0.31414	–3.00	1	0.01145
	WNW	–5.26390	–9.53553	–0.41843	–2.61	1	0.03894
	NS	–11.23527	0.54950	–2.39098	–2.53	1	0.03829
	sub-H	–1.09400	0.13626	–11.04512	–2.72	1	0.03926
below –650	ENE	–5.05532	14.11896	–0.31414	–3.00	1	0.00808
	WNW	–5.26390	–9.53553	–0.41843	–3.00	1	0.00606
	NS	–11.23527	0.54950	–2.39098	–2.53	1	0.01787
	sub-H	–1.09400	0.13626	–11.04512	–3.00	1	0.04378

Table A-6. Transmissivity values used for fracture domain HRD_W.

Elevation [m RHB 70]	Set	a_T (m^2/s)	b_T (–)	c_T (m^2/s)	d_T (–)
–150 to 0	ENE	$3.5336 \cdot 10^{-7}$	0.7	1	1.2
	WNW	$1.7629 \cdot 10^{-6}$	0.8	1	2.0
	NS	$6.7307 \cdot 10^{-7}$	0.7	1	1.6
	sub-H	$1.3461 \cdot 10^{-6}$	0.7	1	1.4
–400 to –150	ENE	$1.6525 \cdot 10^{-8}$	0.5	1	0.8
	WNW	$1.1267 \cdot 10^{-7}$	0.5	1	2.4
	NS	$2.5092 \cdot 10^{-8}$	0.4	1	0.6
	sub-H	$2.0192 \cdot 10^{-6}$	0.7	1	2.4
–650 to –400	ENE	$3.3727 \cdot 10^{-8}$	0.6	1	0.8
	WNW	$1.1267 \cdot 10^{-7}$	0.5	1	0.6
	NS	$1.1201 \cdot 10^{-7}$	0.2	1	0.4
	sub-H	$5.037 \cdot 10^{-6}$	0.8	1	1.6
below –650	ENE	$1.6827 \cdot 10^{-7}$	0.7	1	0.8
	WNW	$5.048 \cdot 10^{-7}$	0.7	1	0.8
	NS	$1.6827 \cdot 10^{-7}$	0.7	1	0.8
	sub-H	$5.048 \cdot 10^{-7}$	0.7	1	0.8

Table A-7. Parameters values used for fracture domain HRD_N. (Modified after Table 10-18 in /Rhén et al. 2009/.)

Elevation [m RHB 70]	Fracture set name	Orientation set pole: (trend, plunge), conc. κ [°,°, –]	Size model, power-law (k_r , r_0) [– , m]	Intensity, ($P_{32,open}$), valid size interval: (r_0, 564 m) [m^2/m^3]	Semi-correlated transmissivity model $log(T) = log(a\ r^b) + \sigma_{log(T)}\ N(0,1)$)
–150 to 0	ENE	(342.2,0.2), 15.8	(2.5, 0.038)	0.41	SC: ($1 \cdot 10^{-7}$, 0.6, 0.6)
	WNW	(209.8,1.6), 14.6	(2.3, 0.038)	0.92	SC: ($2 \cdot 10^{-7}$, 0.7, 0.8)
	N-S	(271.3,3.8), 10.3	(2.5, 0.038)	0.46	SC: ($1 \cdot 10^{-7}$, 0.7, 1.0)
	Sub-H	(238.9,81.5), 12.7	(2.7, 0.038)	1.35	SC: ($2 \cdot 10^{-7}$, 0.7, 1.0)
–400 to –150	ENE	(342.2,0.2), 15.8	(2.8, 0.038)	0.41	SC: ($1 \cdot 10^{-7}$, 0.6, 0.8)
	WNW	(209.8,1.6), 14.6	(2.4, 0.038)	0.54	SC: ($2 \cdot 10^{-7}$, 0.6, 0.6)
	N-S	(271.3,3.8), 10.3	(2.8, 0.038)	0.39	SC: ($1 \cdot 10^{-7}$, 0.4, 0.4)
	Sub-H	(238.9,81.5), 12.7	(2.75, 0.038)	1.28	SC: ($3 \cdot 10^{-7}$, 0.6, 0.6)
–650 to –400	ENE	(342.2,0.2), 15.8	(2.6, 0.038)	0.26	SC: ($1 \cdot 10^{-7}$, 0.5, 0.7)
	WNW	(209.8,1.6), 14.6	(2.4, 0.038)	0.36	SC: ($1 \cdot 10^{-7}$, 0.5, 0.5)
	N-S	(271.3,3.8), 10.3	(2.6, 0.038)	0.25	SC: ($5 \cdot 10^{-8}$, 0.3, 0.3)
	Sub-H	(238.9,81.5), 12.7	(2.7, 0.038)	0.41	SC: ($5 \cdot 10^{-8}$, 0.4, 0.4)
below –650	ENE	(342.2,0.2), 15.8	(2.9, 0.038)	0.35	SC: ($5 \cdot 10^{-9}$, 0.6, 0.4)
	WNW	(209.8,1.6), 14.6	(2.8, 0.038)	0.45	SC: ($5 \cdot 10^{-8}$, 0.6, 0.4)
	N-S	(271.3,3.8), 10.3	(2.95, 0.038)	0.08	SC: ($5 \cdot 10^{-9}$, 0.6, 0.4)
	Sub-H	(238.9,81.5), 12.7	(2.95, 0.038)	0.07	SC: ($1 \cdot 10^{-7}$, 0.6, 0.4)

Table A-8. DFN parameter values used in the present report for fracture domain HRD_N.

Elevation [m RHB 70]	Set	λ_1 (–)	λ_2 (–)	λ_3 (–)	D (–)	l_{ref} (m)	I (m^{-3})
–150 to 0	ENE	–4.82996	15.04355	–0.05515	–2.50	1	0.05364
	WNW	–7.25299	–12.66444	–0.40766	–2.30	1	0.13016
	NS	–10.27471	0.23317	–0.68262	–2.50	1	0.06018
	sub-H	–1.60737	–0.96963	–12.56050	–2.70	1	0.14315
–400 to –150	ENE	–4.82996	15.04355	–0.05515	–2.80	1	0.03791
	WNW	–7.25299	–12.66444	–0.40766	–2.40	1	0.07503
	NS	–10.27471	0.23317	–0.68262	–2.80	1	0.03606
	sub-H	–1.60737	–0.96963	–12.56050	–2.75	1	0.12702
–650 to –400	ENE	–4.82996	15.04355	–0.05515	–2.60	1	0.03101
	WNW	–7.25299	–12.66444	–0.40766	–2.40	1	0.05002
	NS	–10.27471	0.23317	–0.68262	–2.60	1	0.02982
	sub-H	–1.60737	–0.96963	–12.56050	–2.70	1	0.04348
below –650	ENE	–4.82996	15.04355	–0.05515	–2.90	1	0.02779
	WNW	–7.25299	–12.66444	–0.40766	–2.80	1	0.04161
	NS	–10.27471	0.23317	–0.68262	–2.95	1	0.00586
	sub-H	–1.60737	–0.96963	–12.56050	–2.95	1	0.00513

Table A-9. Transmissivity values used for fracture domain HRD_N.

Elevation [m RHB 70]	Set	a_T (m^2/s)	b_T (–)	c_T (m^2/s)	d_T (–)
–150 to 0	ENE	$1.1242 \cdot 10^{-06}$	0.6	1	1.2
	WNW	$3.3653 \cdot 10^{-06}$	0.7	1	1.6
	NS	$1.6827 \cdot 10^{-06}$	0.7	1	2.0
	sub-H	$3.3653 \cdot 10^{-06}$	0.7	1	2.0
–400 to –150	ENE	$1.1242 \cdot 10^{-06}$	0.6	1	1.6
	WNW	$2.2485 \cdot 10^{-06}$	0.6	1	1.2
	NS	$5.0185 \cdot 10^{-07}$	0.4	1	0.8
	sub-H	$3.3727 \cdot 10^{-06}$	0.6	1	1.2
–650 to –400	ENE	$7.5113 \cdot 10^{-07}$	0.5	1	1.4
	WNW	$7.5113 \cdot 10^{-07}$	0.5	1	1.0
	NS	$1.6765 \cdot 10^{-07}$	0.3	1	0.6
	sub-H	$2.5092 \cdot 10^{-07}$	0.4	1	0.8
below –650	ENE	$5.6211 \cdot 10^{-08}$	0.6	1	0.8
	WNW	$5.6211 \cdot 10^{-07}$	0.6	1	0.8
	NS	$5.6211 \cdot 10^{-08}$	0.6	1	0.8
	sub-H	$1.1242 \cdot 10^{-06}$	0.6	1	0.8

Table A-10. Parameters values for fracture domain HRD_EW007. (based on data from /Joyce et al. 2010/).

Elevation [m RHB 70]	Fracture set name	Orientation set pole: (trend, plunge), conc. κ [°,°, –]	Size model, power-law (k_r , r_0) [– , m]	Intensity, ($P_{32,open}$), valid size interval: (r_0, 564 m) [m²/m³]	Semi-correlated transmissivity model $log(T) = log(a\ r^b)+\sigma_{log(T)}\ N(0,1)$)
–150 to 0	ENE	(162.8,1.4), 10.7	(2.77, 0.038)	0.55	SC: (3 10^{-8}, 0.6, 0.4)
	WNW	(25.3,0.2), 16.4	(2.30, 0.050)	1.01	SC: (3 10^{-8}, 0.6, 0.3)
	N-S	(88.9,3.9), 8.8	(2.53, 0.038)	0.33	SC: (1 10^{-7}, 0.8, 0.3)
	Sub-H	(138.7,81.3), 9.7	(2.76, 0.038)	1.72	SC: (2.3 10^{-7},0.8,0.5)
–400 to –150	ENE	(162.8,1.4), 10.7	(2.83, 0.038)	0.60	SC: (2 10^{-7}, 0.6, 0.6)
	WNW	(25.3,0.2), 16.4	(2.41, 0.038)	1.15	SC: (3 10^{-8}, 0.6, 0.4)
	N-S	(88.9,3.9), 8.8	(2.60, 0.038)	0.54	SC: (3 10^{-7},0.8, 0.4)
	Sub-H	(138.7,81.3), 9.7	(2.84, 0.038)	0.82	SC: (5 10^{-8}, 0.8, 0.4)
–650 to –400	ENE	(162.8,1.4), 10.7	(2.93, 0.038)	0.69	SC: (1 10^{-8}, 0.5, 0.2)
	WNW	(25.3,0.2), 16.4	(2.62, 0.038)	1.43	SC: (1.2 10^{-7}, 0.3, 0.2)
	N-S	(88.9,3.9), 8.8	(3.00, 0.038)	0.64	SC: (8 10^{-8}, 0.4, 0.2)
	Sub-H	(138.7,81.3), 9.7	(2.99, 0.038)	0.92	SC: (1.5 10^{-7}, 0.7, 0.3)
below –650	ENE	(162.8,1.4), 10.7	(2.96, 0.038)	0.33	SC: (1 10^{-8}, 0.7, 0.4)
	WNW	(25.3,0.2), 16.4	(3.00, 0.038)	0.89	SC: (3 10^{-7}, 0.7, 0.4)
	N-S	(88.9,3.9), 8.8	(3.00, 0.038)	0.21	SC: (1 10^{-8}, 0.7, 0.4)
	Sub-H	(138.7,81.3), 9.7	(2.97, 0.038)	0.80	SC: (1 10^{-7}, 0.7, 0.4)

Table A-11. DFN parameter values used in the present report for fracture domain HRD_EW007.

Elevation [m RHB 70]	Set	λ_1 (–)	λ_2 (–)	λ_3 (–)	D (–)	l_{ref} (m)	l (m^{-3})
–150 to 0	ENE	3.16313	–10.21843	–0.26142	–2.77	1	0.05308
	WNW	7.00863	14.82686	–0.05725	–2.30	1	0.15595
	NS	8.77800	0.16855	–0.59853	–2.53	1	0.04212
	sub-H	0.96837	–1.10228	–9.58839	–2.76	1	0.16834
–400 to –150	ENE	3.16313	–10.21843	–0.26142	–2.83	1	0.05308
	WNW	7.00863	14.82686	–0.05725	–2.41	1	0.15909
	NS	8.77800	0.16855	–0.59853	–2.60	1	0.06441
	sub-H	0.96837	–1.10228	–9.58839	–2.84	1	0.07146
–650 to –400	ENE	3.16313	–10.21843	–0.26142	–2.93	1	0.05221
	WNW	7.00863	14.82686	–0.05725	–2.62	1	0.16689
	NS	8.77800	0.16855	–0.59853	–3.00	1	0.04311
	sub-H	0.96837	–1.10228	–9.58839	–2.99	1	0.06303
below –650	ENE	3.16313	–10.21843	–0.26142	–2.96	1	0.02377
	WNW	7.00863	14.82686	–0.05725	–3.00	1	0.05995
	NS	8.77800	0.16855	–0.59853	–3.00	1	0.01415
	sub-H	0.96837	–1.10228	–9.58839	–2.97	1	0.05668

Table A-12. Transmissivity values used for fracture domain HRD_EW007.

Elevation [m RHB 70]	Set	a_T (m^2/s)	b_T (–)	c_T (m^2/s)	d_T (–)
–150 to 0	ENE	$3.3727 \cdot 10^{-7}$	0.6	1	0.8
	WNW	$3.3727 \cdot 10^{-7}$	0.6	1	0.6
	NS	$2.5185 \cdot 10^{-6}$	0.8	1	0.6
	sub-H	$5.7925 \cdot 10^{-6}$	0.8	1	1.0
–400 to –150	ENE	$2.2485 \cdot 10^{-6}$	0.6	1	1.2
	WNW	$3.3727 \cdot 10^{-7}$	0.6	1	0.8
	NS	$7.5555 \cdot 10^{-6}$	0.8	1	0.8
	sub-H	$1.2592 \cdot 10^{-6}$	0.8	1	0.8
–650 to –400	ENE	$7.5113 \cdot 10^{-8}$	0.5	1	0.4
	WNW	$4.0235 \cdot 10^{-7}$	0.3	1	0.4
	NS	$4.0148 \cdot 10^{-7}$	0.4	1	0.4
	sub-H	$2.524 \cdot 10^{-6}$	0.7	1	0.6
below –650	ENE	$1.6827 \cdot 10^{-7}$	0.7	1	0.8
	WNW	$5.048 \cdot 10^{-6}$	0.7	1	0.8
	NS	$1.6827 \cdot 10^{-7}$	0.7	1	0.8
	sub-H	$1.6827 \cdot 10^{-6}$	0.7	1	0.8

For all regions of the domain assessed, approximate homogeneous CPM properties of the flow-wetted fracture surface area per unit volume of rock mass (a_r) are based on the data provided by /Joyce et al. 2010/, see Table A-13 and Table A-14.

Table A-13. Specific flow-wetted fracture surface area per unit volume of rock applied for the fracture domains inside the focused area/volume.

Elevation [m RHB 70]	HRD_C a_r [m^2/m^3]	HRD_W a_r [m^2/m^3]	HRD_N a_r [m^2/m^3]	HRD_EW007 a_r [m^2/m^3]
> –150	1.00	1.00	1.50	1.50
–150 – –400	0.40	0.40	0.67	1.00
–400 – –650	0.22	0.12	0.33	0.40
<–650	0.02	0.02	0.16	0.04

For the region outside the detailed described HRDs i.e. on a regional scale, the ECPM settings of hydraulic conductivity and kinematic porosity of the SDM-Site regional flow domain are established from a deterministic fracture set containing fracture geometry and fracture transmissivity.

For the region outside the SDM-Site regional flow domain homogeneous CPM properties are assigned. These properties are based on the calculated median of the overall deterministic fracture set regardless of underlying fracture domains.

Table A-14. Homogeneous continuous porous media (CPM) properties applied in hydraulic rock domains outside the SDM-Site regional flow domain.

	CPM properties outside the SDM-Site regional flow domain		
Elevation [m RHB 70]	***K*** **[m/s]**	ϕ **[–]**	***ar*** **[m²/m³]**
> –150	$2.9 \cdot 10^{-6}$	$2.1 \cdot 10^{-5}$	1.50
–150 – –400	$5.4 \cdot 10^{-7}$	$1.3 \cdot 10^{-5}$	0.67
–400 – –650	$6.0 \cdot 10^{-8}$	$1.0 \cdot 10^{-5}$	0.33
<–650	$4.6 \cdot 10^{-9}$	$1.0 \cdot 10^{-5}$	0.16

The general approach in DarcyTools is to specify the fracture thickness b_f [L] and the fracture kinematic porosity ϕ_f [–] of the stochastically generated fractures by fracture set and by fracture size interval. Hence, in DarcyTools there is no direct relationship between transmissivity and transport aperture but the fracture transport aperture is obtained from the thickness-porosity product, i.e.

$$e_f = b_f \phi_f \tag{A-9}$$

In the work reported here all stochastically generated fractures have the same values of the fracture thickness and the fracture kinematic porosity. The values used are presented in Table A-15 together with some other fracture specifications.

Table A-15. Additional specifications used in DarcyTools.

Specification	Value	Minimum value
Generated fracture size interval	15–1,000 [m][1]	
Fracture thickness	0.1 [m]	
Fracture kinematic porosity	$1 \cdot 10^{-3}$ [–]	
Diffusion coefficient in free water	$1 \cdot 10^{-10}$ [m²/s]	
Minimum grid cell hydraulic conductivity[2]		$3 \cdot 10^{-11}$ [m/s] (~ $4 \cdot 10^{-18}$ [m²])
Minimum grid cell kinematic porosity[2]		$1 \cdot 10^{-5}$ [–]

[1] This data range refers to square-shaped fractures. The interval for disc-shaped fractures is 8.5–564 m.

[2] Used for cells without fractures.